Lancaster University

Characterisation and simulation of InAs/InAsSb structures for mid – infrared LEDs

James Alexander Keen

MPhys MRes

Supervisor: Prof. A. Krier

Thesis presented for the degree of

Doctor of Philosophy (PhD)

in Physics

September 2018

Declaration

I declare that the contents of this thesis, titled '*Characterisation and simulation of InAs/InAsSb structures for mid – infrared LEDs*', are the result of my own independent work. Where I have consulted the published work of others this is acknowledged by explicit references. I confirm that this work has not been submitted in whole or in any part for any other degree or qualification at this university or at any other academic institution.

James Keen

September 2018

Characterisation and simulation of

InAs/InAsSb structures for mid – infrared LEDs

James Alexander Keen

September 2018

Abstract

This work reports research on InAs/InAsSb structures focusing on their photoluminescence and electroluminescence spectra over the 4 – 300 K temperature range. The purpose was to gain an insight into developing mid – infrared light – emitting diodes (LEDs) operating with sufficiently high power and efficiency for room temperature gas sensing applications.

InAs/InAsSb strained – layer superlattice (SLS) and multiple quantum well (MQW) structures of low antimony content (Sb = 3.7 – 13.5 %) grown by MBE on InAs substrates were compared. These structures were characterised by XRD and TEM imaging. Band structure simulations highlighted the effects of changing QW antimony content and layer thicknesses on the emission properties.

Mid – infrared 4 – 300 K photoluminescence showed peak shifting to longer wavelengths and intensity reduction for structures with increased QW antimony

content. Excitonic emission identified in the photoluminescence spectra under low excitation power was investigated. Temperature quenching was attributed to competing radiative and non – radiative free carrier recombination processes. At higher temperatures, MQW photoluminescence was dominated by emission from electron – hole recombination in the InAs barrier layers. This was not observed for the SLS, with holes strongly confined in the QWs up to room temperature. The dominant Auger process was identified to differ between the MQW and SLS structures, with larger experimental values for these processes compared to theory indicating some degree of suppression due to the type II band alignment of the structures. All these findings highlighted the superiority of the SLS and its attractiveness for use in the active region of MIR LEDs.

Two prototype SLS LEDs were fabricated. Mid – infrared 7 – 300 K electroluminescence was obtained, with the 4.2 μm CO_2 absorption fingerprint identifiable. The electroluminescence spectra displayed similar behaviour to the PL spectra. Microwatt output powers were produced by the devices at room temperature. Approaches to improve device performance are considered, as it is of interest to further develop SLS LEDs for mid – infrared applications.

Acknowledgements

My thanks go to those whom without their support in a variety of ways I would not have been able to progress through to successfully complete the long, challenging and ultimately rewarding experience of the PhD. I wish to firstly thank my supervisor Professor Anthony Krier for his continued support and guidance throughout, and for the opportunity four years ago to return to Lancaster University to undertake the PhD having enjoyed the time here previously whilst completing an undergraduate physics degree. I would like to thank my colleagues Dr Andy Marshall, Dr Manoj Kesaria, Dr Qi Lu, Dr Jonathan Hayton and Dr Peter Carrington who all when approached kindly offered their expertise to help progress my work though tricky patches. Thanks also go to those within the physics department who have provided technical assistance whenever needed – Alan Stokes for the provision of liquid helium and nitrogen necessary for operating the laboratory equipment to obtain measurements, Steve Holt and those in the teams of the electronics and mechanical workshops for keeping the laboratory equipment operational, Rob Lewsey for I.T. support, and Shonah Ion for working tirelessly to oversee everything and keep the whole department running smoothly. My appreciation also goes to the fellow PhD students I have shared offices, laboratories and lunchtimes with who have become good friends – particularly Denise Montesdeoca Cardenes and Eva Repiso, Veronica Letka and Ofogh Tizno, Simon Malzard and Marjan Famili, James Edholm, Laura Hanks and Jonathan Hayton, just to name a few. I have valued your friendship, good humour and encouragement and hope I was equally as engaging. Finally, a special thanks to my family – particularly my parents, sister and uncle – for their unlimited support and encouragement throughout all my academic studies.

Journal Publications

1. *Electroluminescence and photoluminescence of type-II InAs/InAsSb strained-layer superlattices in the mid-infrared*, **J.A. Keen**, E. Repiso, Q. Lu, M. Kesaria, A.R.J. Marshall, A. Krier, Infrared Physics & Technology, 93, p. 375-380, (2018)

2. *InAs / InAsSb type II strained-layer superlattices for mid-infrared LEDs*, **J.A. Keen**, D. Lane, M. Kesaria, A.R.J. Marshall, A. Krier, Journal of Physics D - Applied Physics, 51, 7, (2018)

3. *Modelling and measurement of bandgap behaviour in medium-wavelength IR InAs/$InAs_{0.815}Sb_{0.185}$ strained-layer superlattices.* V. Letka, **J. Keen**, A. Craig, A.R.J. Marshall. SPIE proceedings 10433; Electo-optical and infrared systems: technology and applications XIV conference, Warsaw (2017)

Conference Presentations

1. *Characterisation of InAs/InAsSb type II MQW & SLS structures for MIR LEDs*. **J. Keen**, E. Repiso, Q. Lu, D. Lane, J. Morgan, M. Kesaria, A.R.J. Marshall, A. Krier. PROMIS conference, 18th July 2018, Windermere, UK. Talk.

2. *Strained type II InAs / InAsSb superlattice structures on InAs for use in mid-infrared LEDs,* **J. Keen**, D. Lane, M. Kesaria, A. Marshall, A. Krier, UK Semiconductors (UKSC) Conference 2017, 13th July 2017, Sheffield, UK. Talk.

3. *Design of InAs / InAsSb superlattice structures for mid-infrared LEDs for gas detection,* **J. Keen**, Postgraduate Research Conference (PGRC) 2017, 6th May 2017, Lancaster University, Lancaster, UK. Talk.

4. *Design of InAs / InAsSb superlattice structures for mid-infrared LEDs on InAs,* **J. Keen**, A. Krier, Semiconductor and Integrated OptoElectronics (SIOE) Conference 2017, 19th April 2017, Cardiff, UK. Talk.

5. *Designing high performance InAs / InAsSb superlattice light emitting diodes,* **J. Keen**, Faculty of Science & Technology (FST) Christmas Conference 2016, 20th December 2016, Lancaster University, Lancaster UK. Poster presentation. *Winner of 1st prize for best poster.

Contents

Index of Figures & Tables

Chapter 1

Introduction

The 3 – 5 µm mid – infrared (MIR) region of the electromagnetic spectrum continues to attract significant interest due to its importance for a variety of technological applications, including but not limited to the detection and monitoring of environmentally harmful gases [5, 6, 7], medical diagnostics and treatments [8, 9], military security and defence [10, 11, 7] and space technology [12]. This MIR region is particularly suited for gas sensing as it features the unique absorption signatures of environmentally harmful gases (Figure 1.1) such as methane (3.3 µm), carbon dioxide (4.2 µm), carbon monoxide (4.6µm) and nitrous oxide (5.2 µm). Detecting and monitoring the presence of these gases is desirable in a range of different situations, such as checking emissions from vehicle exhausts and power stations as well as identifying biohazards.

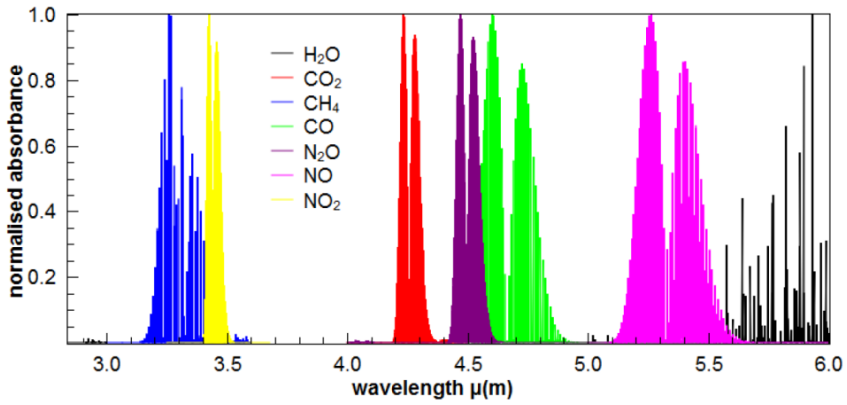

Figure 1.1 – Absorption signatures of gases in the mid-infrared (MIR) spectral region [1], including methane (CH_4) at 3.3 µm, carbon dioxide (CO_2) at 4.2 µm and carbon monoxide (CO) at 4.6 µm.

Although semiconductor lasers have been developed for most of these applications, leading to the realisation of commercially available devices, LEDs are a promising

alternative due to favourable operating properties including lower complexity and simpler implementation, temperature stability, lower power and lower cost [13]. Despite these advantages there has been much less development of mid – infrared LEDs, presenting an opportunity for their further study.

LEDs are a particularly attractive method for gas sensing as the LED emission spectra can be tuned to coincide with the absorption of the gas to be detected, creating a gas specific detector [14]. Additionally, they are advantageous over electrochemical detection methods due to a significantly lower chance of cross – response and the ability of the measurements to take place in situ and in real time rather than requiring a sample to be removed and analysed elsewhere [1]. LEDs exhibiting broad emission spectra would suffice for gas identification under controlled conditions where a high concentration of the target gas can be provided. However, for real world applicability the emission spectra should be tuned to centre precisely on the wavelength of the gas absorption line to provide maximum sensitivity such that the devices operate with sufficiently high efficiency to detect the low concentrations of these gases naturally present in the environment. The atmospheric concentration of CO_2 is now above 400 ppm (parts per million) whereas the concentrations of CO and CH_4 are only ≈ 0.2 ppm and ≈ 1800 ppb respectively [15], highlighting the variation in the necessary sensitivity of a gas sensing device depending on the gas. To meet the low detection threshold and achieve a high signal – to – noise ratio during measurements the output power of the LED should be as high as possible, with an output of > 1 mW commonly agreed as the requirement for a device to be practical in real world applications [14, 1]. Furthermore, the absorption band of a gas has a

typical bandwidth of 2 % around the central wavelength [1] necessitating the need for narrow emission spectra to maximise the strength of the detection and to minimise the risk of cross – contamination with other gases. It is notable that GSS Ltd has now established commercially available devices for the monitoring of CO_2 incorporated within heating, ventilation and air conditioning systems [16, 1]. These sensors require 3.3 µW operating power, producing an optical power of ~ 8 mW / cm^2 at 25 °C with a detection accuracy of ± 50 ppm of the gas concentration [1].

Unfortunately, mid – infrared LED efficiency at room temperature is still significantly lower than devices operating at visible and near – infrared wavelengths, because of the significant temperature dependence [17] due to the reduced energy of the photons as well as high rates of detrimental non – radiative Auger recombination processes which increase significantly as the injected carrier concentration increases and the emission wavelength is extended [18]. Improving the room temperature output power of LEDs requires overcoming these challenges of reducing thermal escape of carriers from the QWs to maintain a high rate of radiative recombination as well as suppressing the rates of temperature – dependent non – radiative recombination processes. Additionally, the optical extraction efficiency of InAs based mid – infrared LEDs is limited to ≈ 1.4 % based on the refractive index of the material [7] which adds a further constraint on device performance.

Straightforward comparison of the performance of infrared LEDs is tricky as there are not commonly agreed parameters for benchmarking. Usually a specific parameter relevant to the intended application is the subject of improvement, possibly at the

cost of other parameters. This selectivity of parameters such as output power, injection current, duty cycle, emitting area and temperature can skew the perceived overall performance of the device. An attempt to provide an insight into the infrared LEDs reported in academic literature and available commercially is presented in Figure 1.2. The output powers are the reported values for operation in either pulsed mode or quasi – CW mode. Note that scaling to normalise the values has not been applied due to the absence of key information regarding device properties such as emitting area, so values are taken as is but still act to give a good impression of the current state of the field.

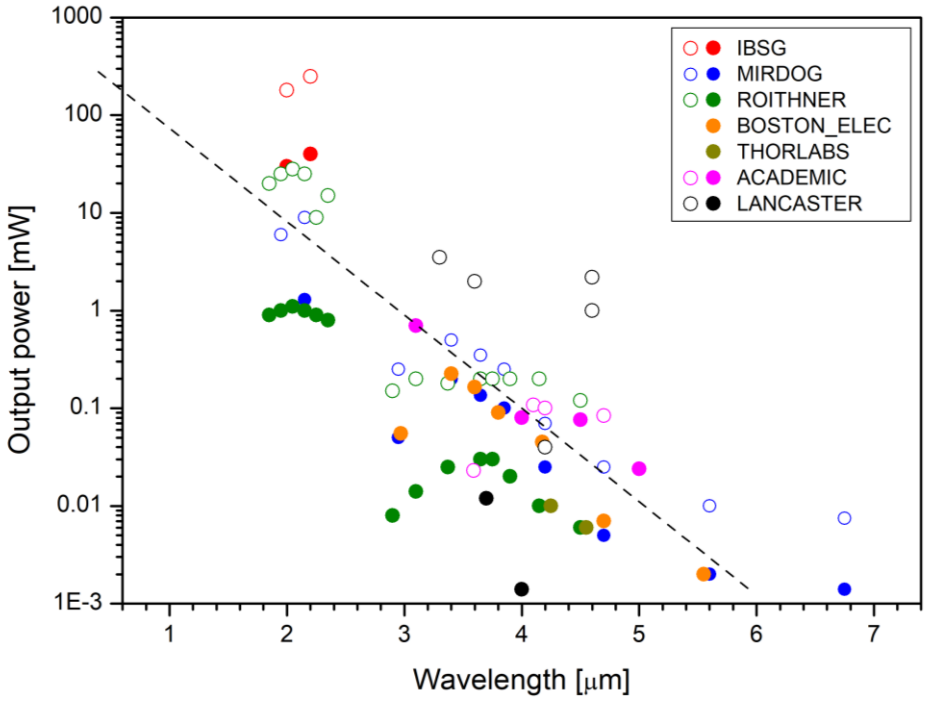

Figure 1.2 – Comparison of reported LED output power versus emission wavelength. Note this only a general picture as the emissions are obtained from device operation under different drive conditions (qCW – solid circles, pulsed – open circles) and the results have not been adjusted to account for structural differences such as emitting area. The dashed line is included to act as a guide to the eye, showing the overall trend of a decrease of output power with increase of emitting wavelength.

The key observation is the clear downwards trend of output power from the LEDs as the emission wavelength is moved longer, primarily due to the reduced energy of the

photons. Despite the large number of reported MIR LEDs, the lack of those producing emission of > 1 mW output power at mid infrared wavelengths ($\lambda \geq 3$ μm) highlights the challenges of developing devices operating in this region suitable for gas sensing.

This thesis reports the research and development work to optimise the InAs/InAsSb type II structure for use as the active region in mid – infrared light – emitting diodes (LEDs). The InAs/InAsSb structure has been chosen due to the ability to tailor the structure (layer thicknesses and compositions) to produce emission at specific wavelengths coinciding with the MIR wavelengths at which absorption of target gases occurs; the target gases are chosen to be CO_2 and CO which exhibit strong absorptions at 4.2 μm and 4.6 μm respectively. The rates of radiative and non – radiative recombination processes and their effects on device performance are investigated, with a focus on optimising room temperature device output power at the target wavelengths. LEDs featuring the InAs/InAsSb structure as the active region are fabricated and tested to compare with the results of the standalone structures, demonstrating the realisation of working devices for CO_2 and CO gas sensing.

This chapter, *Chapter 1*, has introduced the motivation of the work and outlined the scope of this Thesis. Theoretical concepts are covered in *Chapter 2*, followed by *Chapter 3* which presents an up to date review of academic literature on InAs(Sb) – based mid – infrared LEDs, and an overview of the experimental procedures is in *Chapter 4*. The results of the work undertaken during this PhD are presented and extensively discussed in *Chapter 5,* with a summary and conclusions in *Chapter 6*.

Chapter 2

Theory & fundamental concepts

This work focuses on the study of III – V semiconductor structures, specifically the type II InAs/InAsSb structure, and their utilisation in mid – infrared light – emitting diodes (LEDs). In this chapter the theory and concepts necessary to understand to be able to undertake an informed research and development process are outlined. Firstly, the concept of a material band structure is introduced including the effects of temperature, material compositions and strain. Secondly, the radiative and non – radiative recombination processes of free carriers (electrons and holes) are outlined. Thirdly, the experimental techniques of photoluminescence and electroluminescence used to analyse samples and devices are discussed. Finally included is the concept of a light – emitting diode and the approach for characterising device performance.

2.1 Band structure of semiconductors

When atoms and molecules join to form materials their individual discrete energy levels combine to form distinct energy bands. Since all the lower energy bands are constantly filled, descriptions of material band structures usually only concern the outermost fully occupied band, called the valence band, and the next highest energy band called the conduction band into which excited electrons can move. The energy spacing between these bands, referred to as the band gap of the material, governs whether the material behaves as an insulator, semiconductor, or metal. At the temperature minimum of 0 K all electrons reside in the valence band. As temperature rises the increase of thermal energy is enough to enable electrons to

move from the valence band across the band gap into the available empty states in the higher energy conduction band and contribute to the conduction of electricity through the material. In metals the overlap of the bands easily facilitates this movement; metals are excellent electrical conductors. The wide band gap of insulators prevents the movement of electrons. Semiconductors are semi – conducting materials in which electrons can move if provided with enough energy to overcome the band gap energy of the material. A schematic of the band structures for these different types of materials is shown in Figure 2.1.

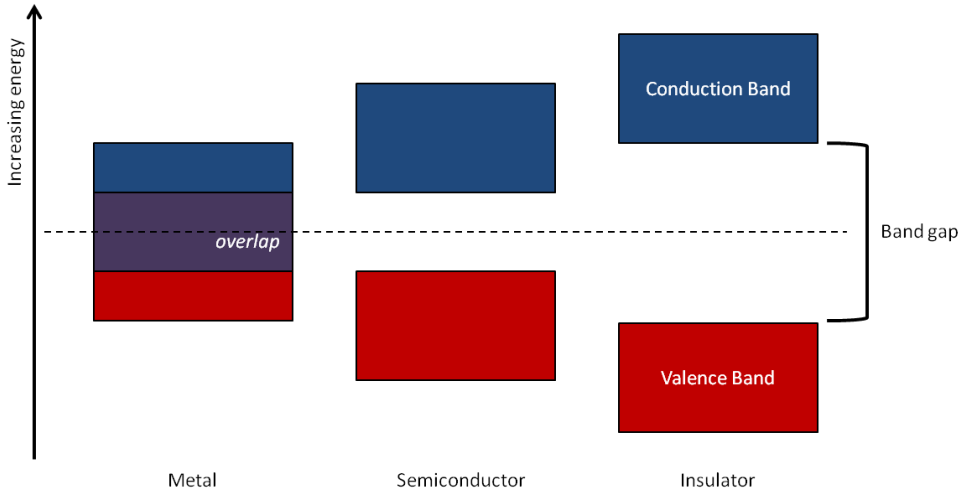

Figure 2.1 – Schematic of metal, semiconductor and insulator band structures showing the respective energy requirement to enable electron promotion out of the valance band and across the band gap into the conduction band.

2.1.1 Temperature dependence of band structure

As temperature increases the lattice of the semiconductor material expands and the electrons become less bound to the fixed ions. This means less energy is required to facilitate movement of electrons from the valence band to the conduction band, hence the band gap exhibited by the material reduces.

The change of semiconductor band gap with temperature $E_g(T)$ can be modelled using the Varshni equation [19]:

$$E_g(T) = E_g(0) - \frac{\alpha T^2}{\beta + T} \qquad (2.1)$$

where $E_g(0)$ is the band gap of the material at the minimum temperature of 0 K and the coefficients α and β are fitting parameters. The value of α is related to the thermal expansion of the lattice, and the value of β corresponds to the Debye temperature in the Debye theory.

2.1.2 Band structure alignments

A schematic energy band diagram of two different undoped semiconductor materials placed side by side is shown in Figure 2.2. Conduction band and valence band energies are represented by $E_{cb(i)}$ and $E_{vb(i)}$ respectively. The differences in the energies of the conduction and valence bands are referred to as the conduction and valence band offsets (ΔE_{cb} and ΔE_{vb}). Fermi levels are defined by $E_{f(i)}$. Electron affinity $\chi_{(i)}$ is defined as the energy required for an electron to move out of the conduction band. Each semiconductor material exhibits an individual χ value. Considering the electron affinity of the two materials determines their band alignment with respect to each other. The difference between the conduction bands is defined by the difference between the electron affinities:

$$\Delta E_{cb} = \chi_1 - \chi_2 \qquad (2.2)$$

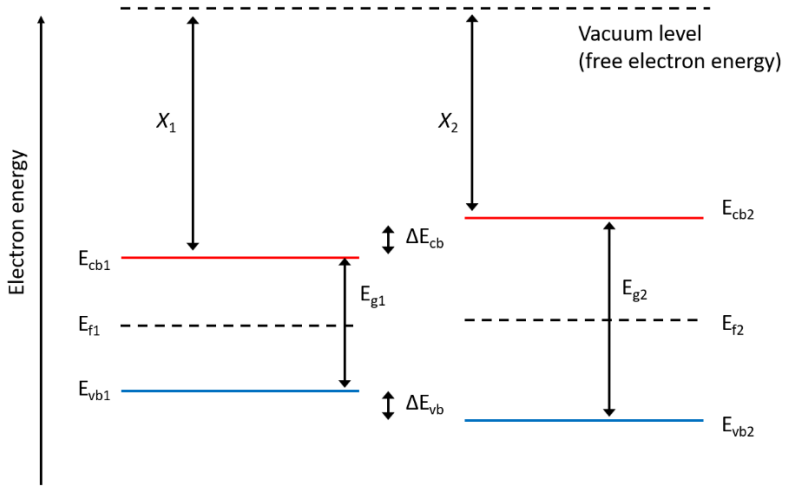

Figure 2.2 – Schematic energy band diagram showing two undoped semiconductor materials side by side. The electron affinity values ($\chi_{(n)}$) determine their band alignment with respect to each other. Conduction and valence band energies ($E_{cb(n)}$ and $E_{vb(n)}$), differences between the conduction bands and the valence bands ($\Delta E_{cb(n)}$ and $\Delta E_{vb(n)}$) as well as the band gaps ($E_{g(i)}$) and the Fermi levels ($E_{f(i)}$) are all labelled.

The joining of two different semiconductor materials creates energy discontinuities at the abrupt interface between them caused by the difference in Fermi levels and electron affinities, resulting in the formation of a heterojunction. The difference between the band gap of the two layers can be defined in terms of the differences between the energies of the conduction and valence bands:

$$E_{g(2)} - E_{g(1)} = \Delta E_C + \Delta E_V \qquad (2.3)$$

The band alignment of the two materials determines whether ΔE_C and ΔE_V values are positive or negative, and thus whether the band structure is stated to be Type I or Type II. Figure 2.3 shows schematically the different possible band structures. Type I and type II structures exhibit different carrier recombination behaviour. In the type I band alignment the value of ΔE_C is negative and ΔE_V is positive, meaning the conduction band of the smaller band gap material is of lower energy than in the larger band gap material, and conversely the valence band of the smaller band gap

material is of higher energy than in the larger band gap material. Electrons and holes are both confined in the smaller band gap material and recombine via direct transitions. An example of a structure with type I band alignment is InAs / GaAs. In the type II band alignment, the band offsets ΔE_C and ΔE_V are both negative (type IIa) or both positive (type IIb). In the type IIa structure the electrons are located within the smaller band gap material and the holes in the larger band gap material, with this opposite for the type IIb material. An example of a type IIa structure is InAs / AlSb; examples of type IIb structures are InAs / InAsSb and GaSb / GaAs. Due to the spatial separation of the carriers, the recombination occurs via spatially indirect transitions (though still direct in k – space). If the value of ΔE_V is larger than the energy band gap of one of the materials, such that the energy of the valence band of one material is higher than the energy of the conduction band in the other material, then a "broken gap" type II band structure (sometimes called type III) is formed; examples of this are InSb / InAs and InAs / GaSb.

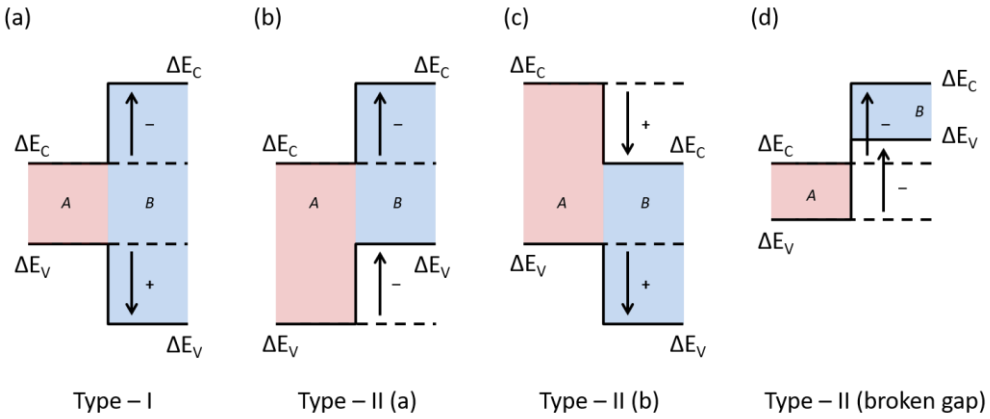

Figure 2.3 – Heterojunction band alignment possibilities showing type I and type II structures.

2.1.3 Band gap of alloy materials

The band gap of binary materials (e.g. InAs) is fixed, aside from variation due to temperature, meaning their application is somewhat limited. However, alloy materials comprised of two binary materials (e.g. InAsSb is the alloy of InAs and InSb) can have their band gap varied by changing the composition of the three elements in addition to changing the layer thicknesses. The band gap of these alloy materials can be predicted from consultation of a lattice constant versus band gap energy diagram, as shown in Figure 2.4. The dependence of composition on the band gap energy (E_g) of an alloy material follows Vegard's Law:

$$E_g(A_{1-x}B_x) = (1-x)E_g(A) + xE_g(B) - x(1-x)C \qquad (2.4)$$

where *A* is the first material (for example, InAs) and *B* is the second material (for example, InSb), x is the percentage of the third element (for example, Sb), and C is the bowing parameter which is either set to zero for linear interpolation of band gap between the two binaries or a non – zero value that adds a bowing of the band gap dependence. This expression relates to a free – standing layer of the material. It is important to note that if the material is not fully relaxed, for example if a layer of InAsSb is grown on top of a layer of InAs, then the compressive strain present will act to modify the band edges and increase the band gap, such that following this equation the band gap energy of the strained material will likely be underestimated compared to that expected for a relaxed layer of the same material [20].

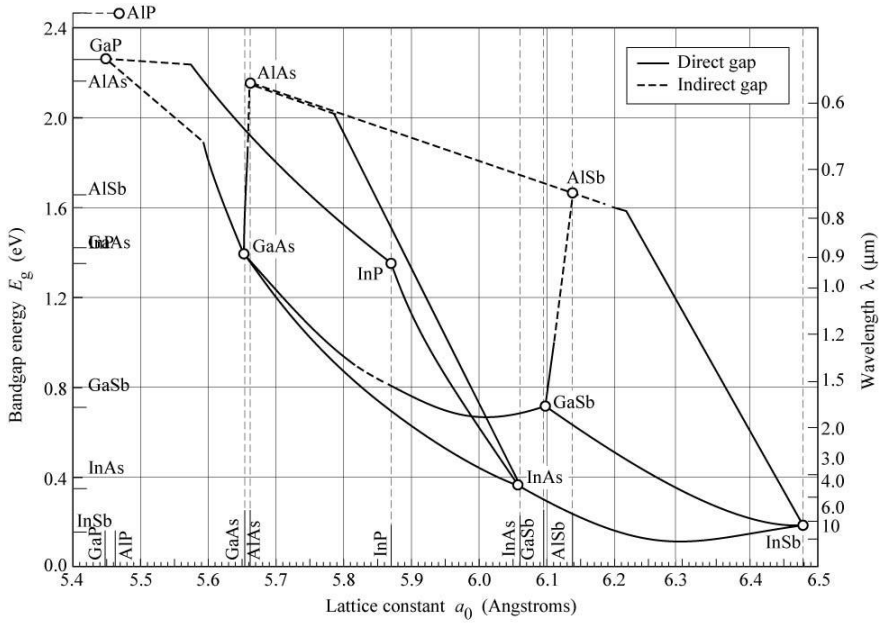

Figure 2.4 – Band gap energy versus lattice constant of III – V semiconductor materials at room temperature, indicating the possible emission wavelengths achievable from structures comprised of different compositions and combinations of these materials [21].

2.1.4 Strained layers

Deposition of a layer of semiconductor material onto another semiconductor material of different lattice constant creates strain within the structure as the top material needs to reshape to enable bonding to the bottom material. If the lattice constant of the top layer is greater ($a_2 > a_1$) then compressive strain reduces the lattice in the direction perpendicular to growth and it increases in the direction of growth (Figure 2.5). If the lattice constant of the top layer is less ($a_2 < a_1$) then tensile strain has the opposite effect of increasing its lattice in the direction perpendicular to growth and reducing it in the direction of growth (Figure 2.6).

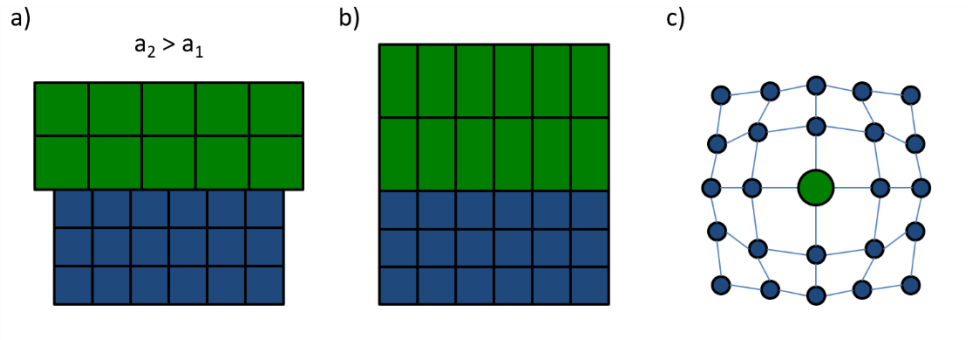

Figure 2.5 – Schematic showing a layer of semiconductor material of large lattice constant (green area) grown on top of a layer of semiconductor material of smaller lattice constant (blue area). The larger lattice of the top material is squashed perpendicular to the direction of growth and stretched in the direction of growth, generating compressive strain in the structure.

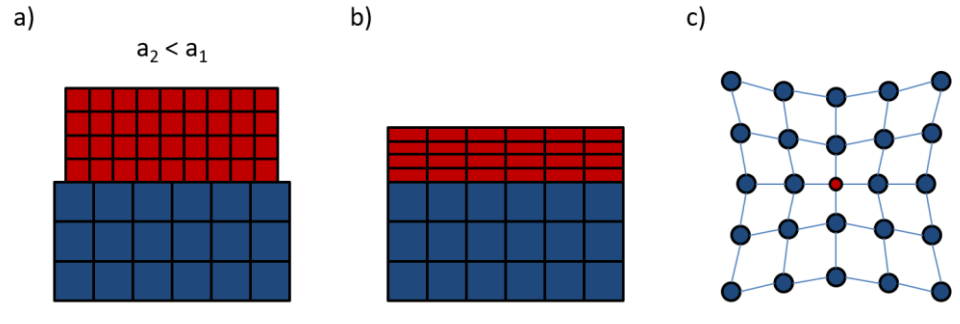

Figure 2.6 – Schematic showing a layer of semiconductor material of small lattice constant (red area) grown on top of a layer of semiconductor material of larger lattice constant (blue area). The smaller lattice of the top material is stretched perpendicular to the direction of growth and squashed in the direction of growth, which generates tensile strain in the structure.

If lattice mismatch is significant then the high deformation of the lattice structure can lead to the generation of dislocations, which are abrupt changes in the usually ordered lattice. The presence of defects in the structure, either by missing atoms or the inclusion of impurity atoms, can also cause dislocations to be generated. The two main types of dislocations are edge dislocations and screw dislocations, as pictured in Figure 2.7, with the Burgers vector indicating the magnitude and direction of the lattice shift.

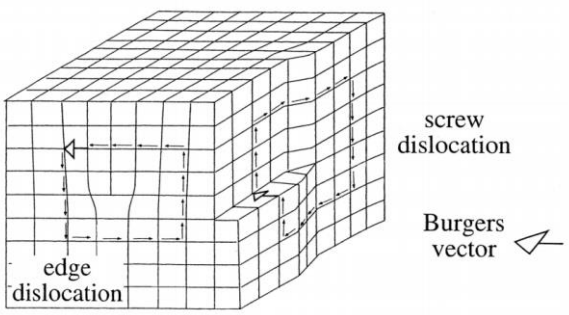

Figure 2.7 – Schematic showing edge and screw dislocations in a crystal lattice structure [22] that can be generated at the interface between two materials if there is a large lattice mismatch.

Critical Thickness is the point at which the top layer reaches a thickness such that the strain building up due to lattice mismatch generates enough energy to facilitate the formation of dislocations. An attempt at calculating this critical thickness for an edge dislocation to form at the interface between the two materials was first undertaken by Frank and van der Merwe [23] and developed by Matthews and Blakeslee [4] into the expression:

$$h_c \cong \left(\frac{b}{f}\right)\left(\frac{1}{4\pi(1+v)}\right)\left(ln\left(\frac{h_c}{b}\right)+1\right) \qquad (2.5)$$

In this expression h_c is the critical thickness, *b* is the magnitude of the Burgers vector, *f* is the lattice mismatch, and *v* is the Poisson's ratio equal to $v = C_{12}/(C_{11}+C_{12})$ where C_{11} and C_{12} are the elastic constants of the top layer.

Another approach by People and Bean [24] considered the critical thickness for the formation of dislocations within the layer (defined as screw dislocations) rather than those forming at the interface. They introduced the similar but alternative expression:

$$h_c \cong \left(\frac{1-v}{1+v}\right)\left(\frac{b^2}{16\pi\sqrt{2a(x)}f^2}\right)\left(ln\left(\frac{h_c}{b}\right)\right) \qquad (2.6)$$

In this expression the variables are the same as in the Matthews and Blakeslee model, with the addition of the *a(x)* parameter which is the lattice constant of the material of the top layer.

Furthermore, theoretical work by O'Reilly [25] and Krijn [26] presents the changes to the conduction and valence band energies resulting from strain present in the structure. In the case of a quantum well structure, the presence of compressive strain acting in the growth direction splits the heavy hole and light hole valence bands, as shown schematically in Figure 2.8 [25].

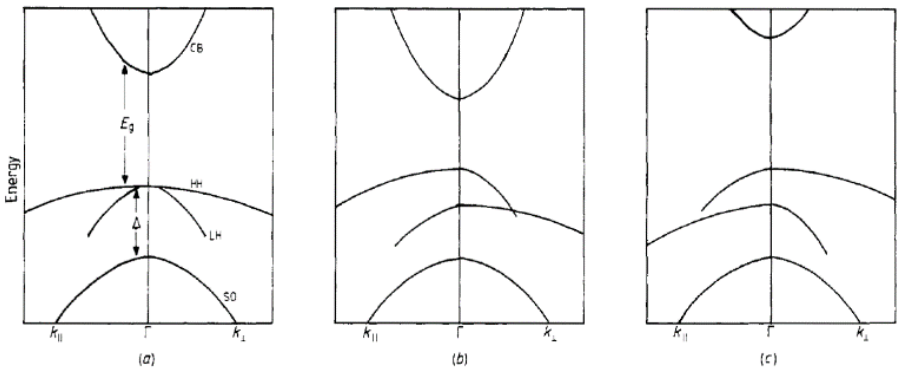

Figure 2.8 – The effect of strain on the band structure of a material [25]. (a) band structure of an unstrained direct band gap semiconductor material with heavy hole (HH) and light hole (LH) band maxima at same energy corresponding to the Brillouin zone centre and the spin – off band (SO) an energy Δ lower. (b) Biaxial tension where the hydrostatic component of strain reduces the mean band gap while the axial component splits the valence bands to create an anisotropic valence band structure. (c) Biaxial compression where the mean band gap increases, and the valence band splitting is opposite such that the highest valence band is now HH along the strain axis. Directions are defined with respect to the growth plane – k‖ represents the direction perpendicular to the growth and strain direction, with k⊥ the direction along the strain axis.

The effect of strain on the energy levels is due to two contributions – hydrostatic and shear components. The hydrostatic strain component leads to a shift of the average valence band energy:

$$E_{v,av} = \frac{(E_{HH}+E_{LH}+E_{SO})}{3} \qquad (2.7)$$

The shifts of the conduction and valence bands are expressed by Equations 2.8 & 2.9 with a_c and a_v the respective hydrostatic deformation potentials.

$$\Delta \mathrm{E}_c^{hy} = a_c(2\epsilon_{\parallel} + \epsilon_{\perp}) \tag{2.8}$$

$$\Delta \mathrm{E}_v^{hy} = a_v(2\epsilon_{\parallel} + \epsilon_{\perp}) \tag{2.9}$$

The shear component couples to the spin – orbit interaction and causes additional splitting of the valence band energies relative to $E_{v,av} = \Delta_0/3$ as:

$$\Delta \mathrm{E}_{HH}^{sh} = -\frac{1}{2}\delta E^{sh} \tag{2.10}$$

$$\Delta \mathrm{E}_{LH}^{sh} = -\frac{1}{2}\Delta_0 + \frac{1}{4}\delta E^{sh} + \frac{1}{2}\left[\Delta_0^2 + \Delta_0 \delta E^{sh} + \frac{9}{4}(\delta E^{sh})^2\right]^{1/2} \tag{2.11}$$

$$\Delta \mathrm{E}_{SO}^{sh} = -\frac{1}{2}\Delta_0 + \frac{1}{4}\delta E^{sh} - \frac{1}{2}\left[\Delta_0^2 + \Delta_0 \delta E^{sh} + \frac{9}{4}(\delta E^{sh})^2\right]^{1/2} \tag{2.12}$$

where the strain – dependent shift δE^{sh} is dependent on the interface orientation and is given by Equation 2.13 for growth on a (001) substrate, in which b is the relevant tetragonal shear deformation potential:

$$\delta E^{sh} = 2b(2\epsilon_{\parallel} + \epsilon_{\perp}) \tag{2.13}$$

Thus, the total shift of the valence band can be expressed as:

$$\Delta E_{v(HH,LH,SO)} = \Delta \mathrm{E}_v^{hy} + \Delta E_{HH,LH,SO}^{sh} \tag{2.14}$$

The shift of the SO band energy induced by the strain can be employed to suppress the CHSH Auger process by increasing the activation energy and thus reducing the rate of this process as well as reducing inter – valence band absorption [27, 26].

The need to grow structures with a high degree of lattice mismatch between the layers can be met by modifying the growth techniques to manage the high probability of undesirable defects and dislocations occurring. An approach is the Interfacial Misfit (IMF) which involves forming an abrupt interface between the

substrate and the compressively strained layer [28]. For the growth of a GaSb layer onto a GaAs substrate this technique has been shown to significantly relieve strain at the interface such that the GaSb layer is almost entirely relaxed (98.5 %) with a very low density of dislocations of 10^5 cm^{-2} compared to 10^9 cm^{-2} without the IMF layer [29, 30]. This allows the fabrication of high quality GaSb based devices on GaAs substrates. An alternative method is introducing a metamorphic buffer layer [30] where the lattice constant is gradually changed in a series of graded steps from that of the bottom layer to that of the desired top layer. Whilst effective this process is time consuming and the inclusion of a thick (a few microns) buffer layer into the structure design is not always appropriate.

2.1.5 Multiple quantum well and superlattice structures

Whilst a bulk structure features a single layer of active material, a multiple quantum well (MQW) structure has numerous alternating layers of two (or more) materials of different band gap. If the layers in the heterostructure are sufficiently thick that the electrons and holes present in one layer do not interact with those in neighbouring layers, that is that the carriers and their wavefunctions are confined in the direction of growth, then a Multiple Quantum Well (MQW) structure has been formed. If the layer thicknesses are reduced to be sufficiently thin, the wavefunctions of the confined carriers overlap, and the MQW structure is deemed to transition into a Superlattice structure [31]. The presence of strain in the layers caused by the alternating different materials forms strained – layer superlattice (SLS) structures. The distinction between MQW and superlattice can be confirmed by consideration of electron – hole wavefunction overlapping, density of states (DOS) and energy levels.

2.1.6 Electron – hole wavefunction overlap

The wavefunction overlap is proportional to the matrix element M, which can be used as a figure of merit to compare different structures. As light propagates through the QW structure, photons are emitted by electrons of energy $\mathrm{E_i}$ in an initial state $|\mathrm{i}\rangle$ in the conduction band recombining with holes to a final state $|\mathrm{f}\rangle$ of energy $\mathrm{E_f}$ in the valence band. The matrix element for this transition is defined as:

$$\mathrm{M} = \langle \mathrm{f}|\mathrm{x}|\mathrm{i}\rangle = \int \Psi_\mathrm{f}^*(\mathrm{r})\,\Psi_\mathrm{i}(\mathrm{r})\mathrm{d}^3\mathrm{r} \tag{2.15}$$

which can be separated into two terms:

$$\mathrm{M} = \mathrm{M_{cv}}\mathrm{M_{nn'}} \tag{2.16}$$

where $\mathrm{M_{cv}}$ is the valence – conduction band dipole moment:

$$\mathrm{M_{cv}} = \langle \mathrm{u_c}|\mathrm{x}|\mathrm{u_v}\rangle \tag{2.17}$$

and $\mathrm{M_{nn'}}$ is the electron – hole wavefunction overlap:

$$\mathrm{M_{nn'}} = \langle \mathrm{en'}|\mathrm{hn}\rangle = \int_{-\infty}^{\infty} \psi_{\mathrm{e_{n'}}}^*(\mathrm{z})\psi_{\mathrm{h_n}}(\mathrm{z})\,\mathrm{dz} \tag{2.18}$$

Since electric dipole transitions between the conduction and valence bands are strongly allowed then it can be assumed that $\mathrm{M_{cv}}$ is non – zero, hence the matrix element M for optical transitions is simply proportional to the overlap of the electron and hole states [32]. Considering the ground state transition, electrons in the $\mathrm{n'} = 1$ state in the conduction band recombine with holes into the $\mathrm{n} = 1$ lowest state in the valence band. Furthermore, the wavefunction overlap can be considered for a single period (P) of the periodic SL structure spanning from $\mathrm{z} = -\frac{\mathrm{P}}{2}$ to $\mathrm{z} = +\frac{\mathrm{P}}{2}$ containing a single QW region. Thus, the expression for the electron-hole wavefunction overlap can be simplified:

$$\mathrm{M_P} = \langle \mathrm{e}|\mathrm{h}\rangle = \int_{-\mathrm{P}/2}^{+\mathrm{P}/2} \psi_{\mathrm{e_1}}^*(\mathrm{z})\psi_{\mathrm{h_1}}(\mathrm{z})\,\mathrm{dz} \tag{2.19}$$

2.1.7 Density of States

Quantum structures confine the movement of free carriers to different degrees, for example inside a quantum well (QW) they are confined in two dimensions. The possible energies and wavefunctions of these constrained carriers are found by solving the Schrodinger equation:

$$-\frac{\hbar^2}{2m}\frac{d^2\psi}{dz^2} + U(z)\psi = e\psi \tag{2.20}$$

For a quantum well of width L and infinite depth, the energy of the n^{th} energy level is calculated as:

$$E_n = \frac{\hbar^2}{2m}\left(\frac{\pi}{L}\right)^2 n^2 \tag{2.21}$$

The energy of the lowest level is defined by the band gap of the material of the QW, and the quantization energies of the ground levels:

$$E_1 = E_g^{QW} + E_{e1} + E_{hh1} \tag{2.22}$$

The density of states (DOS) function indicates the number of states available to be occupied at each energy level in a system. A large DOS value indicates many states can be occupied; conversely, a low value means few states are available. It is necessary for determining the concentration and energetic distribution of carriers within semiconductor materials, in which the free motion of carriers is restricted to two, one or zero spatial directions depending on the structure. Quantum wells confine carriers in 2D, with quantum wires and quantum dots confining carriers in 1D and 0D respectively. The DOS in a bulk semiconductor, defined by Equation 2.23, is small near the band edge and increases with the square root of increasing energy [33] as shown by the curve in Figure. 2.9a.

$$\rho_E^{3D}(E) = 2\left(\frac{2\pi m k_B T}{h^2}\right)^{3/2} E^{1/2} \tag{2.23}$$

In a two – dimensional structure (i.e. quantum well) the DOS is step like (Figure 2.9b) with *n* representing the energy level, and is defined by:

$$\rho_E^{2D}(E)_{2D} = \frac{m^* n}{\pi \hbar^2} \tag{2.24}$$

It is significant that the 2D DOS is independent of energy. In quantum wires and quantum dots the free carriers are additionally confined, in two and three dimensions respectively [33]. The 1D DOS for quantum wires and 0D DOS for quantum dots (Fig. 2.9 c & d) are defined by Equations 2.25 & 2.26, which are stated here for completion but not elaborated upon in this section as the work relates exclusively to quantum well structures.

$$\rho_E^{1D}(E) = \sum_n \sum_m \frac{1}{2\pi} \left(\frac{2m}{\hbar^2}\right)^{1/2} n_{q-wire} \left(E - E_{n,m}\right)^{1/2} \tag{2.25}$$

$$\rho_E^{0D}(E) = \sum_n \sum_m \sum_l 2 n_{q-dot} \delta(E - E_{n,m,l}) \tag{2.26}$$

The shapes of the different DOS depending on the dimensionality of the structures and their constraint on free carrier movement are shown in Figure 2.9.

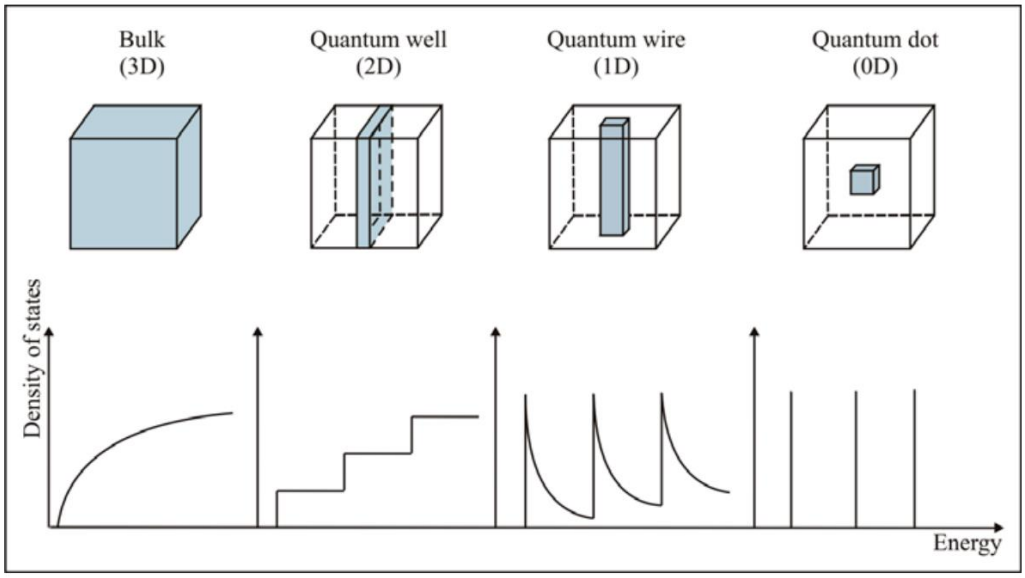

Figure 2.9 – Density of states (DOS) for semiconductor structures of different dimensions [34].

2.2 Electron – hole recombination

Within a material there are two types of free carriers – electrons and holes. In the absence of external stimuli such as incident light or applied electric current, at a set temperature, the product of the electron (n_0) and hole (p_0) concentrations is a constant defined as the intrinsic carrier concentration (n_i^2) [21]:

$$n_0 p_0 = n_i^2 \tag{2.27}$$

Additional free carriers $(\Delta n, \Delta p)$ can be generated by the material absorbing light. Under these conditions the total carrier concentrations are modified [21]:

$$n = n_0 + \Delta n \tag{2.28}$$

$$p = p_0 + \Delta p \tag{2.29}$$

The probability of an electron and hole recombining is proportional to both the concentration of electrons and the concentration of holes. Thus, the recombination rate can be defined as [21]:

$$R = -\frac{dn}{dt} = -\frac{dp}{dt} = Bnp \tag{2.30}$$

where the proportionality constant B is called the bimolecular recombination coefficient, with typical values of $\approx 10^{10}$ cm^{-3} / s for direct gap bulk semiconductors and of $\approx 10^{13}$ cm^{-3} / s for indirect gap bulk semiconductors [33].

2.2.1 Radiative recombination processes

The recombination of an electron and a hole is a radiative process if the energy of the electron is converted to a photon (of energy equal to the band gap). There are different radiative electron – hole recombination processes that can occur within a semiconductor material, as shown in Figure 2.10. These are band to band, band to donor or to acceptor, donor to acceptor, and excitonic, which are discussed in turn.

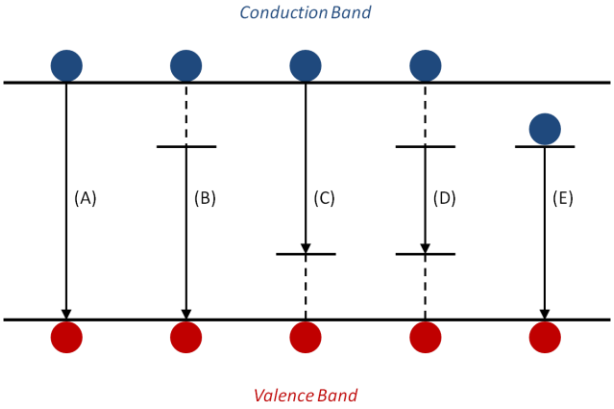

Figure 2.10 – Schematic of the different radiative recombination processes: (A) band-to-band, (B) donor-to-band, (C) band-to-acceptor, (D) donor-to-acceptor, (E) excitonic. Blue circles represent electrons and red circles represent holes, black arrows represent photon emission, black dashed lines represent phonon emission.

Band – to – band recombination

An electron in the conduction band recombines with a hole in the valance band, with the excess energy taking the form of a photon with an average energy of:

$$E_{photon} = E_g(T) + \frac{k_B T}{2} \qquad (2.31)$$

where $E_g(T)$ is the band gap of the material at temperature T, k_B is Boltzmann's constant, and the $k_B T/2$ term accounts for thermal effects. In a direct gap semiconductor material, the electron transition occurs at the same point in k – space, requiring negligible change in momentum. In an indirect gap semiconductor material, the bottom of the conduction band and the top of the valence band occur at different points in k – space. Band – to – band recombination is therefore less likely in indirect gap semiconductor materials since the process needs to include a phonon in addition to a photon to conserve momentum and energy.

Donor – to – band / band – to – acceptor recombination

An electron from the donor level recombines with a hole in the valence band, with the excess energy taking the form of a photon with an average energy of:

$$E_{photon} = E_g(T) - E_i + \frac{k_B T}{2} \qquad (2.32)$$

where E_i is the binding energy of the donor. The vacant donor site remains positively charged until an electron from the conduction band fills the vacancy via a phonon interaction. Band – to – acceptor recombination is a similar process, where an electron recombines with a hole in the acceptor level, with E_i the binding energy of the acceptor. These two types of recombination usually occur at low temperatures as the donor / acceptor states are merged into the conduction / valence band states as temperature increases.

Donor – to – acceptor recombination

Recombination can occur between donor and acceptor states if there are sufficiently high concentrations of impurities. In this case the photon energy is:

$$E_{photon} = E_g(T) - (E_D + E_A) + \frac{e^2}{4\pi\varepsilon_0\varepsilon_r r} \qquad (2.33)$$

where E_D and E_A are the donor and acceptor ionisation energies. The final term describes the coulomb attraction between the carriers in the donor and acceptor states.

Exciton recombination

Electrons and holes can bind to form Excitons which later decay and the carriers then undergo radiative recombination. Excitons are discussed further in Section 2.3.

2.2.2 Non – radiative recombination processes

The recombination of an electron and a hole may not generate a photon, but instead the energy released is transferred to vibrate the lattice atoms, i.e the energy is converted into phonons. The main causes of free carriers recombining non – radiatively is Auger processes or structural defects such as foreign atoms or dislocations [21].

LED device performance is compromised by non – radiative recombination processes which are temperature dependent and thus are particularly detrimental at high temperatures (above ≈ 100 K). The intensities of photoluminescence and electroluminescence emission are observed to decrease with rise of temperature. The non – radiative Shockley Read Hall (SRH) and different Auger recombination processes are discussed in this section.

Auger recombination processes

The main factor compromising LED performance is widely considered to be the occurrence of non – radiative Auger recombination processes [35]. Energy released by the recombination of an electron and hole does not produce a photon but instead is transferred to a third particle, exciting it to a higher energy state, where it then loses the energy in a non – radiative way (a photon is not produced). The four main Auger processes are CHCC, CHHH, CHLH, and CHSH. These abbreviations are based on the first letters of the bands involved, for example the CHCC process involves three electrons in the conduction band and one hole in the heavy hole band [36]. Figure 2.11 shows schematics of these Auger processes.

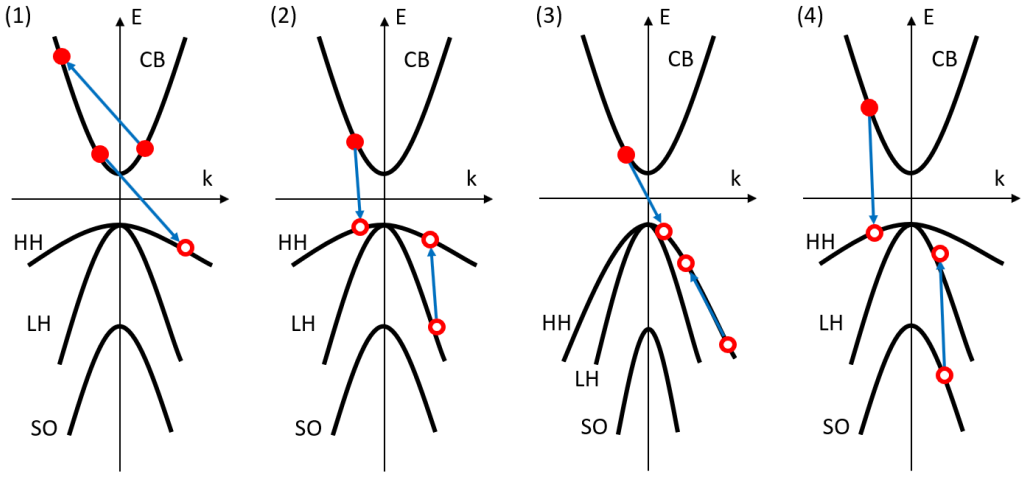

Figure 2.11 – Schematic of the different non-radiative Auger recombination processes involving the conduction band (CB) and the three valence bands of heavy hole (HH), light hole (LH) and spin-orbit split-off (SH). The four processes are (1) CHCC, (2) CHLH, (3) CHHH, (4) CHSH.

In the CHCC process two electrons collide, one recombining with a hole and releasing energy that excites the other electron up the conduction band, with this electron then loses its energy via rapid phonon emission. The CHCC process is dominant in an n – type material which has an excess of electrons. The other three Auger processes all involve one electron and two holes, and so occur predominantly in p – type materials that have an excess of holes. In the CHLH process an electron recombines with a heavy hole and the energy released enables a hole to move from the light hole band to the heavy hole band. In the CHHH process, the recombination of an electron with a heavy hole releases energy that promotes a heavy hole to a higher valence state. In the CHSH process, recombination of an electron with a heavy hole produces energy to raise a hole from the split off band up to the heavy hole band.

Auger recombination is dominant in semiconductor materials with a small band gap. Materials with a large band gap normally have a large electron effective mass so in

an Auger process there would be a large transfer of momentum, necessitating that holes must be in high energy states, which is unlikely. In small band gap materials, the electron effective mass is small, with the holes at lower energy, increasing the probability of an Auger process occurring. The Auger recombination rate is proportional to Cn^3 where C is the Auger coefficient and n the carrier density which has a cubic dependence due to the processes involving three carriers (two electrons and one hole, or one electron and two holes). Auger recombination is known to be strongly temperature dependent and follows the general relation:

$$\mathrm{R_{Auger}} \propto \exp\left(-\frac{\mathrm{E_a}}{\mathrm{k_B T}}\right)\mathrm{T}^3 \tag{2.34}$$

where $\mathrm{E_a}$ is the activation energy for the corresponding Auger process and the exponential term dominates. Specific Auger processes each have their own activation energies (which can be controlled by the effective masses of the free carriers) where the CHCC and CHSH processes have activation energies given by:

$$\mathrm{E_a^{CHCC}} = \frac{\mathrm{m_e^* E_g}}{\mathrm{m_e^* + m_{hh}^*}} \tag{2.35}$$

$$\mathrm{E_a^{CHSH}} = \frac{\mathrm{m_{SO}^*}}{\mathrm{m_e^* + 2m_{hh}^* - m_{SO}^*}}\left(\mathrm{E_g} - \Delta_{\mathrm{so}}\right) \tag{2.36}$$

where $\mathrm{E_g}$ is the band gap energy, Δ_{so} is the spin orbit splitting energy, and $\mathrm{m_e^*}$, $\mathrm{m_{hh}^*}$, $\mathrm{m_{SO}^*}$ are the effective masses of the electrons, holes in the heavy hole band and holes in the split off band respectively. It is possible to determine if CHSH is the dominant Auger process using the expression:

$$\frac{(\mathrm{E_T} - \Delta_0)/\mathrm{E_T}}{\mathrm{m_e^*/m_{SO}^*}} > 1 \tag{2.37}$$

such that the CHCC process is dominant when this condition is satisfied. ($\mathrm{E_T}$ is the transition energy corresponding to $e_1 – hh_1$ recombination).

Auger processes can be suppressed by limiting the density of final states available to the third non – recombining carrier and avoid inter – valance band resonances [7]. Most type II antimonide – based QW structures have larger conduction and valence band offsets compared to type I structures possessing the same energy gap, such that they tend to have confined final Auger states opposed to delocalised states, meaning that suppression of Auger processes is more easily achievable in type II structures [37]. The activation energy of Auger processes can be estimated from experimental data of change in PL peak intensity with temperature, by fitting according to the Arrhenius equation (Equation 2.38) in which I is the PL peak intensity with I_0 the predicted intensity at 0 K, A is the rate of the Auger process and E_a is the activation energy:

$$I = \frac{I_0}{1+Aexp^{-Ea/k_BT}} \tag{2.38}$$

Shockley – Read – Hall (SRH) recombination

The Shockley Read Hall (SRH) process concerns the recombination of free carriers located at defects or in trapped states. Defects in the active region can form in different ways – either during the growth process as a result of excessive strain build – up or arise from inherent impurities or dislocations present in the materials. The rate of SRH recombination is defined as:

$$R = A_{SRH}n \tag{2.39}$$

where n is the concentration of free carriers, and A is the SRH coefficient defined by Equation 2.40 with τ_0 the minority carrier lifetime:

$$A_{SRH} = {}^{1}/_{2\tau_0} \tag{2.40}$$

Surface recombination

The abrupt change of material at the interfaces between layers in a heterojunction structure generates defects in the lattice that leads to dangling bonds which can bind impurity atoms during growth. These impurity states increase the possibility of non – radiative recombination of free carriers. The surface recombination rate is dependent on the rate at which minority free carriers move towards the surface, which in semiconductors is on the order of 1 x 10^7 cm / second. The p – n junction should be at a distance away from the surface of at least three times greater than the diffusion length of the involved free carriers to minimise non – radiative recombination via impurities at the surface [33]. Surface passivation is a post growth technique that acts to eliminate dangling bonds and reduce impurities incorporated within the structure.

2.3 Excitons

Excitons are electrically – neutral quasiparticles formed by an electron and hole bound together by coulomb attraction rather than recombining. The exciton can be visualised in the simplest way as a hydrogen – like atom with an electron and hole in stable orbit around each other. Excitons exist as two basic types, either as free excitons (Wannier – Mott excitons) or as bound excitons (Frenkel excitons) [31].

A free exciton produces a photon with energy:

$$E_{photon} = E_g - E_{eh} \tag{2.41}$$

where E_{eh} is the energy required to separate the electron – hole pair, which is typically a few meV.

A bound exciton, created by the binding of an exciton to an atom or defect energy state in the material, produces a photon with energy:

$$E_{photon} = E_g - E_{eh} - E_b \tag{2.42}$$

where E_b is the energy binding the exciton to the associated impurity state.

The emission peak from a bound exciton is narrower than that of a free exciton as there is no contribution from kinetic energy due to it being in a fixed position.

The exciton binding energy E_b is defined as the energy difference between the excitonic emission peak and the peak of electron – hole recombination [38]:

$$E_b = E_{e-h} - E_x \tag{2.43}$$

A value for the binding energy of an exciton can be calculated theoretically by Equation 2.47 where α is the dimension of the system (α = 2 - 3 for QWs depending on the degree of coupling) and E_0 is the exciton energy (Equation 2.44 where E_H is the Rydberg energy). The exact α value is obtained from Equation 2.45 with a_x the exciton Bohr radius (defined by Equation 2.46) and L the width of the QW.

$$E_0 = \frac{\mu E_H}{m_0 \varepsilon^2} \tag{2.44}$$

$$\alpha = 3 - exp\left(-\frac{L}{2a_x}\right) \tag{2.45}$$

$$a_X = \frac{m_0 \varepsilon a_H}{\mu} \tag{2.46}$$

$$E_b = \left(\frac{2}{\alpha - 1}\right)^2 E_0 \tag{2.47}$$

Stable excitons will only be formed if the attraction between the electron and hole is enough to protect the excitons against breakup by colliding phonons, a condition satisfied for an exciton binding energy greater than $k_B T$ [31].

At low temperature the majority of electrons and holes exist bound in excitons, but with increasing carrier density or temperature excitons ionize and release free carriers which rapidly produce further exciton ionization by screening of the Coulomb interaction that binds the remaining excitons together [39, 40, 41, 42]. The Mott transition [43] is a first order phase transition which defines the change from an electrically insulating exciton population to conducting electron – hole plasma in a system of correlated electrons [1]. This crossover point continues to be the subject of much active research especially as both experimental and theoretical studies report conflicting views on whether the nature of this transition is abrupt [40, 44, 45] or gradual [46, 47, 48, 49].

The critical free carrier density η_c corresponding to the Mott transition can be estimated theoretically using Equation 2.48 based on a plate – capacitor model [38, 50] with inputs of QW separation (*d*, fixed value based on the structure) and exciton energy shift (*ΔX*, determined from the experimental data).

$$\eta_c = \frac{\Delta X \varepsilon}{e^2 d} \tag{2.48}$$

Alternatively, the experimental Mott density can be estimated by multiplying the laser power fraction at which the Mott transition is identified to occur with the injected carrier density provided by the laser. This is calculated by Equation 2.49:

$$N = \frac{I \alpha \tau}{h\nu} \tag{2.49}$$

with I the laser power, α the absorption coefficient of the material, and τ the decay rate of the free carriers.

Excitons formed inside a quantum well (QW) are confined (Figure 2.12) forcing the electron and hole closer together, resulting in a larger exciton binding energy than in bulk materials. Experimentally this means radiative emission from excitons should exhibit greater intensity and be observable at higher excitation power or higher temperature in a QW structure. The exciton Mott transition in two – dimensional GaAs/AlGaAs systems has been found to occur at electron – hole pair densities of ≈ 10^{10} cm^{-2} and temperatures of ≈ 10 K [39, 49]. In indirect exciton systems where the electrons and holes are spatially separated in adjacent quantum wells, the small spatial overlap between the quasi – particles leads to a weaker Coulomb interaction and a long radiative lifetime compared to a spatially direct exciton [38].

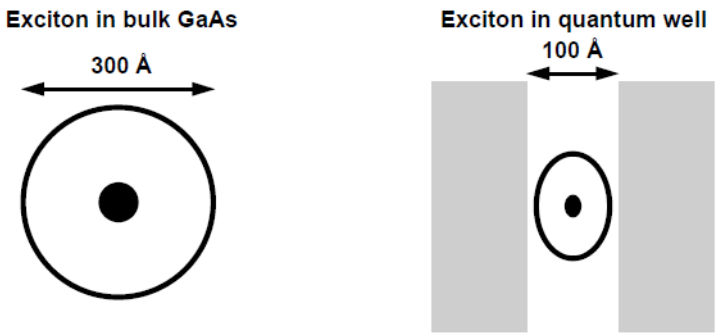

Figure 2.12 – Schematic showing excitons sizes in bulk material and confined inside quantum well [51].

Furthermore, the existence of biexcitons (a bound pair of excitons) in QW structures has been indicated by theoretical predictions [50] and observed experimentally in photoluminescence spectra [52]. The possibility of biexciton formation can be derived by Equation 2.50 (represented in Figure 2.13) [50]:

$$\frac{d}{a_X} = \sigma \qquad (2.50)$$

where d is the charge separation (the QW separation), a_X is the exciton Bohr radius, and σ is the effective mass ratio m_e^*/m_{hh}^*.

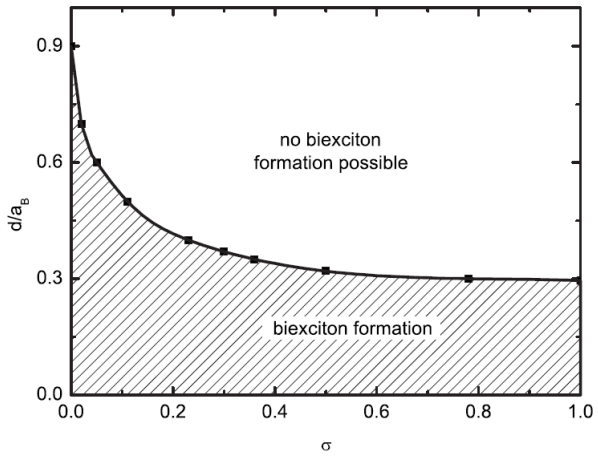

Figure 2.13 – Condition for biexciton formation in semiconductor structures, which is dependent on the separation of the charges, exciton Bohr radius and mass ratio.

2.4 Luminescence

Luminescence is the emission of light from a material due to the application of energy from an external source e.g. laser. In semiconductor materials this luminescence occurs from the recombination of electrons and holes releasing energy in the form of photons. Two ways this process is generated are photoluminescence (PL) and electroluminescence (EL) which are both commonly used to characterise structures and devices.

2.4.1 Photoluminescence

Photoluminescence (PL) is a process used to investigate the optical properties of materials. A laser source produces light of energy greater than the band gap of the subject material, which is directed onto the surface of the sample. This light is

absorbed, and the energy of the photons excites an electron from the lower energy valence band into the higher energy conduction band, creating an electron – hole pair. Numerous electron – hole pairs are generated, with the rate of photon absorption determined by an absorption coefficient. The generated carriers (electrons and holes) can move through the material until meeting and recombining with a carrier of opposite charge occurs (i.e. an electron with a hole, or vice versa). If this process is radiative then light emission occurs, otherwise the recombination is non – radiative. With increasing temperature, the photoluminescence intensity is observed to decrease, due to a number of factors. The rise of temperature provides extra energy such that the holes can leak out of the QWs and reside in the valence band of the barrier layers, which can then undergo radiative recombination at a larger energy (shorter wavelength emission) directly across the barrier layers. The rate of radiative recombination between carriers in the active region scales as n^2 whereas the rate of non – radiative Auger processes scales as n^3, meaning as more carriers are excited by the temperature rise a greater proportion of them will recombine non – radiatively. The greater the decrease of photoluminescence intensity with increased temperature, the larger the proportion of free carriers which are undergoing non – radiative recombination rather than radiative recombination. Optimisation of devices designed to operate at high temperatures focuses on engineering the active region such that the possibility of non – radiative recombination is minimised (as well as optimising the rate of radiative recombination).

2.4.2 Electroluminescence

Electroluminescence (EL) is similar to PL but used to analyse the performance of devices rather than standalone samples of materials. A voltage applied through metallic contacts of the device provides the direct injection of carriers into the structure. The LED device is based on a p – n junction (described in Section 2.5) such that electrons build up in the n – type side and conversely holes in the p – type side. These carriers then move in opposite directions through the structure and upon meeting recombine in either a radiative or non-radiative process similarly to PL. LED efficiency is influenced by factors including competing radiative and non – radiative recombination processes, carrier mobility and diffusion lengths, electrical resistance, current crowding and carrier leakage, which are understood through EL analysis [33].

2.5 The p – n junction & light – emitting diodes

Light – emitting diodes rely on the p – n junction in which the flow of free carriers (electrons and holes) facilitates the emittance of photons (light) via radiative recombination processes of these free carriers.

2.5.1 The p – n junction

A schematic energy band diagram of a p – type (high hole density) layer next to an unconnected n – type (high electron density) layer is shown in Figure 2.14, showing the modified positions of the Fermi levels due to the doping. When the two semiconductor layers are joined together, the Fermi level (E_F) must be constant throughout the structure. Therefore, the energy band diagram (Figure 2.14) is amended to that shown in Figure 2.15 to satisfy this condition.

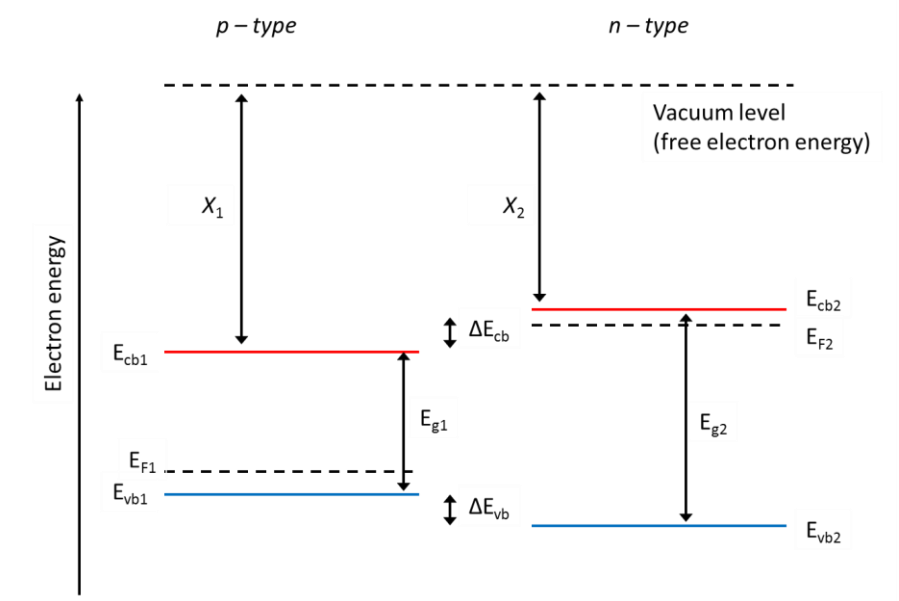

Figure 2.14 – Schematic energy band diagram showing separated *n* - type and *p* - type layers.

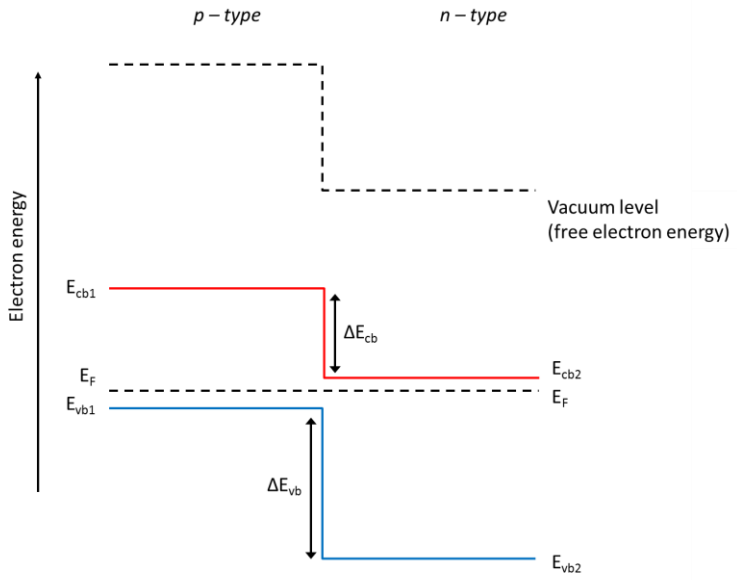

Figure 2.15 – Schematic energy band diagram showing joined *n* - type and *p* - type semiconductor layers with aligned Fermi level.

The large difference in carrier concentration between the two layers generates a diffusion current across the structure. Electrons in the *n* – type region and the holes in the *p* – type region move in opposite directions across the interface. These carriers will eventually undergo recombination with a particle of opposite charge, i.e a

(negatively charged) electron will recombine with a (positively charged) hole. The diffusion length is the average distance a free carrier travels before undergoing recombination. This is defined for electrons and holes by Equations 2.51 & 2.52 respectively, with D_n, D_p the diffusion constants (inferred from carrier mobility) and τ_n, τ_p are the electron and hole carrier lifetimes.

$$L_n = \sqrt{D_n \tau_n} \tag{2.51}$$

$$L_p = \sqrt{D_p \tau_p} \tag{2.52}$$

In typical semiconductors, the diffusion length is several micrometres [21]. In III – V semiconductor materials the diffusion length of electrons is significantly longer than holes, meaning electroluminescence usually occurs with the *p* region of the p – n junction. The diffusion length is longer in narrow band gap semiconductors such as InAs compared to GaAs, meaning the issue of interface or surface non – radiative recombination is more problematic as the carriers can travel further [53].

The movement and subsequent recombination of the free carriers results in the formation of a depletion region centred around the interface, containing only immobile charged ions. Within this depletion region an electric field is created that opposes carrier diffusion, modifying the p – n structure such that the conduction and valence bands bend across the depletion region between the two highly charged regions. The amount of band bending depends on several factors – the composition of the materials of the two layers, the concentration of the carriers, the position of the Fermi level which is affected by the concentration of impurities, the operating temperature of the device, and the application of a bias voltage [33]. This charge present inside the depletion region is defined as the diffusion voltage [21]:

$$V_D = \frac{k_B T}{e} ln\left(\frac{N_A N_D}{n_i^2}\right) \quad (2.53)$$

where N_A, N_D are the acceptor and donor concentrations, and n_i is the intrinsic carrier concentration of the material. The diffusion voltage represents the energy requirement for free carriers to move across the neutral depletion region and into the oppositely charged region on the other side.

Figure 2.16 shows a schematic diagram of the p – n junction under zero applied bias.

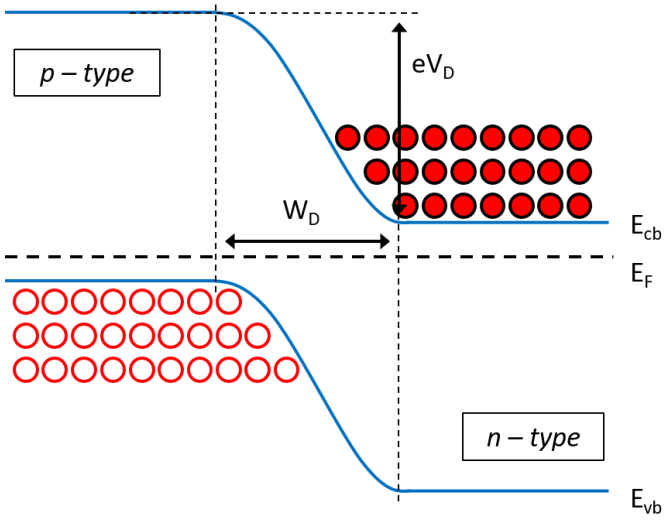

Figure 2.16 – Schematic of p-n junction under zero applied current, showing the high concentrations of electrons and holes in the n - type and p - type regions respectively, either side of the neutral depletion region which the free carriers need to energetically overcome to move across into the region of opposite charge.

2.5.2 LED operation

A light emitting diode is based on a p – n junction (Fig. 2.16) operated in forward – bias mode where an applied electric current injects electrons and holes into the oppositely charged regions. The depletion region is highly resistive due to the absence of free carriers such that the applied voltage drops across it which results in the diffusion voltage, the energy required for carriers to travel across the diffusion region, being reduced as shown in Figure 2.17. This facilitates an increase in current flow through the device.

The current voltage (I – V) characteristic of a p-n junction is defined by the Shockley equation, which under typical forward bias conditions is expressed by Equation 2.54 [21]. The exponential term indicates that as the voltage approaches the diffusion voltage the current significantly increases, with the threshold voltage defined as the voltage at which $V \approx V_D$ and a significant increase in the current occurs.

$$I = eA\left(\sqrt{\frac{D_n}{\tau_n}N_D} + \sqrt{\frac{D_p}{\tau_p}N_A}\right)e^{e(V-V_D)/k_BT} \qquad (2.54)$$

As shown in Figure 2.17 the applied voltage reduces the energy difference between the conduction bands the between the valence bands, resulting in the Fermi level becoming discontinuous across the structure.

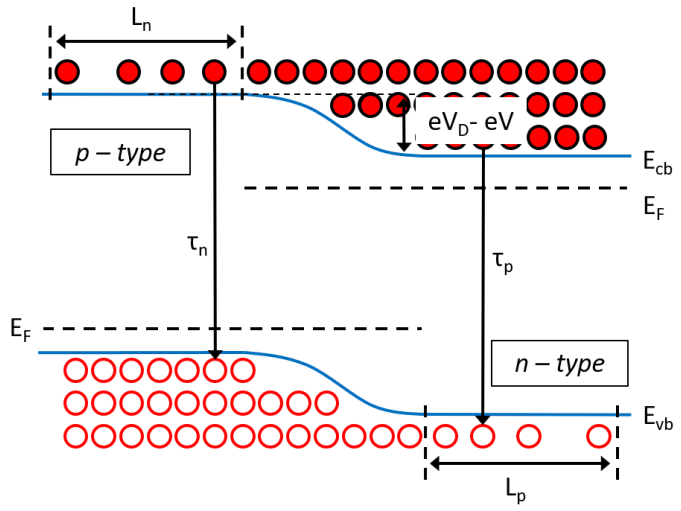

Figure 2.17 – Schematic of the p – n junction under forward bias, showing the effect of the applied voltage reducing the energy difference between the two highly charged regions, thus enabling free carriers to more easily move across the diffusion region to undergo recombination with those of opposite charge.

The energy difference between the Fermi level and the conduction band on the n - type side is defined as [21]:

$$E_{cb} - E_F = -k_B T \ln\left(\frac{n}{N_D}\right) \tag{2.55}$$

Similarly, the energy difference between the Fermi level and the valence band on the p – type side is defined as:

$$E_F - E_{vb} = -k_B T \ln\left(\frac{p}{N_A}\right) \tag{2.56}$$

The separation between the Fermi level and the relevant band edges is small compared with the band gap energy ($E_{cb} - E_F \ll E_g$ and $E_F - E_{vb} \ll E_g$) in highly doped semiconductors [21]. Furthermore, since these values only exhibit weak dependence on the doping concentration, the diffusion voltage can be approximated by a simple expression of band gap energy divided by the elementary charge [21]:

$$V_D \approx E_g/e \tag{2.57}$$

2.5.3 Heterojunction LED

Considering that the rate of radiative free carrier recombination is proportional to the concentrations of electrons and holes (Eqn. 2.30) it is apparent that a large recombination region is not conducive to achieving a high rate. The employment of a double heterojunction structure for the active region acts to trap carriers in the layers of the small band gap material in between barrier layers of wider band gap material, restricting their propagation through the structure. This is shown in Figure 2.18. In a heterojunction device, in contrast to a homojunction device, the thickness of the region in which the carriers recombine is defined by the thickness of the active region not the diffusion length. As the layer thicknesses are on the order of nanometres, compared to several microns for the carrier diffusion lengths, the concentration of free carriers in the active region is significantly increased. The significantly higher rate of free carrier radiative recombination is the reason why high efficiency LEDs feature the double heterostructure / quantum well design [21].

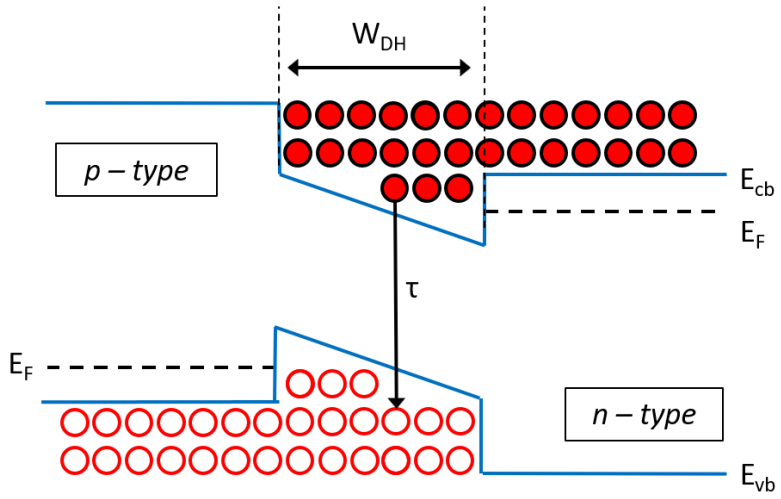

Figure 2.18 – Schematic of the heterojunction LED structure, showing the trapping of carriers in the "quantum well" regions made of narrow band gap material, which acts to significantly increase the carrier concentration in the device active region and thus increase the rate of radiative carrier recombination.

2.5.4 Cascade structured LED

The reduced energy of photons at infrared wavelengths compared to those in the visible region presents an inherent difficultly in achieving high power devices. One idea to address this issue is the cascade structure (Figure 2.19) where electrons cascade through the structure by passing through multiple active regions at progressively decreased energies. This results in a single electron undergoing multiple inter – sub – band transitions in the conduction band, producing numerous photons, thus increasing the overall emission intensity from the device. In theory, the electrons can emit as many photons as active regions encountered [54]. Cascade structures have been successfully incorporated as the active region in mid – infrared LEDs (Section 3.5.1) but are compromised by high energy requirement for operation.

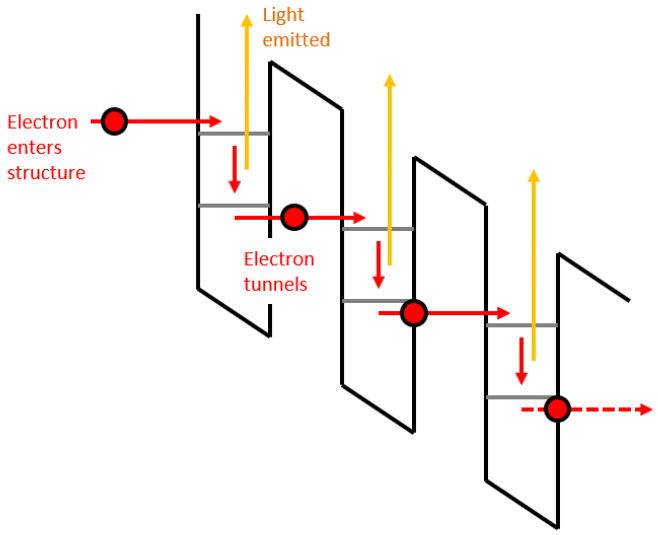

Figure 2.19 – Schematic of cascade structure in which electrons recombine with numerous holes to maximise the radiative e – h recombination rate.

2.5.5 LED efficiency

The internal quantum efficiency of an LED is defined as the number of photons emitted from the active region compared to the number of electrons injected into the device. This can be calculated by knowing the injection current (I), light extraction efficiency (η_{opt}), output power emitted from the active region (P_{int}) of the LED, and the energy (hv) of the electroluminescence emission peak [21, 33]:

$$\eta_{int} = \frac{n_\gamma}{n_e} = \frac{P/hv}{I/e} \tag{2.58}$$

An ideal LED would emit one photon for every one electron injected ($\eta_{int} = 1$). However, in reality not all of the photons generated are emitted into free space, as a proportion are lost for example through absorption in the substrate or at a metallic contact. Additionally, the phenomenon of total internal reflection reduces the ability of the photons to escape, which are leaving the active region at a range of angles.

The light extraction efficiency is defined as the number of photons emitted into free space as a proportion of the total photons emitted from the active region [21]:

$$\eta_{opt} = \frac{n_{\gamma\_out}}{n_{\gamma\_total}} = \frac{P/hv}{P_{int}/hv} \tag{2.59}$$

The light extraction efficiency can be estimated by [33]:

$$\eta_{opt} = \frac{1}{n(n+1)^2} \tag{2.60}$$

where n is the refractive index of the semiconductor material of the device active region. Since the refractive index of InAs is ≈ 3.5 for low – antimony InAs / InAsSb structures this value can be estimated as η_{opt} = 1.4 %.

The external quantum efficiency (η_{ext}) is defined as the number of photons emitted into free space compared to the number of electrons injected into the LED. This value depends on the carrier injection efficiency (η_{inj}), internal quantum efficiency (η_{int}), and the light extraction efficiency (η_{opt}) [33]:

$$\eta_{ext} = \eta_{int} \times \eta_{inj} \times \eta_{opt} \tag{2.61}$$

The value of η_{inj} is usually taken to be 1 assuming 100 % efficiency of injecting the carriers into the device. Additionally, the power efficiency (η_{power}) is defined as P/IV where IV is the electrical power provided to the LED, and therefore is also called the 'wallplug efficiency' [21].

2.5.6 LED emission

LEDs emit light by spontaneous recombination of electrons and holes simultaneously producing photons, in contrast to the stimulated emission process of lasers [21]. Electrons in the conduction band, and holes in the valence band, are both assumed to have parabolic dispersion relations (Figure. 2.20) defined by Equations 2.62 & 2.63 where E_C & E_V are the conduction and valence band edges, and m_e^* & m_h^* are the effective masses of the electrons and holes [21].

$$E_e = E_C + \frac{\hbar^2 k^2}{2m_e^*} \tag{2.62}$$

$$E_h = E_V + \frac{\hbar^2 k^2}{2m_h^*} \tag{2.63}$$

Electrons and holes have an average kinetic energy of $k_B T$. Energy conservation requires that the photon energy is the difference between the energies of the electron and hole, such that the photon energy is approximately equal to the band gap of the material if the thermal energy is small $\left(k_B T \ll E_g\right)$ [21].

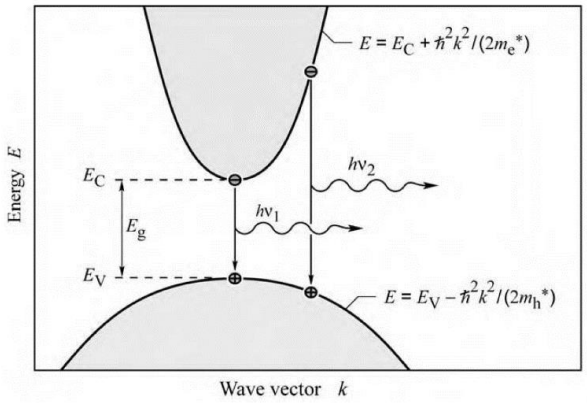

Figure 2.20 – Parabolic dispersion relations of electrons and holes, showing electron-hole recombination and the resulting photon emission.

The emission intensity of an LED with bulk active region can be defined by:

$$I(E) \propto \sqrt{E - E_g}\left(e^{-E/k_BT}\right) \qquad (2.64)$$

From Equation 2.64 the shape of the LED emission spectra can be theorised, as shown in Figure 2.21.

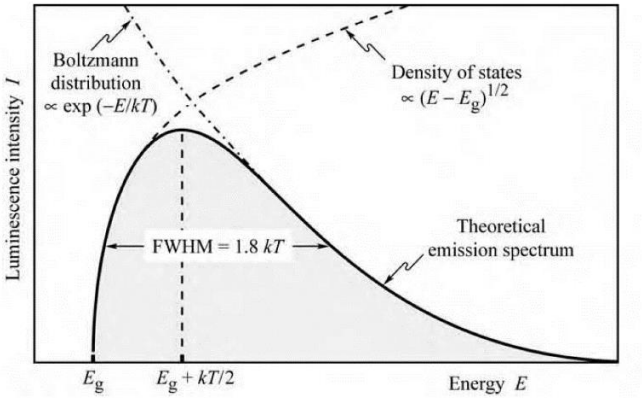

Figure 2.21 – Theoretical shape of the emission spectrum of a bulk LED.

The width of the emission spectra is important for example in the perception of the emission as monochromatic or for applications such as gas sensing that require a narrow emission to match precisely to gas absorption lines. The full – width at half – maximum (FWHM) of the emission, in energy or wavelength, is defined as:

$$\Delta E = 1.8 k_B T \tag{2.65}$$

$$\Delta \lambda = \frac{1.8 k_B T \lambda^2}{hc} \tag{2.66}$$

The intensity of emission from an LED decreases as the temperature increases, due to temperature – dependent factors such as non – radiative recombination of free carriers. This temperature dependence of the LED emission intensity can be described by Equation 2.67 [21] in which T_1 is the characteristic temperature, with a high value desirable as it implies there is a weak temperature dependence of the emission intensity.

$$I = I_0 \, e^{-\frac{T}{T_1}} \tag{2.67}$$

Z analysis provides further insight regarding the strengths of the different electron – hole recombination processes occurring inside the devices. The parameter Z is defined as the average number of free carriers per recombination process, and the value indicates the dominant process. A value of Z = 1 indicates SRH recombination, a value of Z = 2 that radiative recombination dominates, and a value of Z = 3 indicates a high rate of non – radiative Auger recombination. It is important to note that Z = 2 can alternatively be obtained if there are high rates of both SRH and Auger recombination processes. The Z value is calculated as a ratio of the natural logarithms of the drive current (I) and the emission intensity (L):

$$Z = 2\left(\frac{\ln I}{\ln L}\right) \tag{2.68}$$

Chapter 3

Literature review

This chapter presents an overview of the current literature relating to the InAsSb material and the development of InAs/InAsSb mid – infrared light – emitting diodes.

3.1 InAsSb

The InAsSb alloy is of specific interest in the development of semiconductor – based optoelectronic devices. This material exhibits the lowest room temperature band gap (Figure 3.1; E_g ≈ 0.1 eV for Sb ≈ 60 % [55]) of conventional III – V semiconductors [56, 57, 58, 59, 60] excluding those incorporating nitrogen [61, 62] or bismuth [63, 64]. The tailorability of the band gap by composition enables the realisation of light – emitting devices producing infrared emission up to λ ≈ 12 μm for a range of applications and the development of detectors operating in the λ = 8 – 12 μm range as an alternative to the conventional HgCdTe material [56, 58, 65, 66, 67, 68, 60].

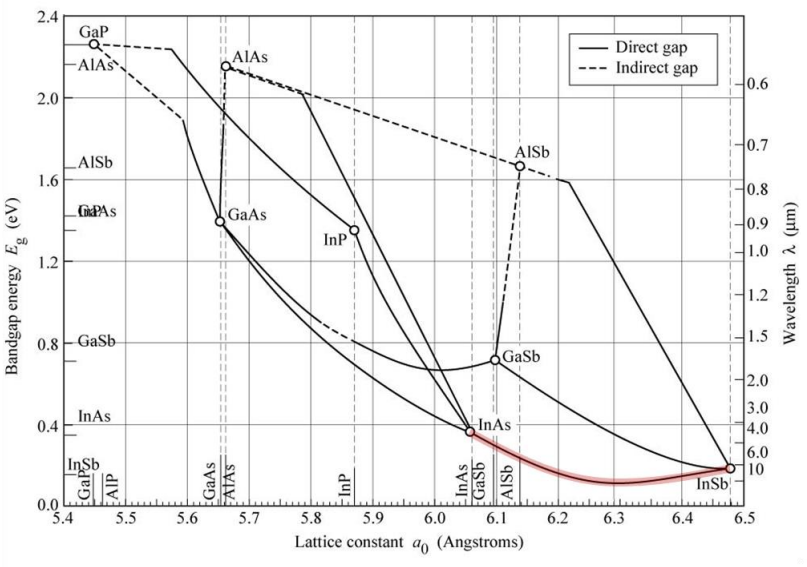

Figure 3.1 – Room temperature band gap energy versus lattice constant of III – V semiconductors, with the InAsSb alloy highlighted (red line) [21]. The minimum band gap of 0.1 eV is achieved for the alloy composition of Sb = 60 %.

Early studies of InAsSb focused on material of low antimony content [58] because the miscibility gap in the middle of the composition range prevented growth of InAsSb alloys with large antimony content using liquid phase epitaxy (LPE) which is an equilibrium growth technique. The subsequent development of molecular beam epitaxy (MBE) in the 1970s enabled the creation of quantum confined structures with better control of thickness and composition and uniformity and with well – defined interfaces. This made it possible to produce InAsSb over the full composition range and characterise the resulting photoluminescence [58, 68]. As shown in Figure 3.1 there is no suitable substrate enabling lattice matching to high antimony InAsSb alloys which is fundamentally detrimental to growth quality and optical properties [58, 20]. This sets a limitation on the layer thicknesses that can be grown before dislocations and defects occur which degrade the quality of the structure [4]. However, there are some advantages of such strained layer structures. Firstly, the presence of strain results in the possible further reduction of the band gap [56, 57]. Secondly, the strain breaks the degeneracy of the heavy hole and light hole valence bands which can help to suppress the rates of non – radiative Auger processes [69, 70, 71] as discussed in Section 2.2.2. Furthermore, As – rich InAsSb alloys have been shown to exhibit relatively low SRH recombination [72].

3.2 Bulk structure LEDs

The first bulk InAs LEDs were reported by Melngailis in 1966 [73, 74] which produced room temperature emission at λ = 3.7 µm. Bulk InAsSb LEDs were first reported in 1993 by Dobbelaere [75] with observation of a dip in the emission spectra at 4.3 µm corresponding to the absorption of atmospheric CO_2 (Fig. 3.2a) demonstrating the

suitability of the device for gas sensing. Demonstrations using InAs – based bulk structure LEDs for mid – infrared gas sensing have been reported for methane (CH_4) at 3.3 µm [76, 77], propane at 3.4 µm [78] (Figure 3.2b), carbon dioxide (CO_2) at 4.2µm [79, 80, 81, 76] and carbon monoxide (CO) at 4.6µm [76]. Furthermore, QinetiQ researchers [82] have reported bulk $Al_xIn_{1-x}Sb$ LEDs over the compositional range x = 0 – 8.8 % with emittance above 3.4 mW / cm^2 at appropriate wavelengths for CH_4, CO, CO_2, NO and NO_2 gas detection.

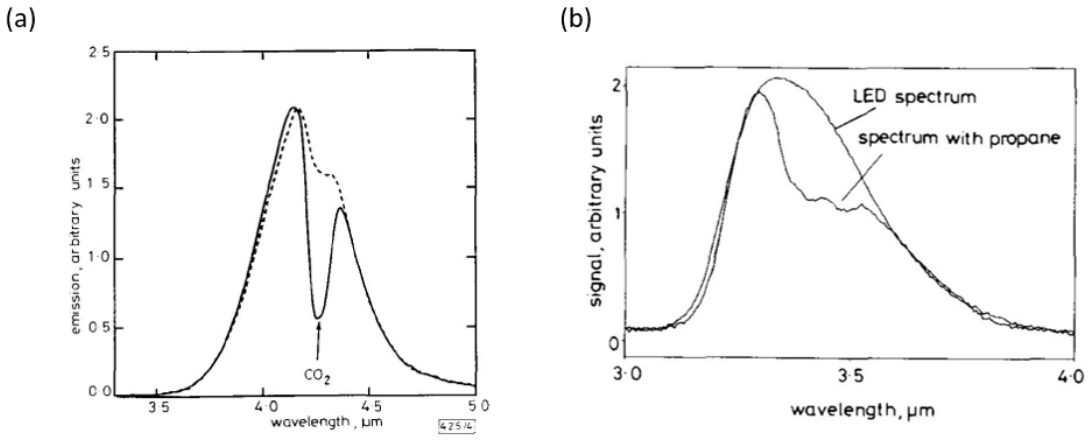

Figure 3.2 – Electroluminescence spectra from a) bulk $InAs_{0.85}Sb_{0.15}$ LED [75] and b) bulk InGaAs LED [78] devices showing the detection of CO_2 and propane by observation of significant dips in the emission spectra at λ = 4.3 µm and 3.4 µm corresponding to the fingerprint absorption of these gases.

Despite the successful realisation of devices for gas sensing, the simplicity of the bulk structure limits by its nature the ability to improve performance characteristics, with type I and type II structures offering a greater possibility to achieve enhancements of device output. These are discussed in the following sections.

3.3 Heterojunction LEDs

Heterojunction structures comprised of alternating layers of two or more materials offer additional tailorability over the emission properties. Furthermore, in contrast to

a bulk structure where the band gap of the device can only be changed by varying the composition of the material, the quantum well design is advantageous in enabling the band gap to be tuned by varying both the composition of the materials and the layer thicknesses. The type II InAs/InAsSb structure continues to attract interest because of the ability to tailor the band structure to target specific emission wavelengths as well as the potential to adjust electron – hole separation to reduce non – radiative Auger recombination and maximise the rate of radiative recombination [83, 70, 84, 85]. This makes the structure an excellent candidate for use in the active region of mid – infrared LEDs.

3.3.1 Single quantum well (SQW) LEDs

In the late 1990s the potential of type II InAs / InAsSb quantum well structures for mid – infrared LEDs was demonstrated by the Imperial College London research group [2, 3, 86, 87]. The emission spectra from two InAs/InAsSb single quantum well (SQW) LEDs containing Sb = 16.6 and 26 % [2, 87] are shown in Figure 3.3. These devices emitted at 5 and 8 µm with output powers of 50 and 24 µW (pulsed operation, 1.5 A at 20 kHz, 5 – 50% duty cycle) with corresponding internal efficiencies of 0.8 and 1.6 %.

The use of heterojunction LEDs containing a single QW in the active region comprised of different combinations of InAs – based semiconductor materials has been extensively demonstrated for mid – infrared gas sensing. This includes the detection of methane (CH_4) at 3.3 µm [88, 89, 90], formaldehyde (CH_20) at 3.6 µm [91], hydrogen sulphide (H_2S) at 3.7 µm [88], sulphur dioxide (SO_2) at 3.9 µm [92],

carbon dioxide (CO_2) at $\lambda \approx 4.2\mu m$ [93, 89, 94, 95, 96, 97], carbon monoxide (CO) at 4.6 μm [98, 95, 97, 14] and nitric oxide (NO) at 5.3 μm [89].

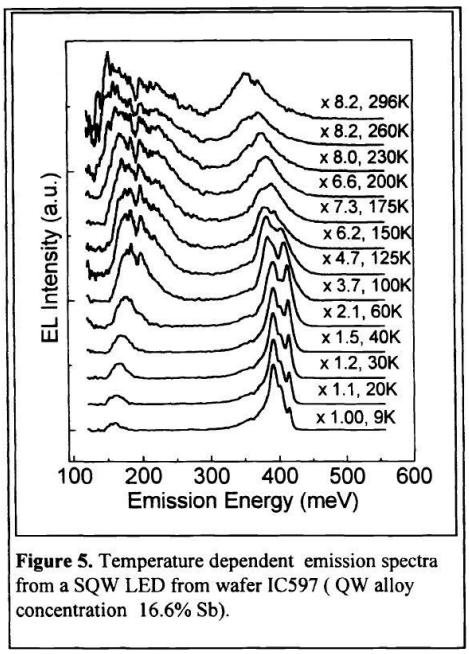

Figure 5. Temperature dependent emission spectra from a SQW LED from wafer IC597 (QW alloy concentration 16.6% Sb).

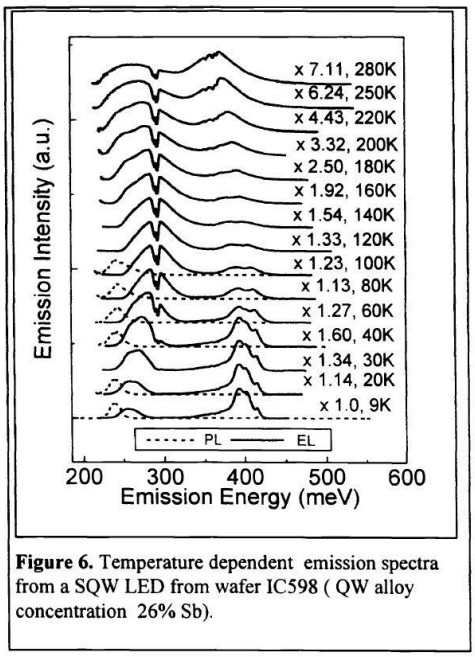

Figure 6. Temperature dependent emission spectra from a SQW LED from wafer IC598 (QW alloy concentration 26% Sb).

Figure 3.3 – Electroluminescence spectra from two InAs/InAsSb type II single quantum well (SQW) LEDs, producing emission up to room temperature with peaks at 5 and 8 μm [2].

3.3.2 Multiple quantum well (MQW) LEDs

LEDs with a multiple quantum well (MQW) active region possess benefits over those with a single quantum well or bulk structure. The additional number of QWs increases the possibility of propagating electrons to be captured, thus increasing the rate of radiative recombination with the holes confined in the QWs. Electroluminescence from type II InAs/InAsSb MQW LEDs over the 4 – 300 K temperature range has been shown to be dominated by e - hh transitions in the QWs [99, 7]. In addition to producing high intensity luminescence from increasing the radiative recombination of free carriers, the type II structure can be engineered to suppress non – radiative Auger recombination processes (Section 2.2.2).

Despite the clear benefits of the type II InAs/InAsSb MQW structure, relatively little research and development specifically on InAs/InAsSb MQW LEDs has been reported. InAs/InAsSb MQW (7 nm InAsSb layers (Sb = 10 %) sandwiched between 13 nm InAs layers) LEDs were reported [100] to produce maximum output power of 27.5 µW (pulsed operation, 740 mA current, 30 kHz, 0.6 % duty cycle) though this dropped to 0.6 µW under reduced drive conditions (pulsed, 150mA, 1 kHz, 50 % duty cycle). At room temperature only the 3.4 µm InAs peak was observed with no emission from InAsSb at 3.8 µm observed at low temperature. Nevertheless, these devices were stated to be suited for detection and monitoring of C – H compounds such as methane [100]. A decade later Carrington [7] reported room temperature emission of 12 µW at 3.7 µm under 100 mA quasi – CW injection current from a 10 period InAs/InAsSb MQW LED of 8.5 nm InAsSb QWs between 24.5 nm thick InAs layers. The emission at room temperature was attributed to e – hh_1 and e – hh_2 QW transitions, demonstrating a high level of hole confinement in the QWs. In these devices the inclusion of an AlGaAsSb barrier at the p – layer interface enhanced the room temperature electroluminescence intensity by a factor of 5 (the effects of barrier inclusion are discussed further in Section 3.4). In addition to the bulk LEDs mentioned, QinetiQ have also reported electroluminescence from InSb/AlInSb MQW LEDs with emittance values of 3.1 and 5.3 mW / cm^2 [101, 102].

3.3.3 Superlattice LEDs

If the layers between the quantum wells are made sufficiently thin (on the order of a few nanometres) then the MQW structure transitions into a superlattice structure (Section 2.1.5). The overlap of the electron and hole wavefunctions increases

significantly. The discrete energy levels of the electrons in the conduction band and holes in the valence bands transform into minibands. Electrons can now propagate through the structure by tunnelling, which increases the probability for radiative recombination with holes. In the InAs/InAsSb structure the holes remain strongly confined in the InAsSb QWs and do not show the same magnitude of dispersion as the electrons although they do interact with each other if the InAs barriers are thin enough. The advantage of the superlattice structure is the significantly higher overlap of the electron and hole wavefunctions, which is directly proportional to the expected radiative recombination rate of the free carriers (electrons and holes). Furthermore, the beneficial suppression of Auger non – radiative recombination processes exhibited by the type II structure [103] becomes more pronounced in the superlattice [104]. Thus, comparing similar MQW and superlattice structures, the overall emission intensity is expected to be much higher from the superlattice [2].

Early work on InAs – based superlattice LEDs includes that of Tang [105] reporting the first uncooled (room temperature emission) InAs/InAsSb superlattice (Sb = 9.5 – 27.4 %) LEDs. These devices produced peak emission of ≈ 200 nW intensity at 5 µm at 300 K and demonstrated the suitability for CO_2 gas sensing with the CO2 absorption at 4.2 µm observed in the room temperature emission spectra (Figure 3.4a). This was soon furthered by those of the same ICL research group reporting InAs/InAsSb strained – layer superlattice LEDs containing Sb ≈ 8% in the QWs emitting at 4.2 µm at room temperature (Figure 3.4b) with output powers above 0.1 mW [2, 3]. More recently, InAs/GaSb superlattice LEDs fabricated into arrays have been employed in the development of infrared imaging [106, 107, 108, 11] (discussed in Section 3.5.2).

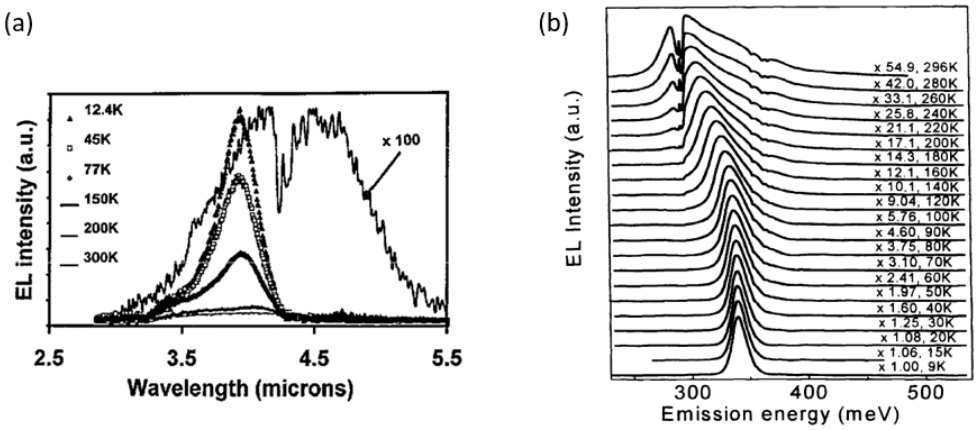

Figure 3.4 – a) Temperature dependent EL spectra for InAs/InAsSb (x=0.095) superlattice LED reported by Tang [105] showing room temperature emission peaking at ≈ 5 µm with the CO_2 absorption feature at 4.2 µm observed. b) Room temperature EL from InAs/InAsSb (x=0.082) SLS LEDs [2] showing CO_2 absorption near the emission peak at room temperature, demonstrating suitability for gas sensing.

3.4 Inclusion of electron - blocking barriers

The inclusion of a wide band gap electron-blocking barrier either side of the active region to prevent free carriers escaping and recombining at the surface or at the interface with the substrate [109] has been shown to increase room temperature electroluminescence intensity by a factor of 5 [7] by preventing carriers from escaping the active region. Similarly, as shown in Figure 3.5, improvements of approximately 3.5 times to the internal efficiency of InAs/InAsSb superlattice LEDs has been demonstrated [2, 3]. Electroluminescence was enhanced by the inclusion of an AlSb barrier [3]. Devices with an InAs/InAsSb single quantum well active region incorporating $AlAs_{0.02}Sb_{0.98}$ or $In_{0.83}Al_{0.17}As$ electron confining barriers either side were also reported [110] to produce output powers of 108 µW and 84 µW at λ = 4.1 and 4.3 µm respectively, with improved quantum efficiencies of x 7 and x 3.4 compared to control LEDs without barriers. Additionally, improved performance was reported from an InAs/InAsSb LED by a factor of x 6.3 with the inclusion of an InAlAs barrier [111]. It is therefore clear the importance of not just maximising the potential

rate of free carrier radiative recombination, but also to minimise carrier escape and non – radiative recombination, to achieve improvements to device output power.

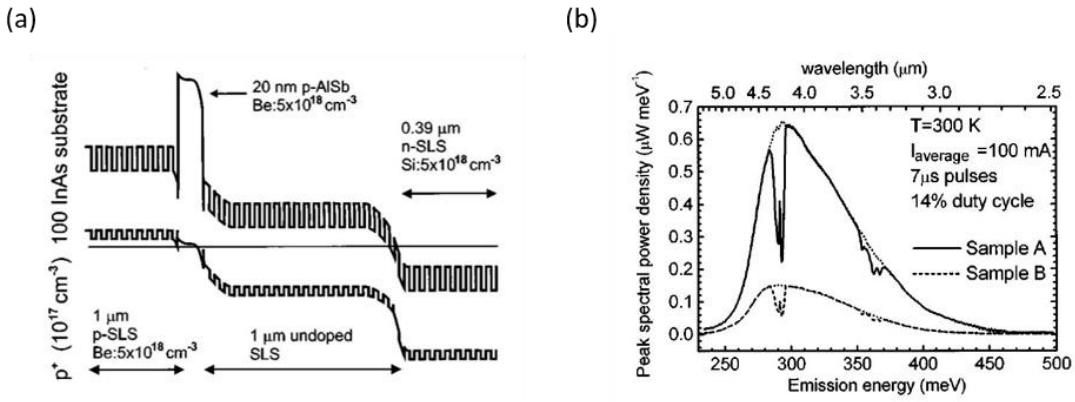

Figure 3.5 – (a) Schematic of LED band structure, (b) Room temperature electroluminescence spectra, showing enhanced emission intensity from the LED (Sample A) with the AlSb barrier included [3].

3.5 Alternative approaches

Alongside the continued development of LEDs with bulk or multiple quantum well structures as the active region, alternative methods have emerged to improve their performance. The developments relating to three of the main concepts – cascade structures, arrays, and plasmonic enhancement – are briefly discussed below.

3.5.1 Cascade structures

The inter – band and inter – sub – band cascade structure, in which a single electron can be recycled to undergo multiple radiative recombination processes, has been established as an efficient way to boost the output of mid – infrared LEDs which is otherwise compromised by the reduced energy possessed by mid – infrared photons. Details of the cascade structure are discussed in Section 2.5.4. Electroluminescence from type II inter – band cascade LEDs has been reported covering the mid to far

infrared (5 – 15 µm) range [112, 54, 108, 113, 114] with emission of milliwatt powers up to room temperature [115, 116].

3.5.2 LED Arrays

The optimisation of a single LED can only be progressed so far. High power emitters can be created by linking together multiple LEDs into an array of LEDs which operate together. QinetiQ developed the first mid – infrared LED arrays comprised of connected InSb/InAlSb heterostructure LEDs [117] which were subsequently commercialised for CO2 detection by GSS Ltd [118]. In addition, QinetiQ have developed InSb/$Al_xIn_{1-x}Sb$ MQW LED arrays [119] for the realisation of surface acoustic wave (SAW) single photon sources for long distance free – space communications. An example device consists of 16 elements connected to give a total emitting area of 1 mm^2 and were measured to have maximum internal quantum efficiency of 85 % at 15 K [102]. Furthermore, AlInSb bulk mid – infrared LEDs connected in an array were recently demonstrated to exhibit a 75 % higher power conversion efficiency compared to commercial devices and proposed to be easily integrated into portable gas sensing devices [120].

Infrared imaging systems which are an important tool in military, industrial and medical applications [121, 11] due to the unique infrared radiation emitted by hot objects. The development and calibration of these systems is made possible by infrared scene projectors [11, 121, 108]. Whilst having been available since the 1980s most of these devices use black – body emitters to create the images and are therefore limited in the frame rate and operating temperature range [121, 11].

Infrared LEDs are an appealing alternative light source due to their narrow emission spectra, high output power, fast switching time, lower cost and reliability [108, 112]. This has led to the development of LED arrays that can mimic black – body emission [121, 122, 108, 112] up to and above 1400 K [113] to realise systems with a faster frame rate and which do not suffer from temperature related performance degradation from device heating due to the absence of the black body source.

3.5.3 Plasmonic enhancements

The field of plasmonics has undergone rapid expansion in recent years and continues to attract significant research interest. Mid – infrared plasmonics has been identified as particularly beneficial in the development of chemical sensing and thermal imaging applications [123]. The interest in plasmonics arose after the demonstration by Ebbesen [124] of extra – ordinary optical transmission of light through sub – wavelength sized ($d << \lambda$) holes in a patterned metal layer that contradicted standard aperture theory. This led to surface patterning being developed as an attractive method for improving the light extraction from LEDs by coupling of photons to surface plasmon modes [125, 126, 127, 123, 1] however optimising the process is challenging due to the scattered emission of the photons impinging on the surface at various angles. Recently, integration of a photonic crystal structure supporting surface plasmons has been shown to enhance five – fold the light extraction efficiency of near - IR LEDs [128] highlighting the potential benefits of plasmonics.

3.6 Summary

Mid – infrared LEDs for the application of gas sensing have received significant attention regarding the research and development of the materials and structure of an optimised active region. Tunability of the emission spectra to the absorption signatures of a variety of gases across the mid – infrared region has been demonstrated. Whilst bulk structures present a simpler design and growth procedure, tuning the emission is limited by only being able to change the composition of the material. The quantum well structure enables straightforward modification of the emission wavelength through changing either individually or together the layer thicknesses and compositions of binary and ternary alloys used. Type I structures exhibit a high rate of radiative recombination through the confinement of the electrons and holes together in the QWs that facilitates a high overlap of their wavefunctions. The type II structure can act to suppress non – radiative Auger recombination processes that are detrimental to device performance at high temperatures, however the disadvantage is that the spatial separation of the electrons and holes significantly reduces the rate of radiative recombination compared to the type I structure. The superlattice structure, a version of the multiple quantum well design in which the layers are sufficiently thin to allow electron tunnelling to occur, can act as a best of both types by suppressing non – radiative recombination whilst also recovering some of the otherwise lost radiative recombination rate. Since superlattices have more adjustable design parameters and present a better option for optimising the LED active region compared to a MQW structure they are the focus of the subsequent work described in this thesis.

Date	Author (primary)	LED structure	Comments	λ at 300K [μm]	Power at 300K [μW]
1966	Melngailis	Bulk InAs		3.7	
1993	Dobbelaere	Bulk InAsSb		4.3	
1999	Hardaway	InAs/InAsSb SQW		5, 8	50, 24 (1.5A inj.)
1999	Hardaway	InAs/InAsSb SLS		4.2	140
1999	Pullin	InAs/InAsSb SQW	AlSb barrier included	4.2	100 (2A inj.)
2000	Pullin	$InAs/InAs_{0.91}Sb_{0.09}$ SQW	$In_{0.83}Al_{0.17}As$ barrier	4.1	108 (1.5A inj.)
2000	Pullin	$InAs/InAs_{0.86}Sb_{0.14}$ SQW	$AlAs_{0.02}Sb_{0.98}$ barrier	4.7	7.6, 84 (1.5A inj.)
2009	Carrington	$InAs/InAs_{0.92}Sb_{0.08}$ MQW	$Al_{0.90}Ga_{0.10}As_{0.15}Sb_{0.85}$ barrier	3.7	12 (100mA inj.)
2018	*Keen*	*$InAs/InAs_{1-x}Sb_x$ (x=3.8, 6.2) SLS*		*4.2*	*8.2, 3.3 (100mA inj.)*

Table 3.1 – Summary of chosen notable literature on InAs(Sb) light – emitting diodes.

Chapter 4

Experimental procedures

Further to the theory and concepts outlined in Chapter 2, the specifics of the different equipment used during the research work are discussed in this chapter.

4.1 Molecular Beam Epitaxy (MBE)

Molecular beam epitaxy (MBE) is a highly technical procedure for the controlled creation under ultra – high vacuum conditions of high – quality structures made of semiconductor materials with very specific layer thicknesses, compositions, and doping levels. The samples for this thesis were produced using a VG – V80H MBE system in the Physics department at Lancaster University. Figure 4.1 shows a simplified schematic of an MBE machine with the important components labelled:

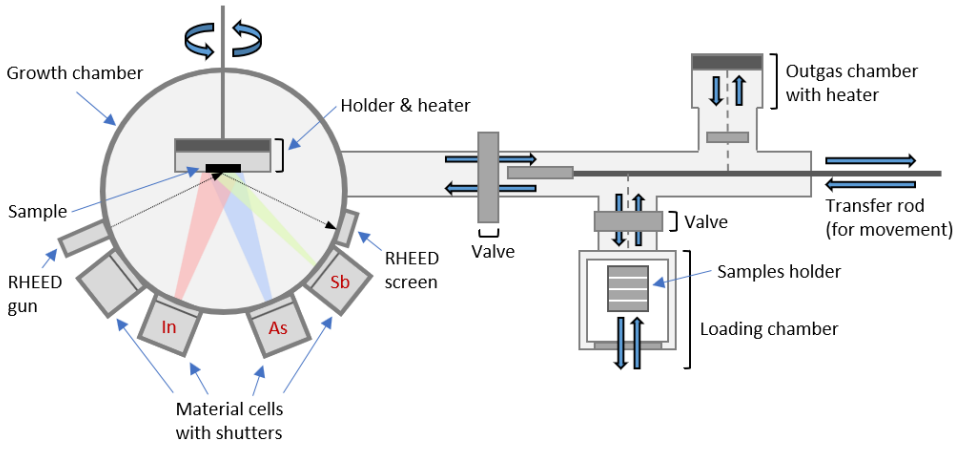

Figure 4.1 – Simplified schematic of MBE system with important components labelled - the growth chamber surrounded by material cells, and the connected smaller outgas chamber and loading chamber, between which samples are moved for undergoing different stages of the growth process.

Structures are created inside an ultra – high vacuum growth chamber maintained at a pressure of ≈ 10^{-10} mbar by a series of pumps. Surrounding the growth chamber are

cells containing solid sources of the elements to be used. Heating of these cells causes atoms of the elements in gaseous state to diffuse onto and incorporate into the top layer of the material being grown. For growth of the InAs/InAsSb structures, a thermal effusion K – cell provided indium (In) flux, and valved cracker cells provided the arsenic (As) and antimony (Sb) fluxes. Doping of layers for the LED devices was achieved with silicon (Si) and tellurium (Te) at concentrations of $10^{17\text{-}18}$ cm^{-3}. Additional cells containing elements such as gallium (Ga) and aluminium (Al) are available for use but were not required for the structures grown for this work. Shutters present on the ends of the cells can be switched between open or closed in a fraction of a second, allowing for quick changes in the materials being deposited on the sample surface. Gate valves act to maintain high vacuum conditions as necessary, for example by isolating the UHV growth chamber whilst samples are transferred between the loading chamber and outside of the system which is subject to fluctuations in the pressure.

III – V substrates (obtained from Wafer Technology as two – inch diameter wafers) can be grown on at this size but are usually cut into quarters for more efficient use as four smaller samples of different structures can be grown, with one quarter providing enough material for structural characterisation or device fabrication. The substrate pieces are mounted securely on molybdenum holders and loaded into the system, where they then individually prepared by undergoing an out – gassing stage of being subjected to high temperature to remove contamination, before being placed inside the growth chamber. Movement of samples around inside the MBE machine between the different compartments is by manual movement of levers and

shutters. Prior to growth of the desired structure, a de – oxidisation process is carried out to ensure the surface of the substrate is in good condition to aid the grown of high – quality defect – free material on top. This involves heating the substrate to remove contaminants. During growth, the substrate is rotated slowly to improve surface layer uniformity.

During the growth, surface constructions are monitored by in – situ reflection high energy electron diffraction (RHEED) which is a technique for studying the surface structure of solids grown under UHV conditions inside the MBE growth chamber. This approach is based on the diffraction of high energy electrons from an ordered crystal and thus the ability to determine the surface structure by deviations from this reference. The setup of the RHEED system is an electron gun (operated at a current of 1.5 – 2.25 A and a voltage of 12 – 14 kV) which produces an electron beam directed onto the top of the material at a very shallow angle (< 2°). These electrons are reflected from the surface and then strike a phosphor screen, forming a visible diffraction pattern which indicates the structure of the surface. Thus, the RHEED pattern observed corresponds to a specific surface crystallography. The patterns consist of lines: main lines which correspond to the spacing between the atoms of the surface layer, and weaker lines in between these which give further information about the surface structure. The appearance of the RHEED pattern also indicates the condition of the surface – a rough surface presents a weak ‘spotty’ pattern whereas a smooth surface is indicated by observing a bright ‘streaky’ pattern [30, 33]. If the surface is contaminated by the presence of an oxide, then the amorphous material means no diffraction pattern is observed. As a layer is grown, in addition to the

pattern changing, the intensity of the observed pattern also varies. Initially, the build – up of patches of material roughens the surface and thus the RHEED pattern reduces in intensity. Further deposition of material such that amalgamation forms a single layer of material smooths the surface, such that the RHEED pattern increases intensity again [30]. An example 2 x 4 RHEED pattern observed at the stage when the substrate is ready after deoxidation for structure growth is shown in Figure 4.2 [61].

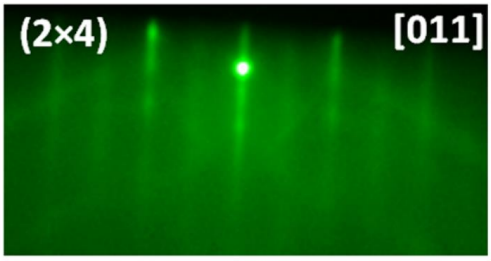

Figure 4.2 – 2x4 RHEED pattern observed after deoxidation to prepare the substrate for layer growth.

Growth rates are calibrated by observing this RHEED spot intensity oscillation. When growth is started, the material surface is smooth and RHEED spot intensity is high. As growth proceeds, clusters of atoms and islands form, and the spot intensity dims due to scattering. Once the new layer is fully formed, spot intensity increases. The time of this oscillation corresponds to the time to grow a single monolayer of material. In practice, several oscillations are timed, and an average growth rate calculated. The layers in the structures are grown at a rate of typically around an Angstrom per second to balance structural quality with the time required to complete the growth.

4.2 X – ray Diffraction (XRD)

The wavelength of X – rays is on the order of the atomic spacing, and so the crystalline structure of the materials acts as a 2D diffraction grating. For constructive interference of the X – rays it is necessary that the path difference must be equal to an integral number of wavelengths, which leads to consideration of the Bragg condition:

$$n\lambda = 2d \sin \theta_B \tag{4.1}$$

where n is an integer, λ is the wavelength of the X – rays, d the lattice plane spacing, and θ_B the Bragg angle which is dependent on the material. Thus, materials with different lattice plane spacing (d) diffract the X – rays at different angles, enabling XRD scans to determine layer thicknesses of the different materials grown by MBE. All the samples were characterised using a Bede QC-200 X – ray diffraction (XRD) to obtain ω – 2θ scans. A schematic diagram showing the setup of the XRD scanning system is shown in Figure 4.3(a) alongside Figure 4.3(b) showing a representation of the Bragg condition (Equation 4.1).

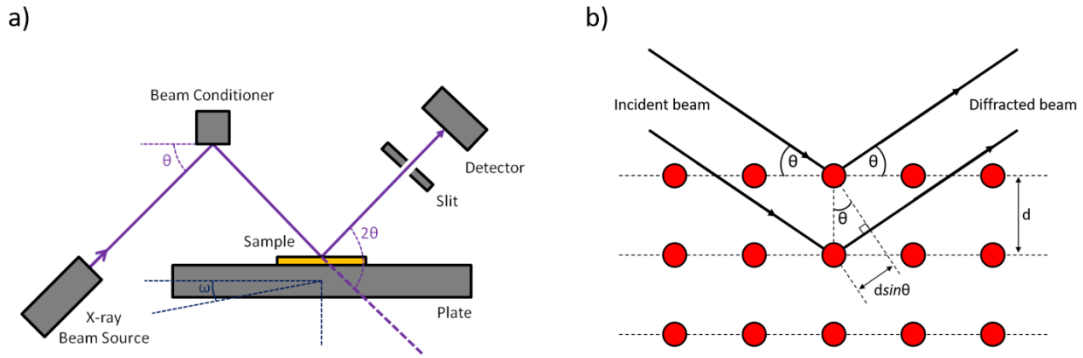

Figure 4.3 – a) schematic diagram showing the setup of the XRD scanning system used to measure X – ray diffraction from the samples; b) representation of the Bragg condition (Eqn. 4.1).

The sample is placed onto a plate that rotates at various angles of ω whilst the detector is simultaneously rotated at various angles of 2θ such that a large range of

diffraction angles can be investigated. A beam conditioner containing a high – quality crystal of known lattice constant (GaSb) is used to select the appropriate Bragg angle prior to running the scans. As the angle of incidence on the surface changes, a perfect sample will produce a sharp peak that is observed when the angle is such that the crystallographic direction is parallel to the diffraction vector, satisfying Bragg's law for constructive interference. The system records these peaks over the range of incident angles measured. Measurements were taken over the ± 5000 arcsec range in steps of 10 which was sufficient to identify multiple fringes. The experimental data is then input into accompanying Bede Mercury RADS simulation software that works based on dynamical scattering theory of X – ray diffraction to produce a theoretical XRD result based on the structural parameters set. By matching the theoretical and experimental XRD results, the structural properties of the sample such as layer thicknesses and material compositions can be determined.

4.3 Photoluminescence spectroscopy

Photoluminescence of the samples was excited using a 785 nm visible red laser focused onto the surface of the sample which was held inside an Oxford Instruments continuous – flow gas exchange cryostat capable of maintaining the sample at a chosen temperature in the range 4 – 300 K. The PL emission was analysed using a Bruker Vertex 70 Fourier transform infrared (FTIR) spectrometer run in step – scan mode. The radiation was detected using a nitrogen cooled 77 K InSb photodetector and lock – in amplifier connected to the FTIR system. A schematic diagram showing the setup of the FTIR PL system is shown in Figure 4.5. Operation of the FTIR system was controlled by OPUS software running on the connected computer.

Measurements of the PL were set to be recorded over the range of 5000 – 1667 cm^{-1} (2 – 6 μm) to span the emission wavelengths of the samples. The resolution was set to the 8 cm^{-1} option, corresponding to a resolution of ≈ ± 7 nm of the data points. These settings can be changed, but these were found to achieve a good balance between scan accuracy and scan time.

The preparation of the system for low temperature measurements is as follows. Firstly, the inner chamber is opened and purged of air by allowing helium to flow in for ~ 1 minute which expels the air. Once this is done, the sample holder arm (with the sample or LED attached) is quickly and carefully fixed into position and the chamber is sealed from the outside atmosphere. Now, a small amount of helium is passed into the inner chamber, and then the chamber is pumped, which reduces the pressure inside. This process is repeated two or three times, until pressure of ~ 10^{-6} mbar is achieved. At this point a final flow of helium is permitted into the inner chamber, but it is then not pumped out but sealed. Once the low pressure inside the inner chamber has been established, the outer chamber is opened and continuously pumped (no helium is necessary) until the pressure reduces to ~ 10^{-6} mbar. At this stage, the system is ready to permit being cooled. Liquid helium flows from a dewar through a transfer arm into the space between the chambers, which cools the sample and gas inside the inner chamber. The outer chamber acts as insulation from the outside environment, allowing this cooling to be achieved and the sample to remain at a stable temperature during measurements.

A laser diode emits a laser beam of 785 nm wavelength with a spot size of approximately 1 mm diameter towards the cryostat containing the sample. The laser is operated at 1 kHz with a 50 % duty cycle corresponding to a current of 100 mA, which is defined as full power. This corresponds to an excitation power of approximately 2.5 W / cm^2 at the surface of the sample. Filter wheels containing different neutral density filters (obtained from Thorlabs) can be positioned in the beam path before it reaches the cryostat to allow measurements with a fraction of the laser power down to ~ 1 %. The sample is fixed onto a sample holder arm and positioned inside the cryostat at an angle of 45 degrees to the line of the laser beam. The laser beam enters the cryostat and onto the sample of the surface, with the laser beam and the infrared photoluminescence from the sample then both exiting the cryostat through a different window. A lens is positioned in the path between the cryostat and the FTIR system, which along with the laser diode can both be adjusted in x, y, z directions to maximise emission received into the FTIR system.

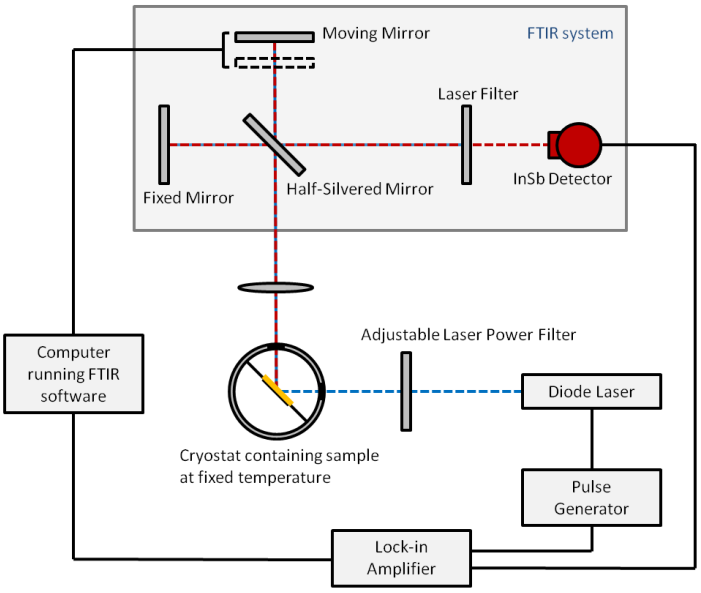

Figure 4.4 – Schematic diagram showing the setup of the FTIR PL system used to measure photoluminescence from the samples. Actual position and size of the elements is different. Beam paths of the laser (blue dashed line) and infrared photoluminescence from the sample (red dashed line) are shown.

The FTIR system works like a Michelson Interferometer, using a half – silvered mirror to split the beam, and the optical path length difference is determined by one mirror being fixed and one mirror moving. An interferogram is obtained by operating the system in step scan mode where by movement of the moveable mirror this optical path difference is varied and the signal for different values is recorded. The split beam recombines and then passes through a filter which absorbs all the laser light such that only the photoluminescence from the sample goes on to reach the InSb detector. The InSb detector is cooled with liquid nitrogen to maintain its internal temperature at around 77 K at which signal detection is most efficient. Signal which is detected is sent via a lock-in amplifier to the computer. OPUS software running on the computer uses Fourier transform analysis to convert the interferogram and signal from the detector into a spectrum of intensity over wavenumber corresponding to the photoluminescence emitted by the sample. The data is then saved and output, with analysis conducted using Origin Lab software on a separate nearby computer.

4.4 Electroluminescence spectroscopy

Electroluminescence from the LED devices was measured using the same FTIR system as used for photoluminescence measurements. A schematic diagram showing the setup for measuring EL is shown in Figure 4.5. The setup is almost identical to that for PL measurements, except electrical current is applied directly to the LED rather than the laser beam being incident upon the surface of the sample. The LEDs are operated with an injection current of up to 100 mA under pulsed drive conditions (1 kHz, 50 % duty cycle). The current is not increased above 100 mA to avoid risking damage to

the devices; the current can be lowered to a minimum of 20 mA to investigate the power dependence of the emission.

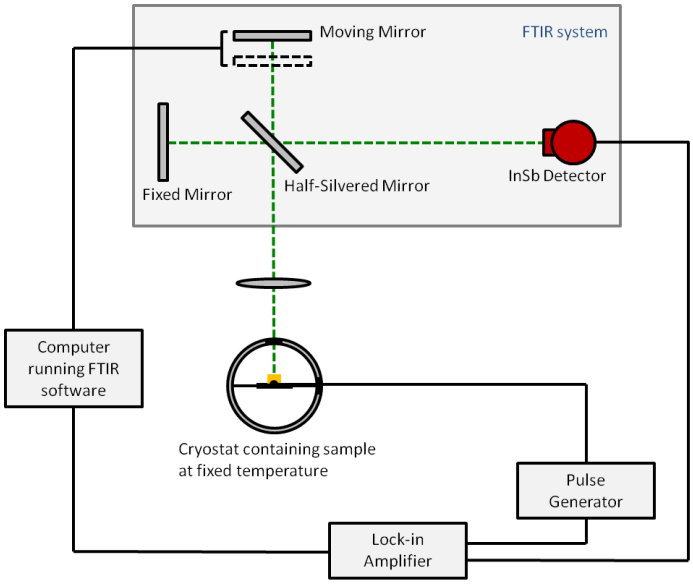

Figure 4.5 – Schematic diagram showing the setup of the FTIR system used to measure electroluminescence from LED devices.

4.5 LED characteristics

Current – voltage (I – V) measurements of the LEDs were obtained using a Keithley 2400-LV SourceMeter apparatus run through a Labview program operated from a connected computer. This software controlled the passing of a current through the LED in small increasing steps and the corresponding voltage recorded, producing a characteristic I – V graph of current versus voltage. The current was set to an upper limit of 200 mA to prevent damaging the LEDs, and the voltage was recorded over the ± 0.5 V range, in steps of 0.01 V (100 data points). Output power of the LEDs was determined by comparing the electroluminescence intensity with that measured from commercial (Roithner) bulk InAsSb LEDs emitting at similar wavelengths under the same operating conditions.

4.6 LED fabrication

Following the MBE growth of an n – n_0 – p structured sample, this is then processed on – site inside the Cleanroom facility (Class 1000 and Class 100 rooms) at Lancaster University. A conventional procedure of photolithography and wet etching is followed in accordance with the recipe for LED fabrication established by our research group. The fabrication steps are outlined in Table 4.1.

Formation of the top contact of the LED device requires selective UV exposure (step 2.3) prior to depositing the metal (gold), which is achieved by using the Top Contact design on the photolithography mask (Figure 4.6a) which has the features as clear glass in a solid chrome background. Fabrication step 3.2 requires the top contact area of the LED device to be protected whilst acid etching of the sides is carried out. The UV exposure of the device is through the MESA design on the photolithography mask (Figure 4.6b) which is the opposite to the top contact mask in that the features are chrome and the background is clear glass, thus only damaging the surrounding material desired for subsequent removal by the etching process (steps 4.1 – 5.1).

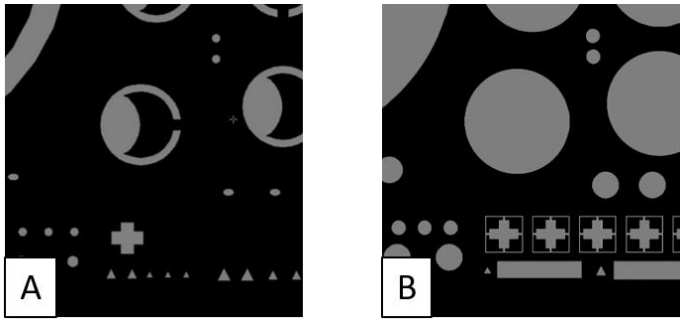

Figure 4.6 – a) Top Contact design on photolithography mask, where the features are clear glass and the background is solid chrome, used for fabricating top contact. b) MESA design on photolithography mask, where the background is clear glass and the features are solid chrome, used to protect device whilst side material is acid etched.

Photos of the processed sample ready for the final fabrication steps to produce individual LED devices are shown in Figure 4.7 (a & b0. The gold metallic contacts are observed against the dark green coloured background.

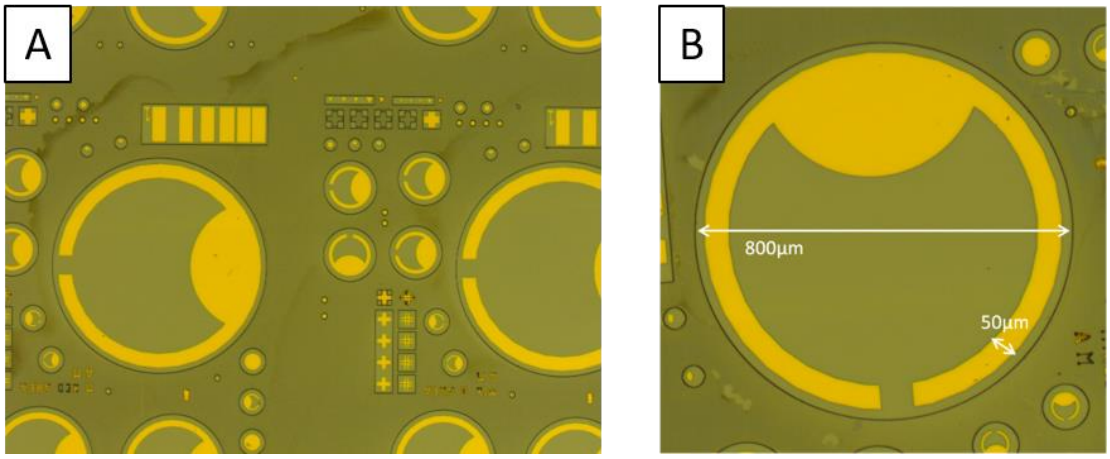

Figure 4.7 – Photos of the LED devices after fabrication process, with 800 µm diameter top contact.

The final fabrication steps are the mounting of an individual LED device onto a pin hear and the wire bonding of the device contacts to the pins (Figure 4.8).

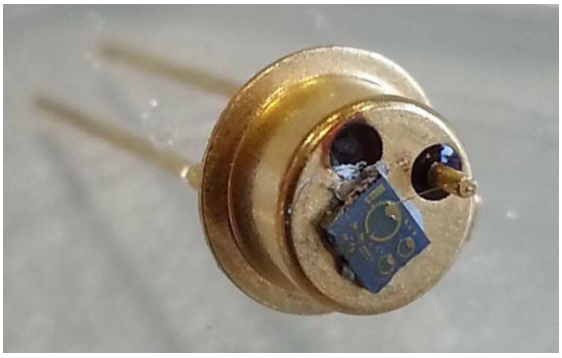

Figure 4.8 – LED device following completion of the fabrication process, which has been mounted onto a TO-header and wire bonded to the pin contact ready for undergoing testing and measurements.

The LED fabrication steps are outlined in Table 4.1.

Step	Process	Equipment	Chemicals	Method
1.1	Preparation (cleaning)	Wet bench	Acetone, IPA	Immerse sample for 5 mins in Acetone, followed by immersion for 5 mins in IPA, then blow dry with nitrogen
2.1	Top contact	Wet bench, spin coater, hot plate	Photoresist *LOR3A*	Apply *LOR3A* photoresist by spin coating (30 secs at 3000 rpm) followed by bake for 5 mins at 180°C on hot plate.
2.2	Top contact	Wet bench, spin coater, hot plate	Photoresist *S1813*	Apply *S1813* photoresist by spin coating (30 secs at 6000 rpm) followed by bake for 0 mins at 115°C on hot plate.
2.3	Top contact	Mask aligner, mixed area photo-lithography mask	-	Exposure of sample surface for 2.5 secs through 'top contact' design of photo-lithography mask.
2.4	Top contact	Wet bench	Developer	Immerse sample in Developer for 80 secs to remove damaged photoresist
2.5	Top contact	Thermal Evaporator	Gold (Au) wire, Titanium (Ti) pellets	Deposit 20nm Ti followed by 200nm Au on sample surface by thermal evaporation.
2.6	Top contact	Wet bench, hot plate	Remover *1165*	Immerse sample in Remover *1165* at 80 °C until sufficient photoresist (& gold) removed.
3.1	Preparation for etching	Wet bench, Spin coater	Photoresist *S1813*	Apply *S1813* photoresist to surface by spin coating (30 secs at 6000 rpm) then bake on hot plate (2 min at 115 °C)
3.2	Preparation for etching	Mask aligner	-	Expose surface for 2.5 secs through 'MESA' design of mixed area photolithography mask.
3.3	Preparation for etching	Wet bench	Developer	Immerse sample in Developer for 80 seconds to remove damaged

				photoresist
4.1	Etching	Acid wet bench, Surface profiler	H_3PO_4, H_2O_2, H_2O	Acids mixture at ratio 1:1:1. Etch rate ≈ 1μm/min. Monitor etched depth with profiler. Etch down to 1 μm above n-type layer.
4.2	Etching	Acid wet bench, Surface profiler	H_2SO_4, H_2O_2, H_2O	Acids mixture at ratio 1:8:80. Etch rate ≈ 600nm/min. Monitor etched depth with profiler. Etch ≈ 1 μm into n - type layer.
5.1	Post-etching	Wet bench	Remover *1165*	Immerse sample in Remover *1165* until sufficient removal of unwanted material
6.1	Back contact	Thermal evaporator	Gold (Au) wire, Titanium (Ti) pellets	Deposit 20nm Ti followed by 200nm Au on sample surface by thermal evaporation.
7.1	Cutting	Scriber		Divide wafer into individual LEDs.
7.2	Mounting	TO-46 header	Electrodag (Ag conducting paste)	Fix individual LED onto individual TO-46 header.
7.3	Wire bonding	Wire bonder	Gold (Au) wire	Connect LED contacts to header pins.

Table 4.1 – Summary of the process for LED fabrication in Cleanroom.

The LED fabrication steps outlined in Table 4.1 are shown schematically in Figure 4.9:

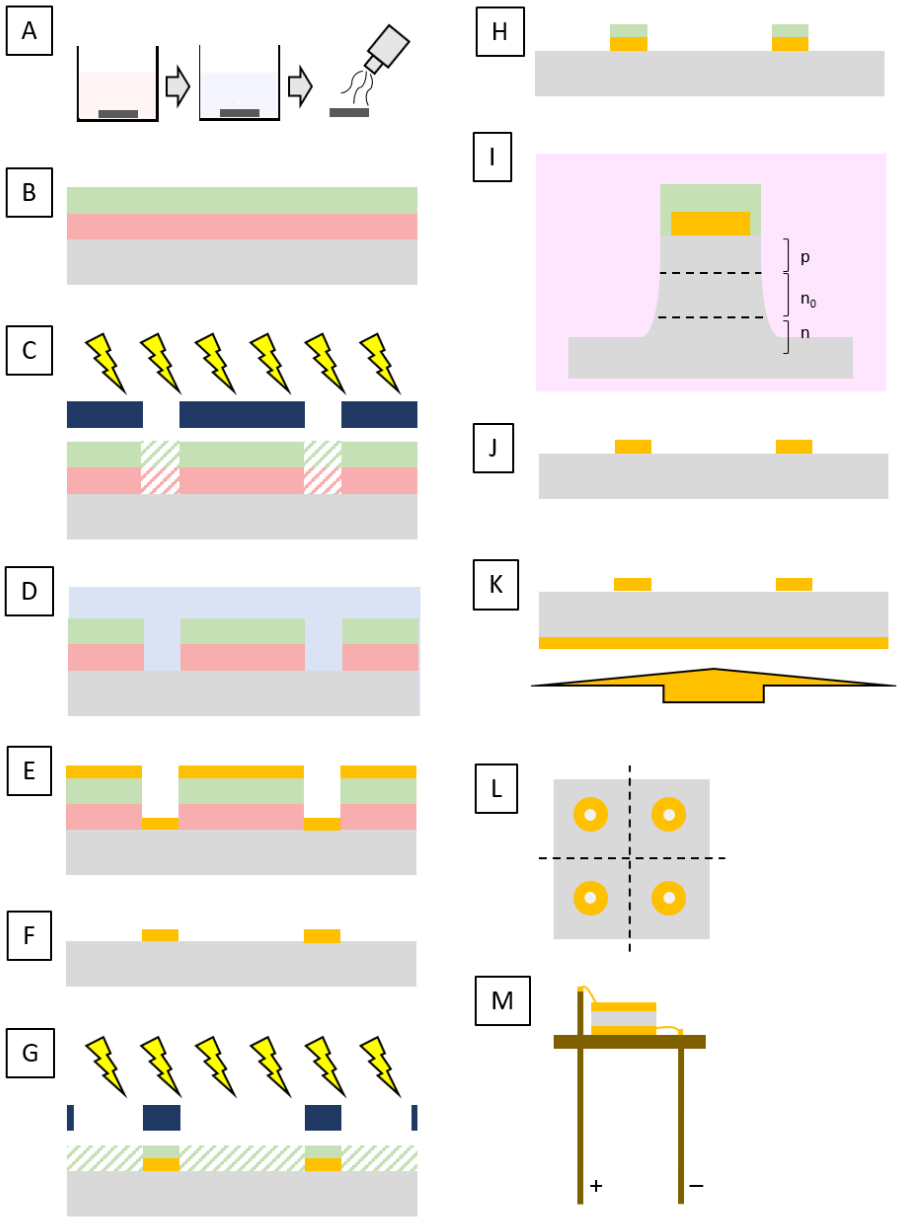

Figure 4.9 – Schematic of LED fabrication process. A) sample preparation (step 1.1), B) photoresist application (steps 2.1 & 2.2), C) UV exposure through 'top contact' design on photolithography mask (step 2.3), D) Immersion of sample in developer to remove damaged photoresist (step 2.4), E) Deposit of gold layer on surface by thermal evaporation (step 2.5), F) Sample with gold top contact after additional photoresist removal (step 2.6). G) UV exposure of surface through 'MESA' design of photolithography mask, H) Protection of top contact ready for etching (step 3.3), I) etching of material either side of the device (steps 4.1 & 4.2), J) Sample post-etching (step 5.1), K) Deposit of gold on back side by thermal evaporation to form bottom contact (step 6.1), L) Scribing sample to divide up individual LED devices (step 7.1), M) Mounting of sample on pin header (step 7.2) and wire bonding to contact device contacts to pins (step 7.3).

4.7 Nextnano modelling

Nextnano [129] is simulation software developed for the modelling and understanding of a range of electronic and optical properties of semiconductor nanostructures [129]. The program provides a self – consistent solution of the Schrodinger, Poisson and current equations. To find the quantization energies, the carriers are treated within the effective mass approximation and the dependence of band offsets relies on a materials database populated mostly from the work of Vurgaftman [130] on the band parameters of III – V materials. In the modelling, square quantum wells with immediate composition changes between the layers is assumed, and periodic boundary conditions permit a single period to be simulated to represent an infinite repeating structure. Strain in the structure is included within the program according to the work of Krijn [26] which is discussed in more detail in Section 2.1.4. The conduction and valence band energies of the InAsSb material (and similarly any other ternary alloy) is determined by interpolation between the respective values for InAs and InSb (the binary alloys), in accordance with Vegard's Law (Eqn. 4.2) where x is the Sb content of the InAsSb material and C is a bowing parameter which if non – zero means the interpolation is non – linear.

$$E_{(InAsSb)} = (1-x)E_{InAs} + (x)E_{InSb} - C(x)(1-x) \qquad (4.2)$$

The program revolves around a coding script which can be modified by the user to relate to the structure to be modelled. The overall program flow is organised as follows [129]:

1. Calculation of strain in the layers, since most semiconductor nanostructures are comprised of strained materials.
2. Calculation of the piezoelectric charges (electric charges accumulating within the materials) and the pyroelectric charges (the ability of the materials to generate an electric potential due to temperature variation).
3. Calculation of the electronic structure using a single – band or 8 $k \cdot p$ envelope function approximation, to determine the band structure and the energies of the electron and hole states.
4. Solving of Poisson, current, and Schrodinger equations self-consistently with respect to each other. With this, the determination of the electron and hole wavefunction intensities and probabilities within the structure.

Details of the Nextnano code written to model InAs/InAsSb heterostructures can be found in Appendix B. The inputs of layer thicknesses and material compositions, as well as the temperature, can be changed and their effects on the outputs of the band structure, energy levels and wavefunctions are observed. Thus, as well as being a design tool, the software provides a useful insight and convenient way of validating the experimental results. The parameter changes necessary to model the structures are discussed in the Results chapter.

Chapter 5

Results and discussion

Type II InAs/InAsSb structures offer the ability to tailor the band structure to specify the emission wavelength of photons generated by the radiative recombination of electrons and holes in the QWs, along with acting to suppress detrimental non – radiative Auger recombination processes, with strained layers enhancing this effect. This chapter discusses InAs/InAsSb strained – layer superlattice (SLS) samples and their comparison to InAs/InAsSb multiple quantum well (MQW) structures. The growth and structural characterisation of samples is discussed. Photoluminescence (PL) measured over the 4 – 300 K temperature range is interpreted, including a discussion regarding the observation of excitons under low excitation power. In addition, the 7 – 300 K electroluminescence (EL) from InAs/InAsSb SLS light – emitting diodes is analysed and compared to the photoluminescence spectra.

5.1 InAs/InAsSb structures

5.1.1 Growth of InAs/InAsSb SLS structures

A series of four InAs/InAsSb strained – layer superlattice (SLS) structures were grown on (100) n – type InAs substrates (500 µm thick, n = $2x10^{18}$ cm^{-3}) by molecular beam epitaxy (MBE) process in a VG – V80 MBE system operated at Lancaster University (as described in Section 4.1). The use of InAs as the substrate material facilitates the growth of strained layers (work regarding strain – balanced structures involves samples grown on GaSb substrate). Prior to growth the sample is prepared by undergoing a deoxidisation process to remove contaminants from the surface;

following the method previously used for samples grown on InAs substrates [61] for the samples studied in this work to desorb the oxide the InAs substrate was gradually heated up to 520 °C under As flux (to preserve the InAs material) until the RHEED pattern was observed to change from the weak x3 pattern into a brighter x2 pattern. Once the substrate has been sufficiently prepared, the temperature was reduced to 480 °C to grow an InAs buffer layer of thickness 625 nm, and then further reduced to 450 °C for growth of the InAs/InAsSb SLS structure. The InAs/InAsSb SLS structure consists of 50 periods of a 14 nm InAs layer and a 14 nm InAsSb layer, where the antimony content of the InAsSb layers varied from 3.8 % to 13.5 % across the series of samples, which was achieved by changing the temperature of the Sb cell between 550 °C and 580 °C. The layers were grown at the rate of ≈ 1 µm / hr. To obtain abrupt interfaces between the InAs and InAsSb layers, As – Sb exchange is conducted by exposing the InAs surface to Sb flux for 10 seconds prior to growth of an InAsSb layer, and before growth of an InAs layer the InAsSb surface is exposed to As flux for 20 seconds, following the optimisation method developed by Carrington [7]. On top of the SLS structure a 63 nm InAs cap is grown. Figure 5.1 is a schematic of the SLS sample structure, and the growth recipe for SLS1 is shown in Appendix A.

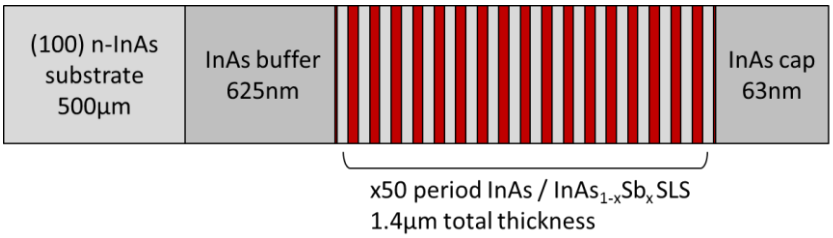

Figure 5.1 – Schematic of the sample structure, showing the multiple period InAs/InAsSb SLS structure grown on InAs substrate.

5.1.2 Structural characterisation of InAs/InAsSb SLS structures

Structural characterisation of the samples was undertaken using a Bede QC200 system to obtain high resolution X – ray diffraction (XRD) ω – 2θ scans, which were matched to simulations produced by accompanying Bede Mercury RADS simulation software, to determine the layer thicknesses and compositions. This process is described further in Section 4.2. The results are shown in Figure 5.2 and Table 5.1 summarises the structural details of the samples. The measured fringes are broader compared to the simulation, but the satellite peaks are clearly visible, which indicates growth of layers of high crystal quality and a low amount of Sb segregation into the InAs layers. Antimony content in the QWs is assumed to be uniform across the structures. For each sample both the InAs and InAsSb layer thicknesses are determined to be 14 nm, and the Sb content of the InAsSb QWs varies between the samples, in good agreement with the intended values coded into the MBE growth recipes. With increasing Sb content in the InAsSb layers the strain is known to increase, which can lead to Sb segregation out of the QWs into the surrounding layers. The average FWHM of the XRD peaks is ≈ 171 arcsec for the first sample SLS1 with the lowest antimony content in the QWs. This value progressively broadens as the antimony content of the QWs increases, to a value of ≈ 505 arcsec in the fourth sample SLS4 having QWs with the highest antimony content. Calculations using the Matthews Blakeslee model [4, 131] as shown in Figure 5.3 reveal the critical layer thickness is just exceeded for SLS4 meaning that this sample is expected to contain some dislocations that would degrade the quality of the structure. This is consistent with reduced structural quality evident in the XRD scan with the peaks less well defined compared to those of the other samples with lower Sb in the QWs.

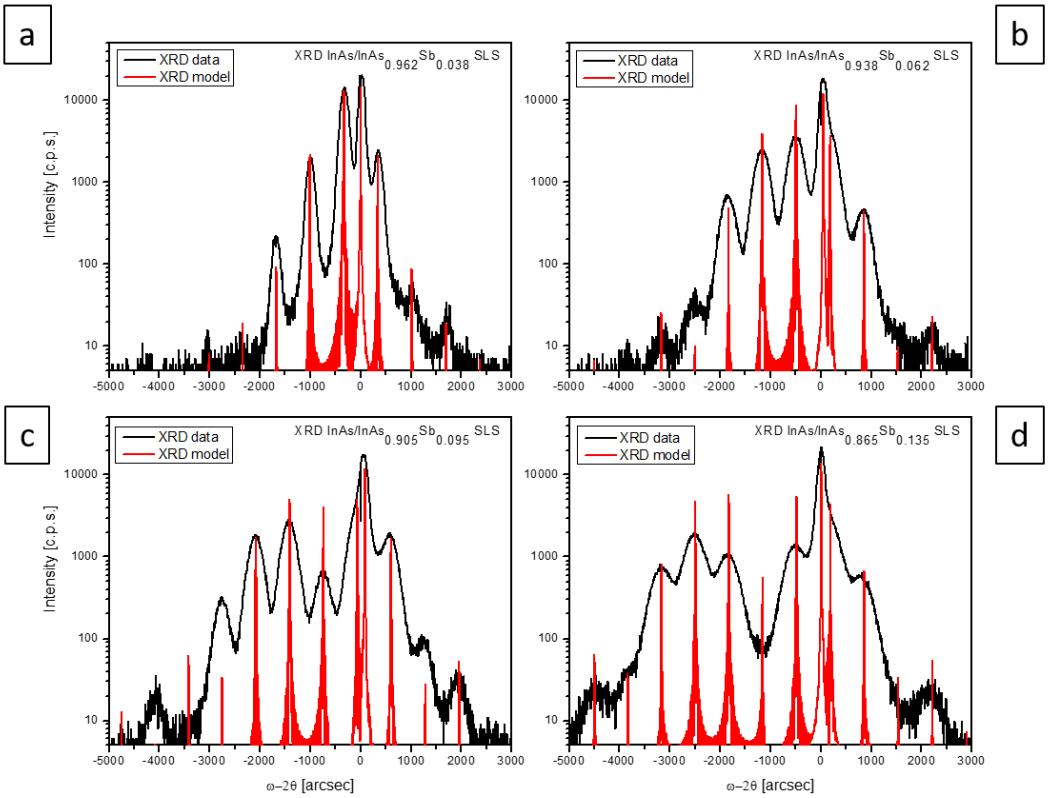

Figure 5.2 – XRD ω - 2θ scan (black line) and comparison with simulated data (red line) for the InAs/InAsSb samples; a) SLS1 (Sb = 3.8 %), b) SLS2 (Sb = 6.2 %), (c) SLS3 (Sb = 9.5 %) and d) SLS4 (Sb = 13.5%), showing progressive broadening of the peaks with increase of antimony content in the QWs.

The structural details of the SLS samples are given in Table 1.

Sample ID		InAs barrier layer [nm]	InAsSb QW layer [nm]	No. of periods	Sb content, x [%]
QMK642	SLS1	14	14	50	3.8
QMK627	SLS2	14	14	50	6.2
QMK625	SLS3	14	14	50	9.5
QMK626	SLS4	14	14	50	13.5

Table 5.1 – Summary of structural details of the InAs/InAsSb SLS samples, stating the layer thicknesses and Sb compositions determined from XRD characterisation.

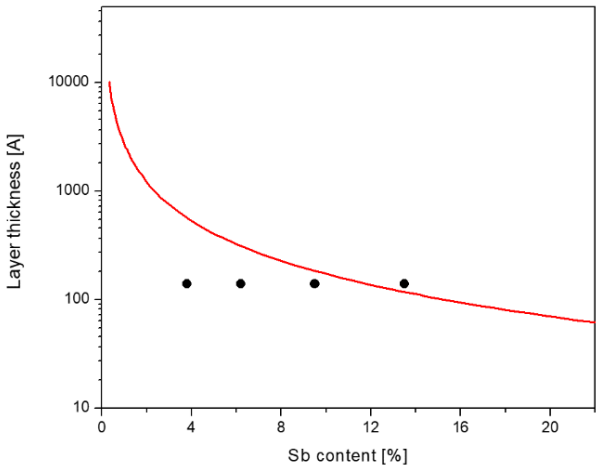

Figure 5.3 – Calculation according to Matthews Blakeslee model [4] of the critical layer thickness of the InAsSb layers in the InAs/InAsSb SLS structures, showing that it is exceeded for SLS4 sample with Sb = 13.5% in the QWs. Black points – layer thickness and Sb content of the four SLS samples determined from XRD characterisation. Red curve – Matthews Blakeslee formula for critical thickness.

Further information regarding the structures of the samples was obtained by Transmission Electron Microscopy (TEM) imaging, shown in Figure 5.4.

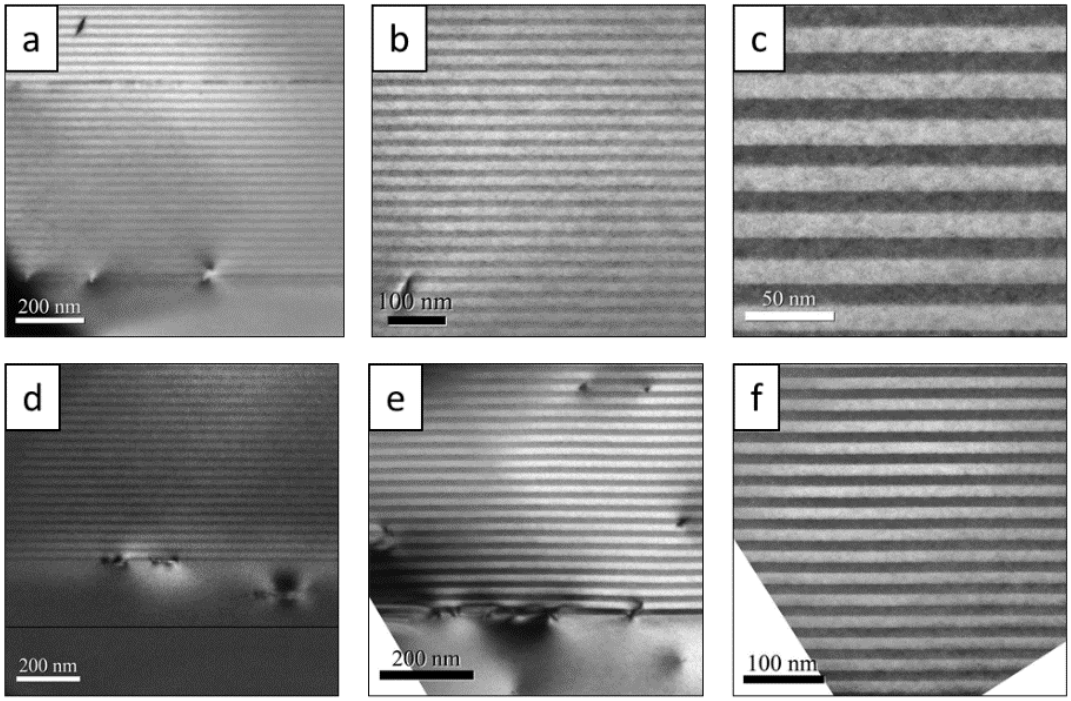

Figure 5.4 – TEM images (002 dark field) of sample SLS2 – (a) 200nm, (b) 100nm and (c) 50nm – sample SLS1 (d, 200nm) and sample SLS4 (e, 200nm and f, 100nm). The images show overall good quality structures but with some threading and misfit dislocations present. The contrast is proportional to the difference in the mean group III and group V atomic numbers, i.e. the InAs layers are bright and the InAsSb layers are dark.

The TEM images were acquired from a JEOL 2100 TEM system operating at 200 kV. The samples were prepared using standard techniques of grinding / polishing and Ar+ ion milling. The final thinning process was undertaken during cooling by liquid nitrogen and with low Ar+ ion energies (1 keV) used to minimise surface damage. In the dark field (002) images (Figure 5.4) the contrast is proportional to the difference in the mean group III and group V atomic numbers, i.e. the InAs layers are bright and the InAsSb layers are dark. A small number of threading dislocations can be seen at the interface between the InAs/InAsSb SLS region and the substrate, as well as a small number of misfit dislocations inside the SLS. However, the TEM analysis only examines 10^{-7} / cm^2 areas, indicating most of the structure will be defect free.

In addition to the TEM images, intensity profiles were conducted on SLS1 and SLS2 which are shown in Figure 5.5. The profiles of both samples are noticeably asymmetric although SLS2, which has QWs of higher antimony content, exhibits a squarer profile. The non – square shape is consistent with antimony segregation occurring during growth as described by the Muraki model [132]. Note that the bowing of the intensity profiles is an artefact of the TEM probe beam and does not have an appreciable effect on the shape of the intensity profiles or thickness measurements. The average layer thicknesses were measured for SLS1 as 12.1 nm for the InAs layers and 15.8 nm for the InAsSb layers, and for SLS2 average thicknesses of 13.2 nm and 13.7 nm, which differs slightly from the layer thicknesses derived from XRD characterisation and the 14 nm / 14 nm intended design.

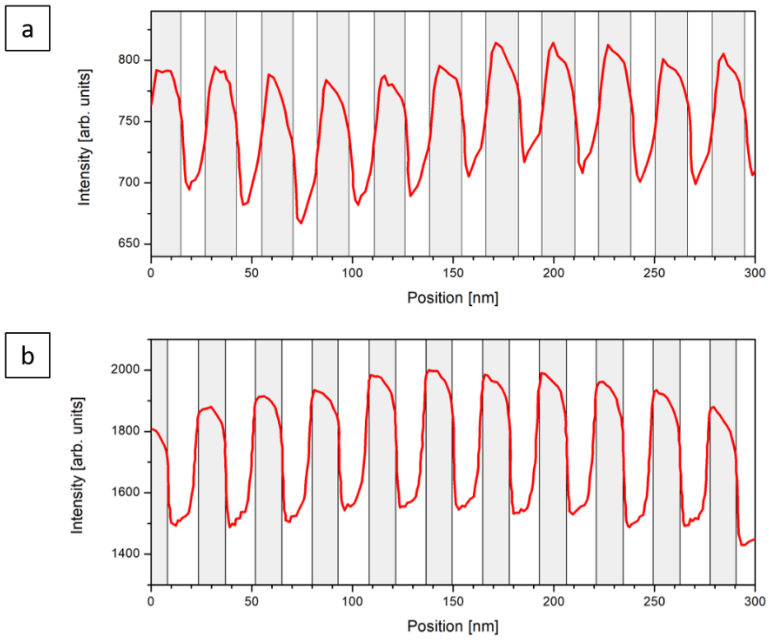

Figure 5.5 – TEM intensity profile scans showing the Sb concentration profile of (a) SLS 1 (4 % Sb) and (b) SLS 2 (6 % Sb). Measured Sb intensity (red line) and shaded regions indicating the different layers of the superlattice (white – InAs, grey – InAsSb).

5.1.3 Photoluminescence of InAs/InAsSb SLS structures

Photoluminescence of the structures was generated and measured in accordance with the setup outlined in Section 4.3. The 4 K photoluminescence spectra of the InAs/InAsSb SLS structures (Figure 5.6a) show that as the Sb content of the $InAs_{1-x}Sb_x$ QWs increases the PL emission shifts to longer wavelengths, the intensity decreases, and the peak broadens, trends which are consistent with spatially indirect transitions in type II QW [133]. As shown in the normalised spectra (Figure 5.6b) the peak intensity decreases by ≈ 13 times as Sb content of the QWs increases from 3.8 % to 13.5 % and full width half maximum (FWHM) increases from ≈ 97 nm to ≈ 270 nm.

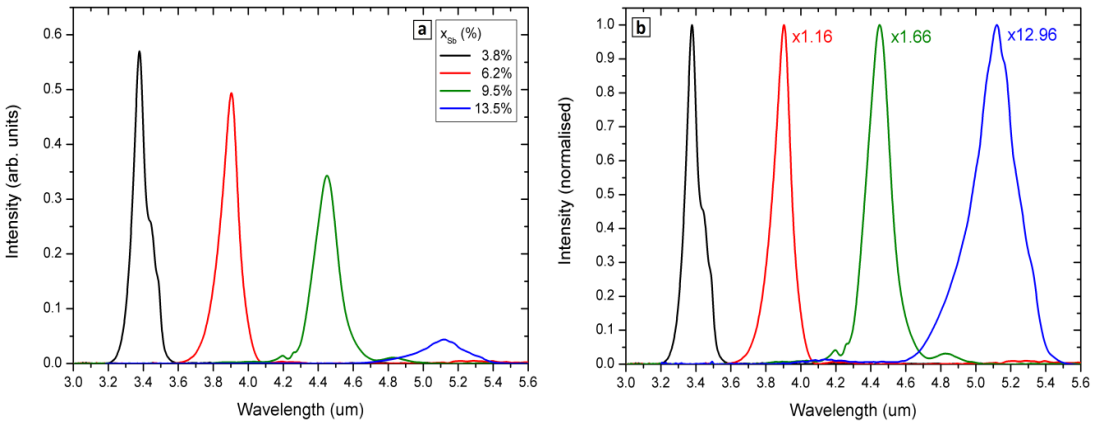

Figure 5.6 – Photoluminescence (PL) spectra of the SLS samples (a) 4K PL spectra of InAs / $InAs_{1-x}Sb_x$ SLS structures with increasing Sb content; (b) normalised 4K PL spectra of those shown in a) highlighting the decrease in intensity with increasing Sb.

The temperature dependent PL spectra from each of the InAs / $InAs_{1-x}Sb_x$ SLS are shown together in Figure 5.7. The PL peak corresponding to the $e_1 – hh_1$ ground state transition is identifiable in all cases from 4 K up to 300 K and the PL spectra do not display a peak corresponding to the InAs barrier transition, indicating that the holes remain strongly confined in the QWs as temperature is increased. The peak energy is dependent on QW composition. An additional PL peak of higher energy than the $e_1 – hh_1$ peak and a different energy for each sample, becomes visible in all the PL spectra of all the samples above ≈ 60 K. The energy separation between these peaks ranges from 15 meV to 26 meV, consistent with $e_1 – hh_2$ transitions to the next confined hole state in the QW. All samples exhibit thermal broadening of ≈ 1.1 – 1.7 k_BT.

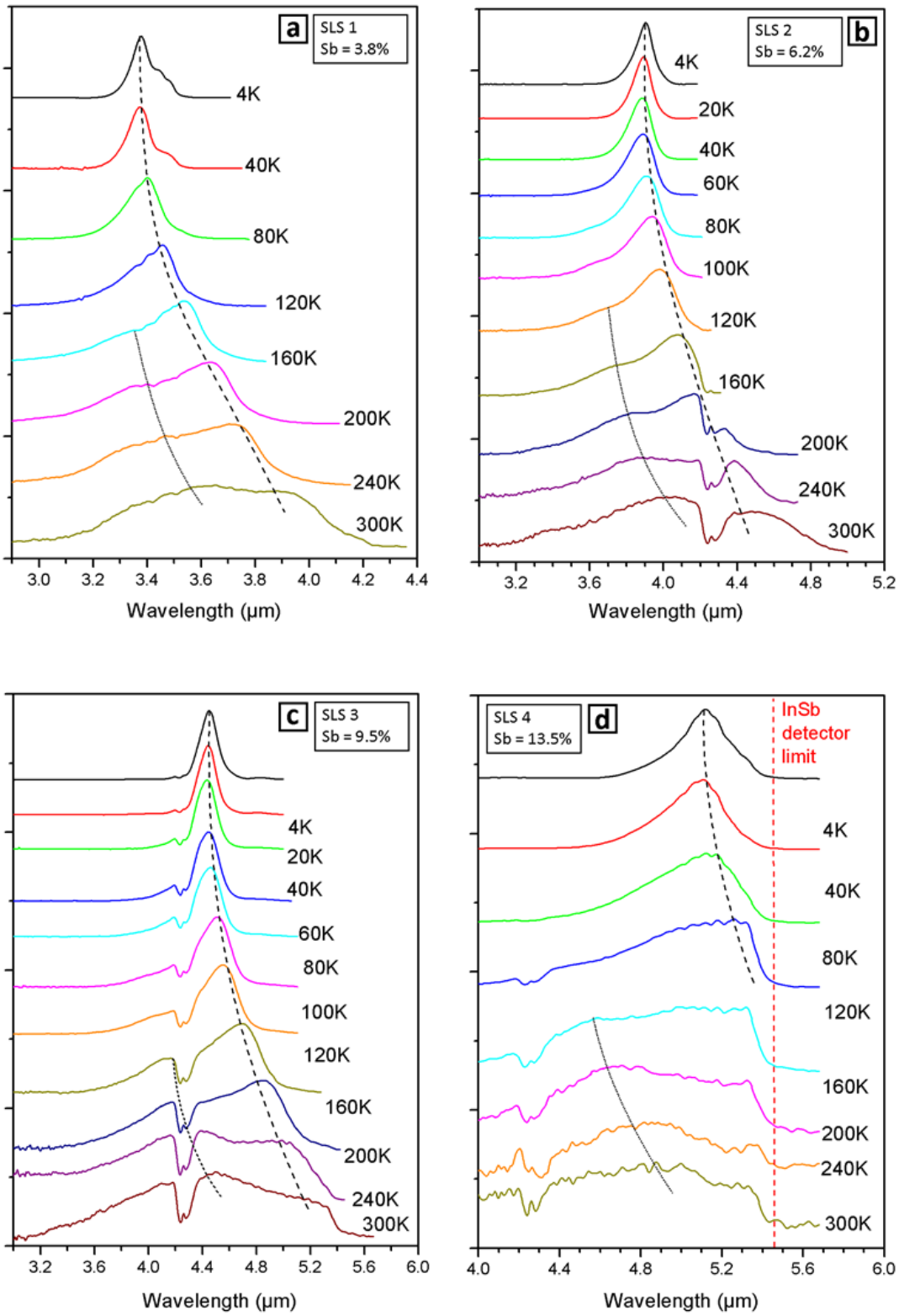

Figure 5.7 – Normalised PL spectra for all of the SLS samples at increasing temperatures. As a guide to the eye the dashed lines show the e_1-hh_1 transition, the dotted lines indicate the e_1- hh_2 transition.

With increasing temperature, the main peak in the PL spectra for each of the SLS shows the characteristic redshift of wavelength due to band gap narrowing and follows closely the well-known Varshni law [19] as shown in Figure 5.8.

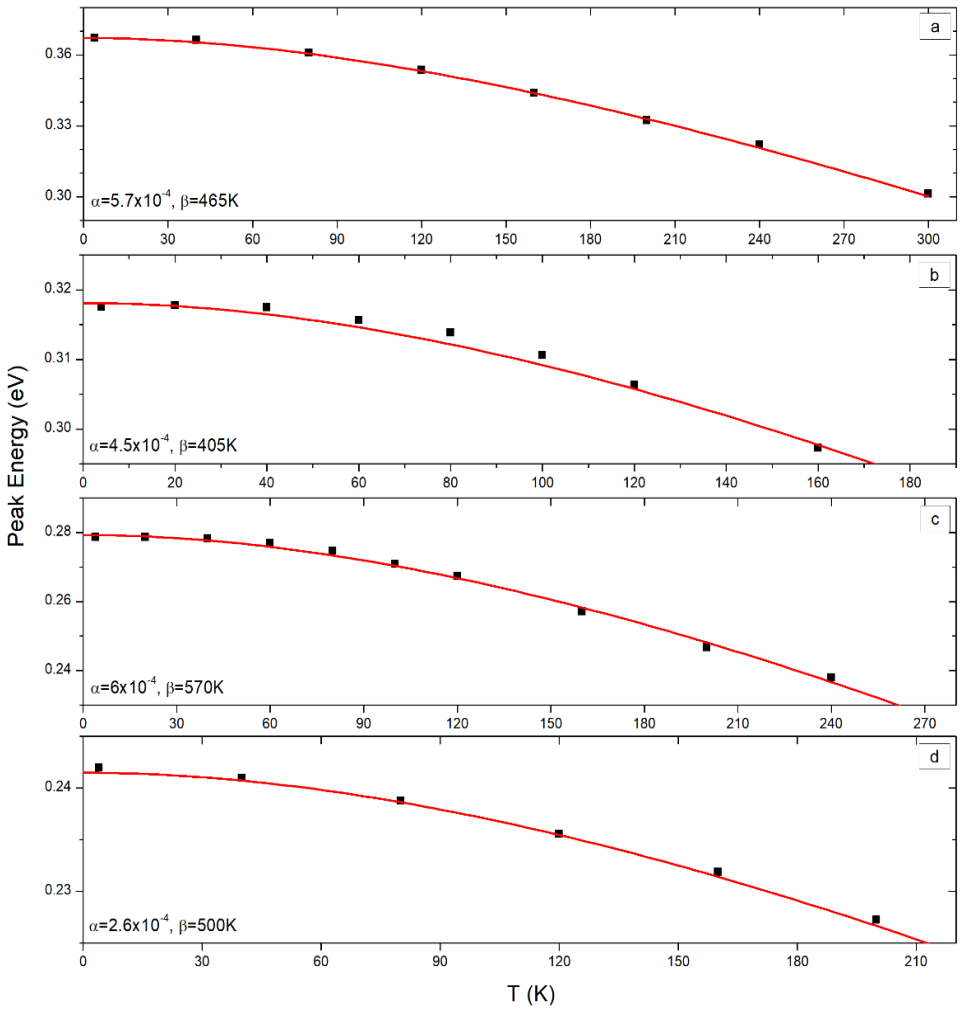

Figure 5.8 – Varshni plots showing the fitting of the Varshni law to the change of peak intensity with temperature for the four SLS samples. With increase of temperature the PL peak energy decreases, observed as the emission moving to longer wavelengths.

5.1.4 InAs/InAsSb MQW structures

To provide comparison with the SLS samples, two InAs/InAsSb MQW samples were also studied [133]. Their structure is a 10 period repeat of 40nm InAs barrier and 10nm InAsSb QW, with the antimony content of 3.7 and 4.3%. The ω – 2θ scans obtained from the XRD analysis are shown in Figure 5.9; the structural details of the SLS samples are given in Table 5.2.

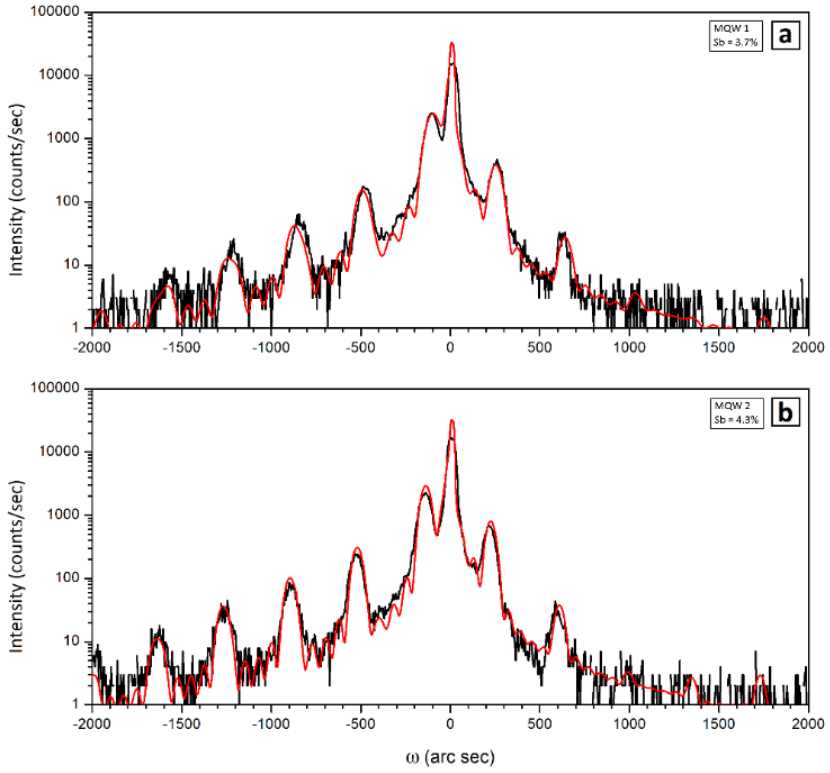

Figure 5.9 – XRD scans (ω - 2θ) comparing XRD data (black line) with simulation (red line) for the two MQW samples.

Sample ID		InAs barrier layer [nm]	InAsSb QW layer [nm]	No. of periods	Sb content, x [%]
C1467	MQW1	40	10	10	3.7
C1466	MQW2	40	10	10	4.3

Table 5.2 – Summary of structural details of the InAs/InAsSb MQW samples, stating the layer thicknesses and Sb compositions determined from XRD characterisation.

The corresponding photoluminescence spectra obtained from the MQW samples at temperatures over the range 4 – 300 K are shown in Figure 5.10.

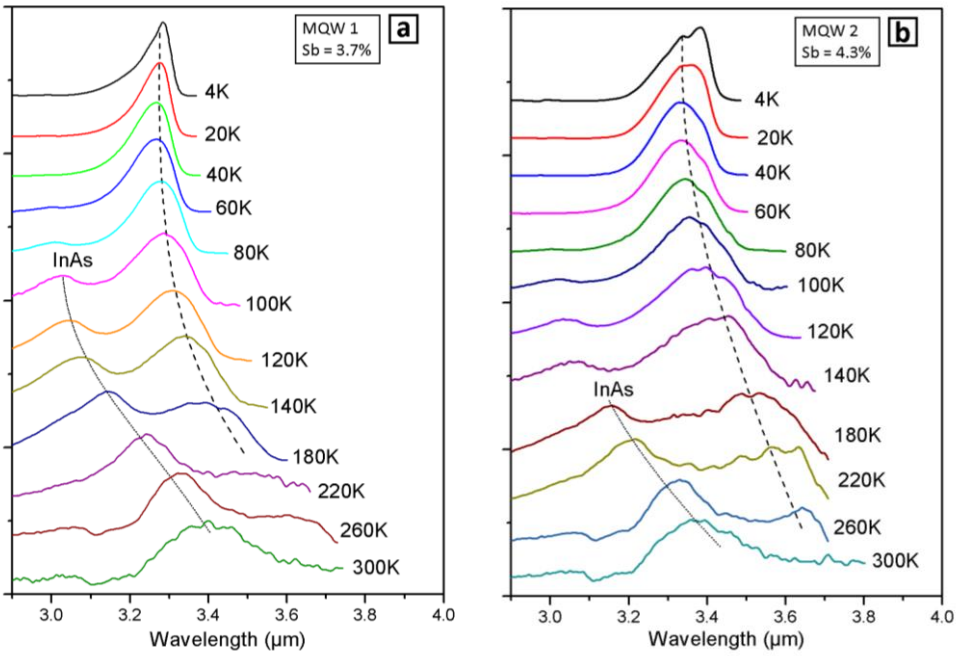

Figure 5.10 – Temperature dependence of PL obtained from the two MQW samples: (a) Sample 1 containing 3.7 % Sb in the MQW and (b) Sample 2 containing 4.3% Sb in the MQW. The lines are a guide to the eye, where the dotted line follows the e_1-hh_1 MQW peak transition and the solid line follows the peak transition from the InAs barriers.

With increasing temperature, as shown in Figure 5.11 the main peak in the PL spectra of the MQW shows the characteristic band gap narrowing / peak shift to longer wavelength, following closely the Varshni law [19]. In both samples, above ≈ 80 K additional PL emission appears, originating from thermal emission of confined holes escaping from the MQW and undergoing recombination with electrons directly across the InAs layers. This process continues up to room temperature at which point it dominates to the extent that there is no longer any observable PL emission from the MQW. This contrasts with the behaviour in the SLS samples, where the stronger hole confinement enables e – h transitions in the QWs to remain the dominant source of the photoluminescence.

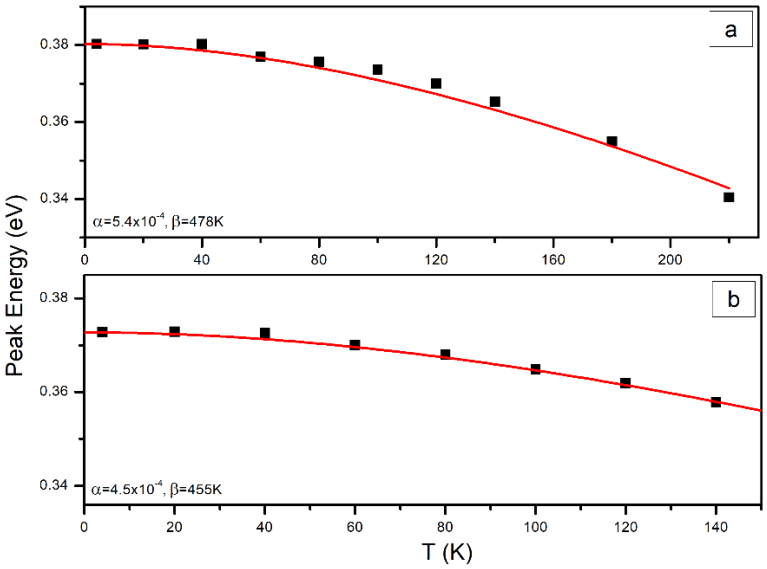

Figure 5.11 – Varshni plots showing the fitting of the Varshni law to the change of peak intensity with temperature for the two MQW samples.

5.1.5 Band structure modelling

The band structure, as well as the associated energies and wavefunctions of the electron and hole states, of the InAs/InAsSb structures have been simulated using Nextnano [129] software (see Section 4.7 for details). Since the inception of the program, more recent experimental works have shown the parameters for the InAsSb alloy presented by Vurgaftman to be inaccurate, and therefore appropriate modifications were made to the Nextnano materials database. The bowing of the spin – orbit splitting energy was set to zero (default is + 1.2 eV) in accordance with the experimental finding of negligible bowing by Cripps et al, [134]. Recalling that the conduction and valence band energies are determined by Vegard's Law (Eqn. 4.2), a non – zero value for the bowing parameter C as well as a 40:60 split between the conduction band and valence band bowings that contribute to the overall band gap were both introduced as suggested by Liu [133]. Vurgaftman reported the conduction band bowing parameter as C_{CB} = + 0.67 eV

which has since been revised upwards to + 0.87 eV by Svensson [135] and later to + 0.938 eV by Webster [20]. It was found that a higher bowing value was necessary to match to the peaks of the 4K PL spectra of our samples, which can be attributed to a higher amount of strain in the structures reducing the band gap below that of equivalent unstrained structures. The bowing parameters for the non – linear interpolation of the conduction and valence band energies were selected as C_{CB} = + 0.65 eV and C_{VB} = - 0.98 eV. Figure 5.12 shows good agreement between the simulated energy of the e_1 – hh_1 transition to the experimental energy of the primary PL peak, over the range of 0 – 15 % antimony content in the QWs.

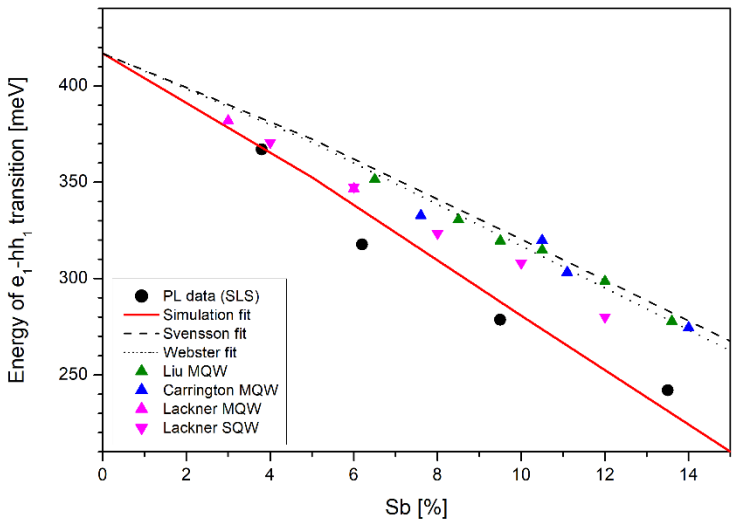

Figure 5.12 – Dependence of the 4 K PL peak energies on Sb content for the InAs/InAsSb SLS structures. The best agreement with the experimental data (black circles) was obtained with an InAsSb bowing parameter of 1.63 eV split at the ratio of 40:60 between the conduction and valence bands (red line). The dashed and dotted lines represent respectively the previously highest InAsSb bowing parameters of 0.87 and 0.938 eV reported by Svensson and Webster [29] (also split at a 40:60 ratio). PL data of InAs/InAsSb structures from additional sources (Liu [133], Carrington [7], Lackner [131]) is also overlaid on the plot.

Figure 5.13 shows for example a comparison between the MQW and SLS structures of similar Sb composition. The effect of reducing the QW separation (from 40 nm to 14 nm) is to raise the energy of the e_1 level from 1.941 eV to 1.950 eV (+ 9 meV) and

similarly the energy of the hh_1 level is increased from 1.578 eV to 1.582 eV (+ 4 meV). In each case the calculated transition energies are in good agreement with the PL transitions observed at 4 K. The activation energies for carrier escape are estimated for the MQW and SLS structures respectively to be 26.1 meV and 17.3 meV for the electrons, and 34.7 meV and 37.3 meV for hole escape from the QW.

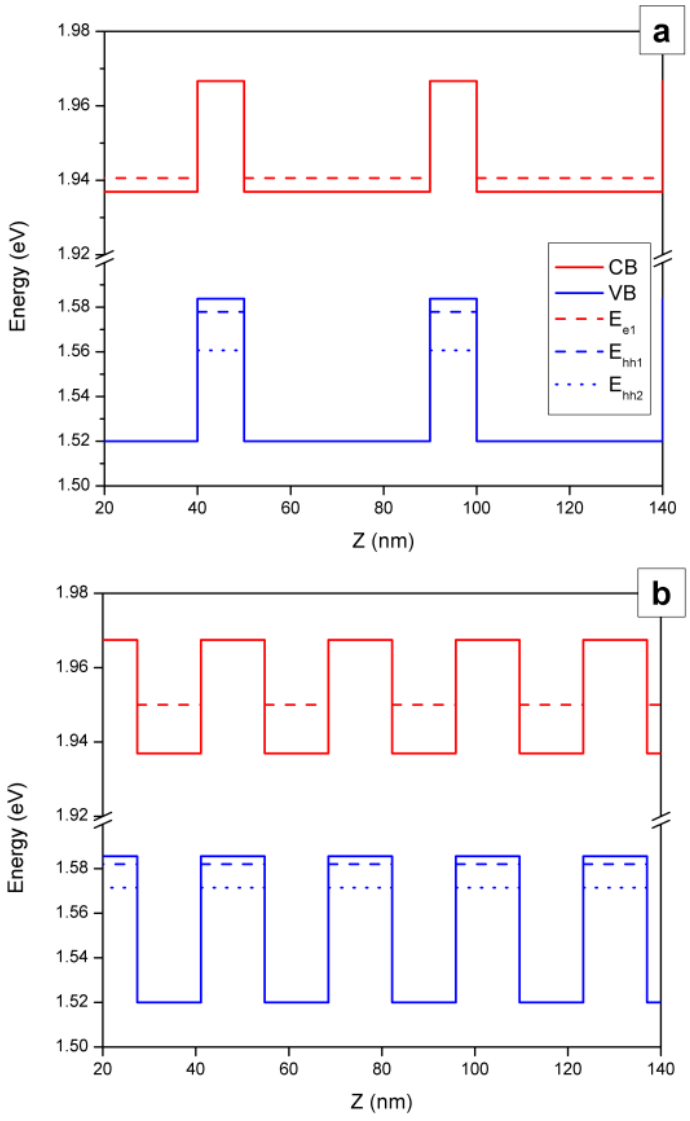

Figure 5.13 – Simulated band structure at 4K of the MQW and SLS samples with comparable Sb content (SLS1 and MQW1). Reducing the thickness of the InAs layers raises the energy level of the eigenstates which enables convenient tuning of the emission wavelength.

Considering the electron and hole wavefunctions (Figure 5.14) the heavy hole wavefunction is strongly localised within the InAsSb QW regions in both the MQW

and SL structures, however in the SLS structure with thinner layers the electron wavefunction spreads out through the structure with significant probability of residing in the QW regions. Since the overlap of the electron and hole wavefunctions is directly related to the radiative recombination rate it is expected that with shorter periods the increased wavefunction overlap results in a corresponding increase in PL emission intensity. Increased antimony content increases the type II behaviour resulting in the opposite effect of reducing wavefunction overlap and is therefore detrimental to PL emission intensity.

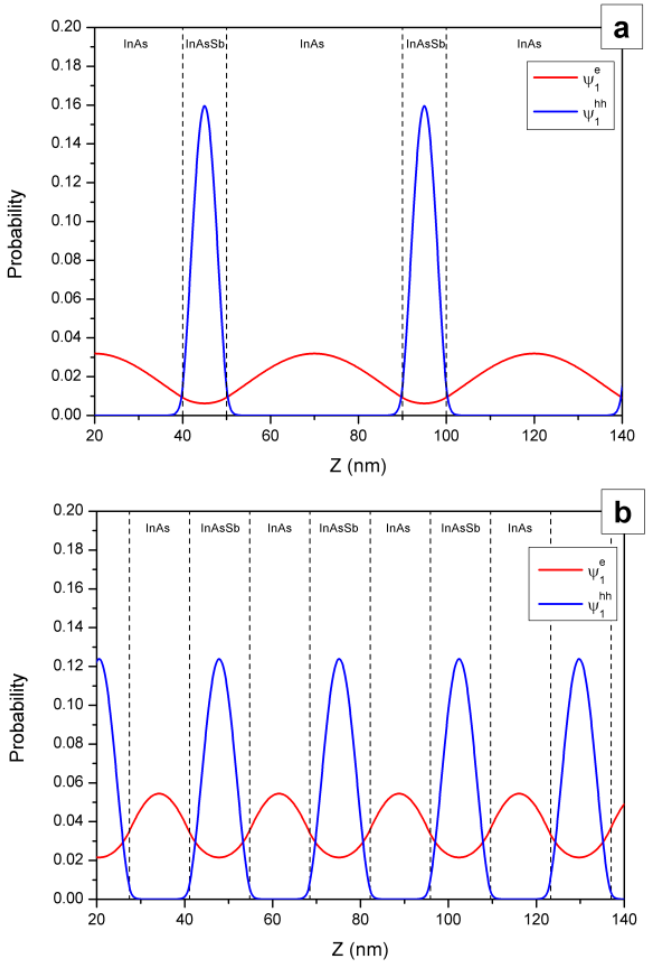

Figure 5.14 – Simulation of electron (red line) and heavy hole (blue line) probabilities within structures having comparable Sb content: a) MQW (Sample 1) and b) SLS (Sample 3). In both cases the heavy holes are strongly localised within the InAsSb QWs. The electron probability distribution inside the InAsSb QWs is significantly higher for the SLS structure, resulting in a larger overlap of the electron and heavy hole wavefunctions.

The wavefunction overlap was calculated for each structure and decreases with increasing Sb in both the MQW and SLS structures, giving a reduction of ≈ 2 % in the SLS and a decrease of ≈ 1 % in the MQW for a change of 1 % of the antimony content in the InAsSb well in each case. The radiative recombination rate is proportional to the matrix element squared M_P^2 which was calculated for each sample and the values are given in Table 5.3. The reduction of 13 x in the experimental PL spectra of the SLS samples as the antimony content increases in the QW layers (Fig. 6b) is more than the calculated approx. 5.4x decrease in M_P^2 shown in the table. Consequently, we attribute the remaining reduction to non-radiative recombination mechanisms which are dominated by Auger processes.

Sample	Sb [%]	Exp. 4 K PL peak energy [meV]	Sim. e_1-hh_1 transition at 4 K [meV]	M_P^2
MQW1	3.7	376	377	28
MQW2	4.3	367	369	20
SLS1	3.8	367	368	878
SLS2	6.2	318	334	450
SLS3	9.5	279	288	204
SLS4	13.5	242	233	95

Table 5.3 – Calculated and experimental values for e_1-hh_1 transition in MQW and SLS structures at 4K.

5.1.6 Auger processes

The PL spectra show a decrease of intensity as temperature increases. This is attributed to a progressively larger proportion of electron – hole recombination being non-radiative, as Auger processes are strongly temperature dependent (Equation 2.34). Furthermore, specific Auger processes each have their own activation energies (CHCC and CHSH processes defined by Equations 2.35 & 2.36) therefore it is possible to determine the dominant Auger process occurring in a structure according to Equation 2.37.

To consider the non – radiative processes the principal Auger activation energies (E_a) were determined using the transition energies and spin orbit split-off energies calculated using Nextnano. These values are given in Table 5.4 alongside the experimentally determined activation energies obtained from Arrhenius plots of the MQW (Figure 5.15) and SLS (Figure 5.16) structures, according to Equation 2.38.

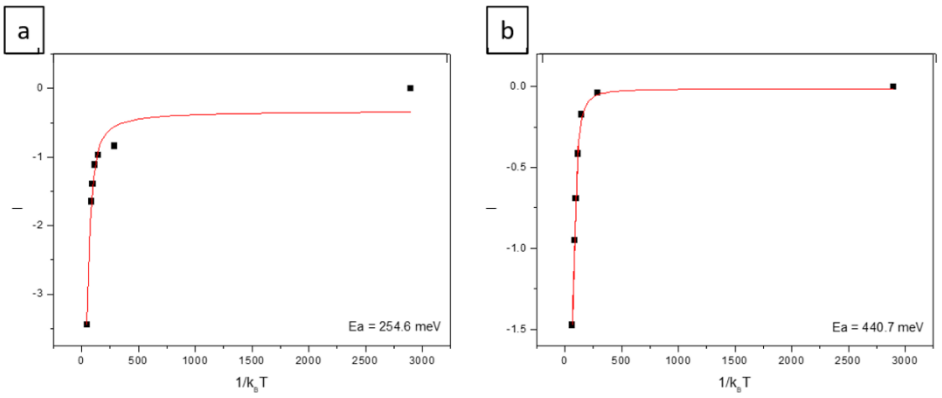

Figure 5.15 – Arrhenius plots for the two MQW structures.

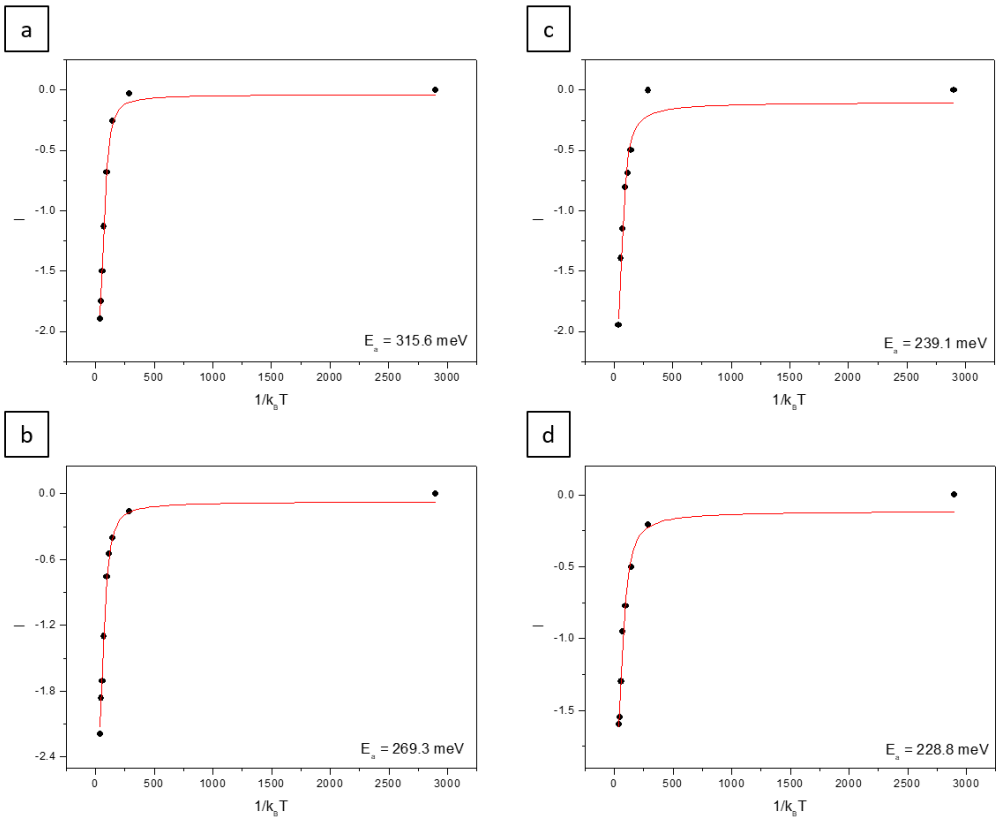

Figure 5.16 – Arrhenius plots for the four SLS structures.

Sample	Sb [%]	$\lvert E_T - \Delta_{SO} \rvert$ [meV]	$\left\lvert \frac{(E_T - \Delta)/E_T}{m_e/m_{SO}} \right\rvert$	E_a^{CHCC} [meV]	E_a^{CHSH} [meV]	E_a exp. [meV]
SLS1	3.8	46	0.9	19	11	316
SLS2	6.2	117	2.5	17	27	269
SLS3	9.5	180	4.5	15	42	239
SLS4	13.5	246	7.1	13	58	229
MQW1	3.7	39	0.7	20	9	255
MQW2	4.3	54	1.0	19	13	441

Table 5.4 – A comparison of the experimentally determined activation energy (from Arrhenius plot) and the calculated values (based on Nextnano simulations) of the main Auger recombination processes in the SLS samples.

Increasing the spin orbit split off energy such that it becomes larger than the band gap $(\Delta_{SO} > E_g)$ suppresses the CHSH process [32]. This excess is larger in the SLS samples than in the MQW samples, so CHSH Auger recombination is more suppressed in the SLS samples than in the MQW samples of similar antimony composition and CHCC dominates instead. For the SLS samples the condition given by Equation 2.37 is satisfied for all samples except SLS1, which has the lowest antimony content. Hence, CHCC Auger recombination is the dominant recombination process for the remaining SLS samples and the calculated activation energy for CHCC is found to trend to decrease with increase of antimony content. Meanwhile, for the MQW samples, the calculated CHSH Auger activation energy in the higher antimony sample (MQW2) is larger, consistent with CHSH suppression due to $E_T \sim \Delta_{S0}$ detuning, which is strongly dependent on antimony content.

The experimentally determined activation energy for the primary Auger process is significantly larger than both the theoretical activation energies for the CHCC and CHSH processes. The experimentally determined values of the activation energy have uncertainties that arise due to complications affecting the Gaussian deconvolutions at high temperatures where the PL emission peaks coincide with the CO_2 absorption

dip in the spectra. It is noted that the theoretically calculated activation energies do not include Coulombic effects or band bending in the simulations. Thermal escape of free carriers from the QWs is estimated for the MQW and SLS structures to be ~ 20 meV for the electrons and ~ 36 meV for the holes, which can be overcome at high temperatures and therefore influences the apparent activation energy of the primary Auger process derived from the Arrhenius plots based on the overall PL intensity. Despite this discrepancy of the numerical values the trend of a reduced Auger rate with increased Sb content in the QWs of these structures is noted. Clear differences observed in the temperature dependent photoluminescence spectra show that the holes remain better confined in the QW at higher temperatures in the SLS than in the MQW – this is attributed to Coulombic attraction arising from increased e-h overlap in the SLS because of thinner InAs barriers – which acts to maximise radiative free carrier recombination compared to non – radiative recombination processes.

5.2 InAs/InAsSb SLS LEDs

Mid – infrared light-emitting diodes (LEDs) are important for a variety of applications, as discussed in the Introduction chapter. The type II InAs/InAsSb SLS structure has been shown to exhibit strong hole confinement to preserve e-h recombination in the QWs up to room temperature whilst also acting to suppress the detrimental non – radiative recombination processes. Therefore, the development of MIR LEDs with an InAs/InAsSb SLS active region are promising for suiting their potential applications.

5.2.1 Growth & fabrication of LED devices

Two LED structures were grown by MBE based on the superlattice structure of the samples discussed previously (Section 5.1). Figure 5.17 shows a schematic of the LED device structure. Firstly, a 1.25 µm n – type (Te doped, 1 x 10^{18} cm^{-3}) InAs layer was grown. Then the undoped active region consisting of a 50-period InAs / InAsSb SLS (total thickness 1.4 µm) was grown. The InAs barrier and InAsSb quantum well thicknesses were 14 nm each, and the Sb content in the QWs was 4% and 6% using the same growth conditions as the first two samples. Finally, a 1.25 µm p – type (Be doped, 1.5 x 10^{17} cm^{-3}) InAs layer was grown to form the p region. These p – n^0 – n diodes were processed in the Cleanroom at Lancaster University using conventional photolithography and wet etching processing techniques to fabricate the LEDs (as described in Section 4.6 – Figure 4.8 shows a finished LED device mounted and wire – bonded on a header ready for undertaking measurements).

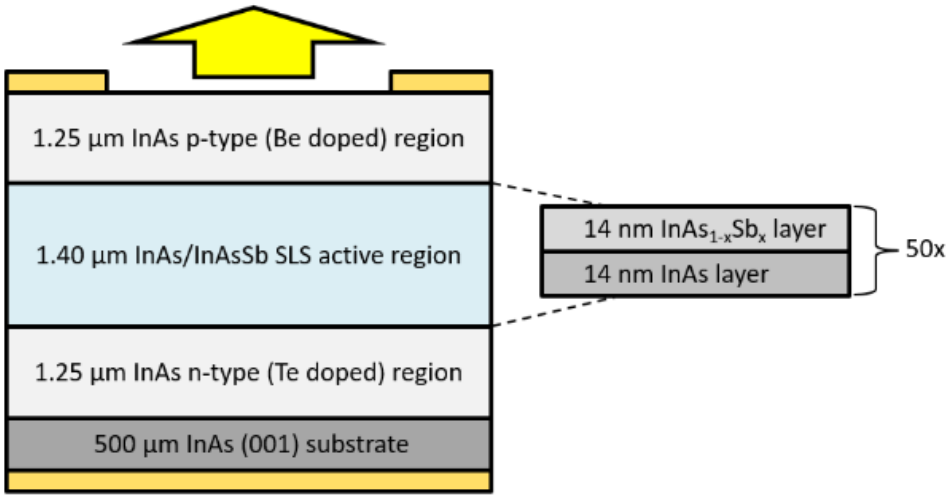

Figure 5.17 - Schematic of the LED structure containing the InAs / InAsSb SLS active region.

5.2.2 Comparison of LED electroluminescence with sample photoluminescence

Electroluminescence (EL) from the LEDs was generated and measured in accordance with the setup described in Section 4.4. The LEDs were operated with constant qCW current of 100 mA (1kHz, duty cycle 50 %). The 7 – 300 K electroluminescence emission spectra from the two superlattice LEDs, alongside the 4 – 300 K photoluminescence spectra of the corresponding samples SLS1 and SLS2, are shown in Figures 5.18 and 5.19. In each case the main peak is attributed to recombination between the lowest energy minibands ($e_1 – hh_1$).

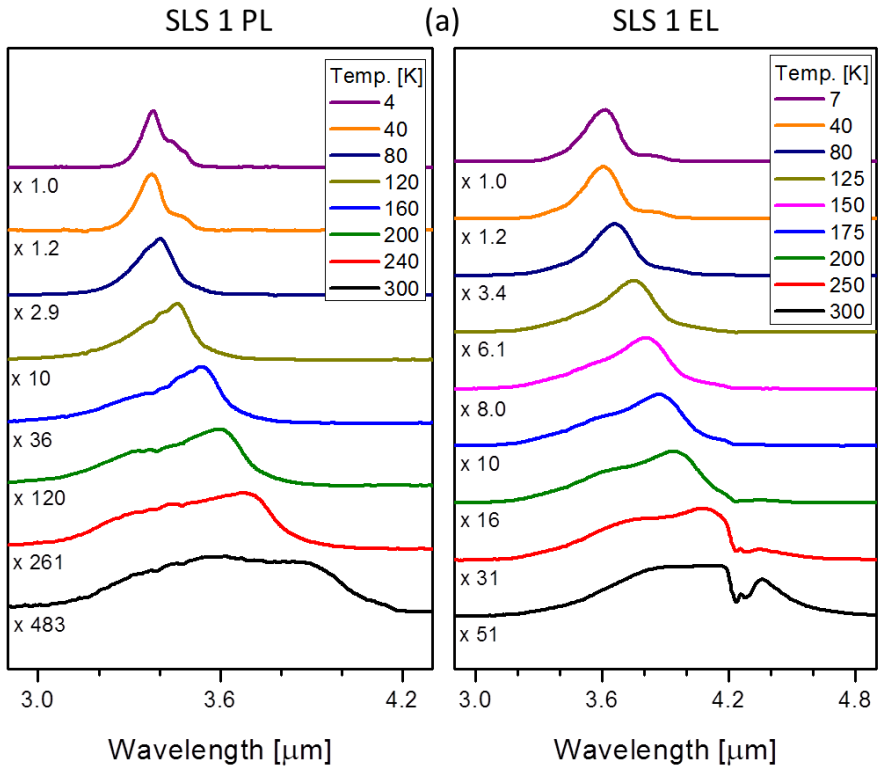

Figure 5.18 – Normalised (4 – 300 K) photoluminescence spectra of sample SLS 1 alongside the normalised (7 – 300 K) electroluminescence spectra of the corresponding LED.

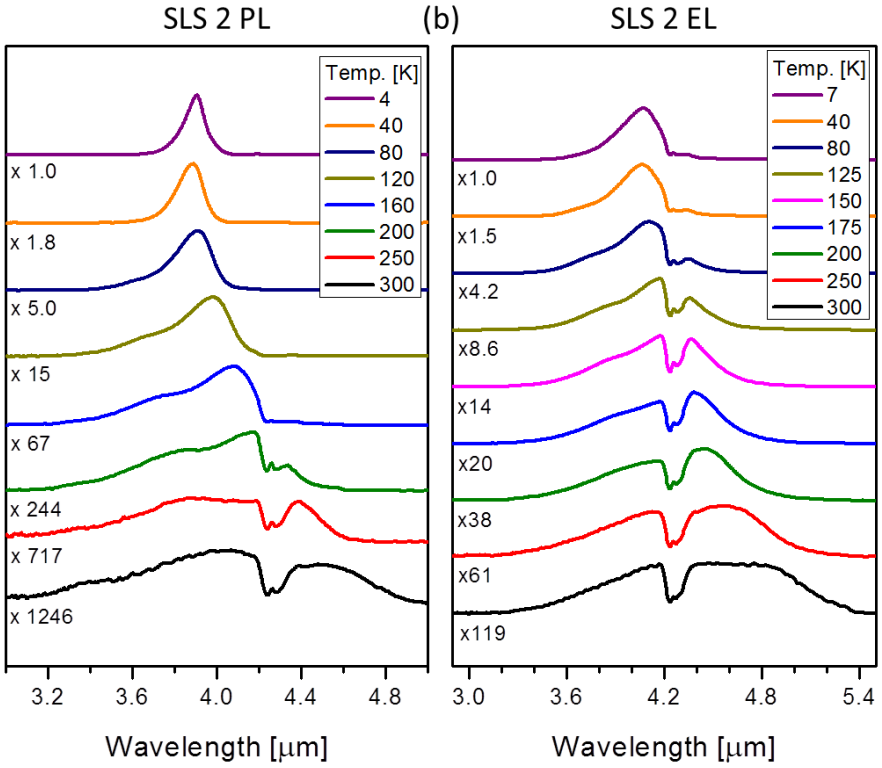

Figure 5.19 – Normalised (4 – 300 K) photoluminescence spectra of sample SLS 2, alongside the normalised (7 – 300 K) electroluminescence spectra of the corresponding LED.

The CO_2 absorption at 4.2 μm is clearly evident in both the 300 K EL spectra of the LEDs, indicating their potential for use in optical gas detection. Both PL and EL spectra exhibit a redshift in the emission wavelength, spectral broadening, and significant quenching with increasing temperature.

The temperature quenching of the two PL spectra is similar, with a slightly higher decrease in the emission intensity with temperature rise in SLS2 containing the higher antimony content. This quenching behaviour originates from the increased type II band offset which reduces the electron – hole wavefunction overlap and the matrix element for radiative recombination. Simulations using Nextnano [129] confirm that with increased antimony content in the InAsSb QWs the structure

becomes more type II, increasing both the conduction band and valence band offsets, resulting in greater confinement of the electrons in the InAs layers and of the holes in the QWs. This reduces the overlap of the electron and hole wavefunctions, lowering the radiative recombination rate of the electrons and holes, thus producing a higher density of free carriers (n). If these carriers can recombine by non – radiative processes, then a reduction in intensity of the emission from the structure is expected. Radiative recombination scales as n^2 but the temperature dependent non – radiative Auger recombination processes scale as n^3, causing larger temperature quenching to occur in the PL and EL of the higher antimony SLS sample and LED respectively. The higher magnitude of quenching of PL compared to EL is attributed to non-radiative recombination of carriers near the surface of the SLS samples which have an exposed active region. Simulation results indicate the broad emission spectra at room temperature (300 K) involve additional transitions into confined hole states.

The low temperature (4 K) photoluminescence spectra from the two SLS samples and the corresponding (7 K) electroluminescence spectra from the SLS LEDs are compared in Figures 5.20a and 5.20b. The 4 K PL peaks are identified at 3.38 µm and 3.91 µm, while the wider EL peaks are identified at 3.61 µm and 4.07 µm respectively. In both cases, the EL spectra are red – shifted to longer wavelength compared to the PL spectra. Joule heating can account for some of this peak shift considering the relatively high series resistance of these diodes, but we also suppose that this difference originates from the asymmetric distribution of the Sb in the superlattices shown in Figure 5.5, such that the depletion layer field in the LED results in a bias

dependent shift in the electroluminescence spectra. Similarly, the 300 K PL and EL spectra are shown together in Figures 5.20c and 5.20d. The PL peaks are identified at 3.65 µm and 4.06 µm, with the EL emission of the corresponding LEDs both peaking at ~ 4.2 µm. The linewidth of these 300 K spectra are broad, and Nextnano simulations of the SLS band structure reveal that up to three heavy hole states contribute to the emission near room temperature. There was no significant low energy emission due to radiative recombination in the InAs barriers associated with hole leakage

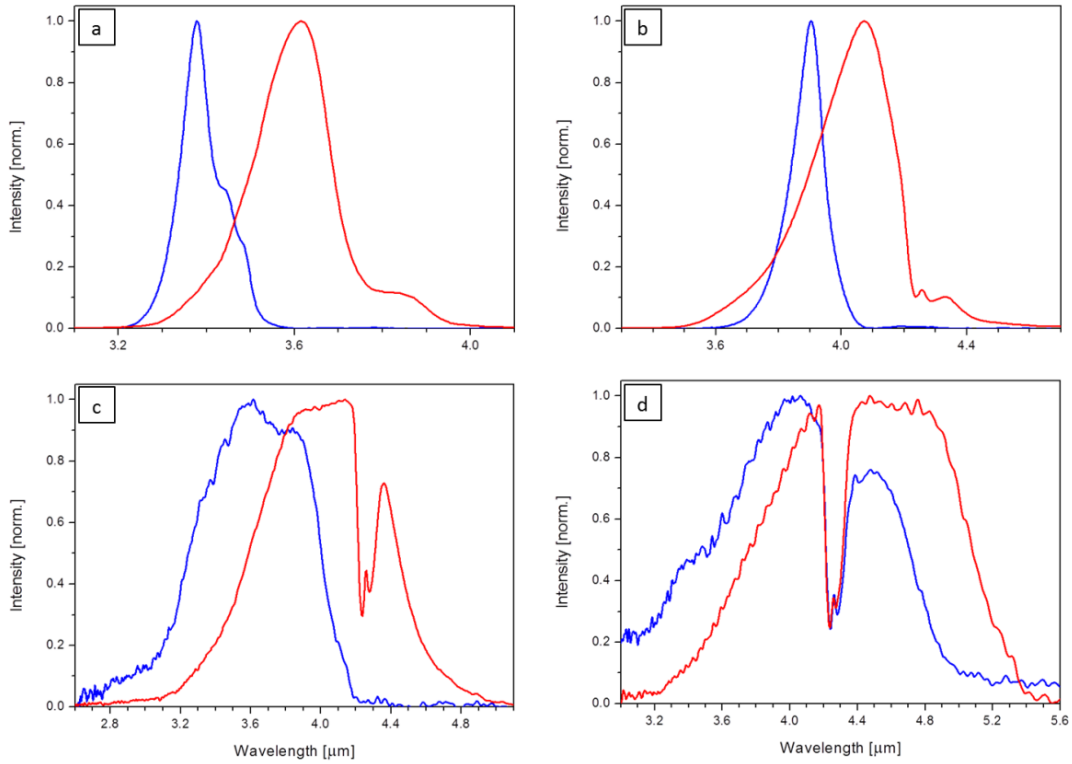

Figure 5.20 – Comparison of low temperature photoluminescence (4K) and electroluminescence (7K) spectra for the two SLS samples (a) SLS1 and (b) SLS2. Photoluminescence and electroluminescence (300K) spectra are shown in (c) and (d). Blue curves are PL and red curves are EL.

5.2.3 LED device characterisation

The current – voltage behaviour gives an insight into the performances of the devices. A resistor exhibits a linear relationship between voltage and current in accordance with Ohm's law (voltage = current x resistance). LEDs are diodes with p – n junctions that have a non – linear behaviour. The measured current – voltage characteristics of the two LED devices are shown in Figure 5.21.

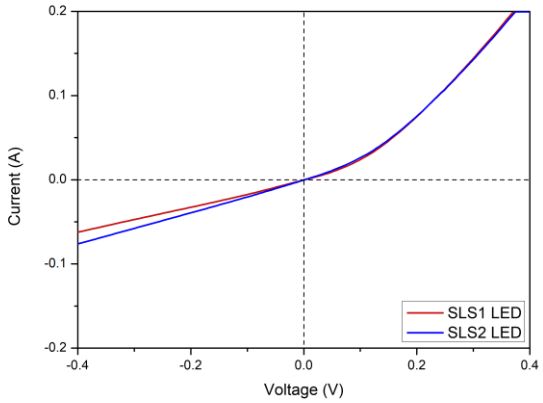

Figure 5.21 – IV (current – voltage) curves of the two SLS LEDs (measured at room temperature).

The operation is as follows. The diode is forward biased, passing a positive current through the devices. When this current exceeds the internal barrier potential, referred to as the turn on voltage point, then free carriers can flow across the p – n junction and undergo electron – hole recombination. This results in a large increase of the current for a small change of voltage (observed as the non – linear curve in the top right corner of Fig. 5.21). Conversely when the diode is reverse biased the diode blocks the current (except a very small leakage current) until the voltage across the junction becomes greater than the breakdown voltage, causing a sudden increase in reverse current (observed as a near linear line in the bottom left corner of Fig. 5.21).

The power – varied 300 K electroluminescence spectra of the two LEDs are shown in Figure 5.22 with the decrease of EL intensity with reduced excitation power. The CO_2 absorption dip at 4.2 µm features in the spectra of both devices.

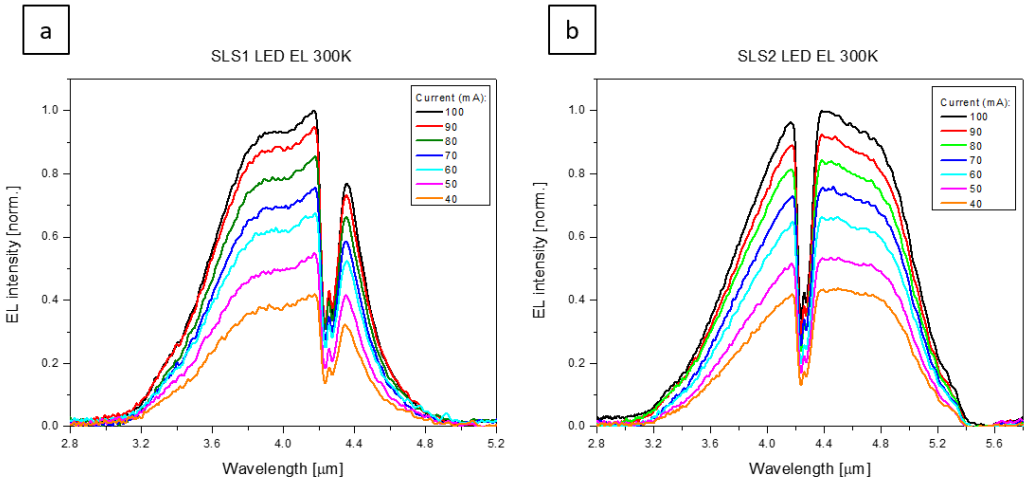

Figure 5.22 – Power dependent 300 K electroluminescence spectra of the two SLS LEDs, showing the reduced EL intensity with decrease of excitation power, and the CO_2 absorption at 4.2 µm.

Z plots (Figure 5.23) based on Equation 2.68 for the 300 K electroluminescence spectra generate the value of Z = 2.14 for both devices which indicates the dominant free carrier recombination process is radiative at room temperature, with no significant compromise due to high rates of non – radiative Auger processes based on Auger suppression exhibited by the SLS structures which are the active region of these LEDs.

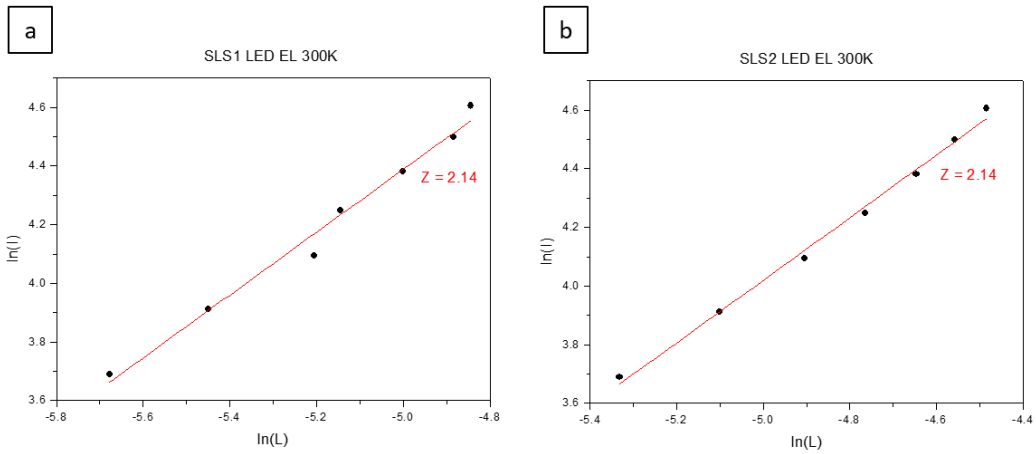

Figure 5.23 – Z plots for the SLS LEDs based on their 300 K EL spectra, producing Z values of Z = 2.14 indicating radiative recombination of free carriers is the dominant recombination process in both devices at 300 K.

Output power was measured as 8.2 µW for SLS1 LED and 3.3 µW for SLS2 LED corresponding to an emittance of 2.13 and 0.86 mW / cm^2, obtained using 100 mA quasi – CW injection current at 300 K and benchmarking to commercial Roithner InAsSb bulk LEDs. IQE values were calculated as 1.95 and 0.84 % respectively. These are similar to IQE values reported for InAs/InAsSb MQW LEDs emitting at similar wavelengths of 2.8 % [2], 2.2% [7] and 0.2 % [99]. The performance could be improved by including an electron blocking layer; in similar structures an AlSb barrier (at the interface between the p region and active region) prevents a large proportion of carriers escaping the active region and undergoing non – radiative recombination, which has been reported to increase IQE at 300 K by a factor of four [3, 2].

5.3 Excitons in the photoluminescence of InAs/InAsSb structures

Alongside the radiative recombination of free carriers (Section 2.2.1) electrons and holes can bind together to form excitons (Section 2.3) which can be observed in photoluminescence spectra under low excitation power.

5.3.1 Excitons in 4 K PL with varied excitation power

The 4 K PL spectra of the InAs/InAsSb MQW and SLS structures measured with excitation power over the range of 0.2 – 20 mW (Figure 5.24) show multiple peaks which evolve independently with power. In each case the lowest energy peak is associated with indirect exciton transitions between the QWs [38, 51, 41].

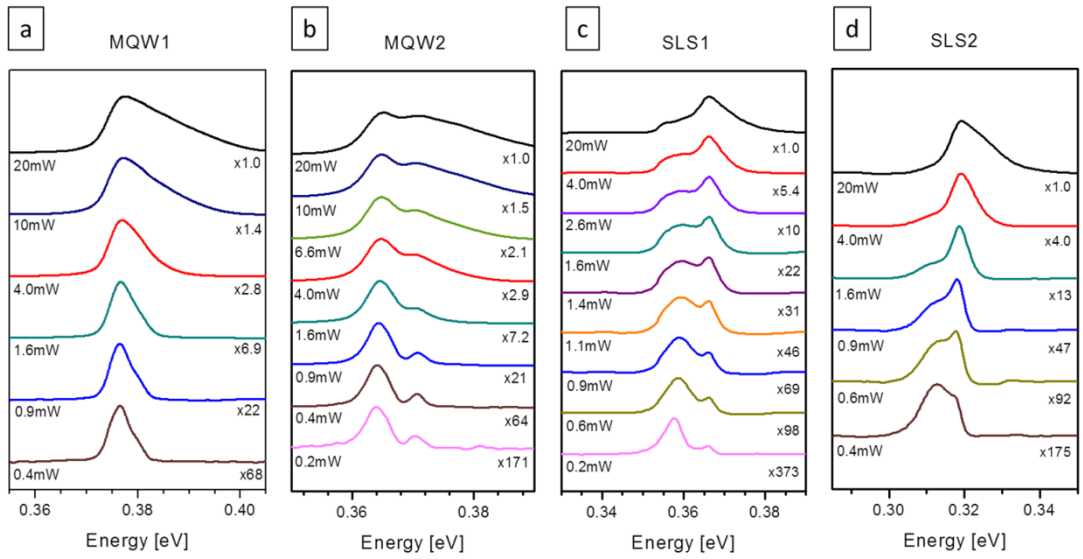

Figure 5.24 – Normalised power dependent 4 K PL spectra of the InAs/InAsSb MQW samples (a & b) and SLS samples (c & d) showing the evolution of different peaks. At low excitation power the lower energy peak is dominant; with increasing excitation power the higher energy peak becomes dominant.

Possible alternative explanations for these peaks in the PL spectra have been considered and subsequently discounted as follows. The first option is that variations in the composition and/or monolayer thickness fluctuations of the layers in the structures produce multiple e – hh_1 transitions at slightly different energies. These

transitions associated with the same QW transition would theoretically be very similar regarding linewidth, temperature dependence and power dependence. However, the two peaks are different in shape, and the intensities are observed to change differently with the change of excitation power. Furthermore, XRD structural characterisation and TEM imaging of these structures (Figures 5.2 – 5.5) shows structures with well – defined layers and without significant variations that could lead to alternative PL emission. The second option is that the two peaks are the e_1 – hh_1 and e_1 – hh_2 transitions in the QWs. Band structure modelling by Nextnano [129] was used to calculate these energies. As shown in Figure 5.25 the simulated energy of the e_1 – hh_1 transition matches well to the higher energy PL peak, and the difference in energy between these two e_1 – hh transitions is larger than the difference in energy between the two peaks identified in the PL spectra. Simulation results indicate the separation of the e_1 – hh_1 and e_1 – hh_2 transitions to be 17.4 meV (MQW1), 18.0 meV (MQW2), 10.2 meV (SLS1) and 10.9 meV (SLS2) whereas the deconvolutions of the PL spectra of the samples reveals the separation of the PL peaks to be around 4 – 8 meV with slight variations due to excitation power. Therefore, the lower energy peak observed in the PL spectra is ruled out as being from electron – hole recombination in the QWs and is instead attributed to excitons at low excitation power. The two peaks seen in the PL spectra of MQW2 (Fig. 5.24b) are assumed to also be present in the PL spectra of MQW1 (Fig. 5.24a) to mimic the behaviour, however these are of very small energetic separation such that it is difficult to deconvolute the spectra and identify them with confidence. Whilst the shapes of the very low ($P \leq 4.5$ %) spectra allude to the presence of two peaks that with tentative deconvolution indicate the behaviour of MQW2 is replicated, the

higher power spectra necessitate too much reliance on the deconvolution methods. Therefore, for only MQW2 and the two SLS samples are deconvolutions and further analysis of the power – dependent 4 K PL presented for these exciton related results.

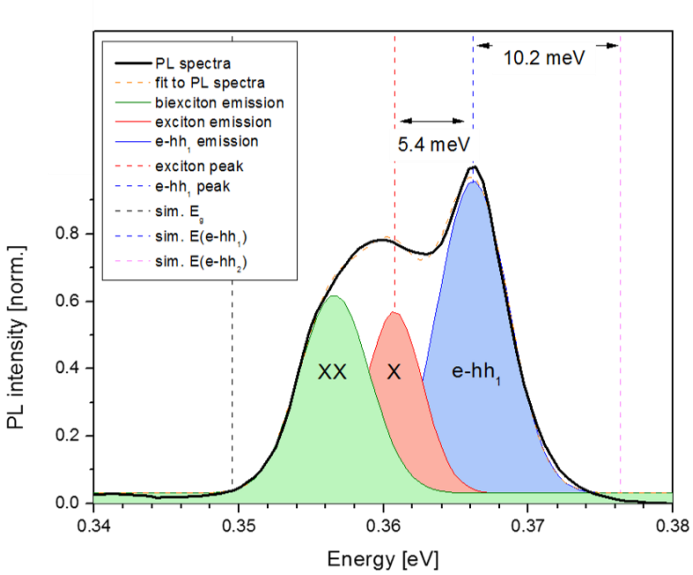

Figure 5.25 – Deconvolution of the 4 K PL spectra (SLS1 sample, 8 % power) showing the identification of three distinct peaks of close separation in energy, attributed to the existence of biexcitons and excitons which produce photoluminescence at lower energies alongside photoluminescence from the higher energy e - hh_1 transition in the QWs. Overlaid are simulated energies of the band gap (black dashed line), e - hh_1 transition (blue dashed line) and e - hh_2 transition (pink dashed line), showing good agreement of theory and experiment in the energy of the e - hh_1 peak and thus confirming excitonic features in the PL spectra are real.

The intensities of the PL peaks from the exciton states and electron – hole radiative recombination, obtained from deconvolution of the 4 K power – dependent PL spectra (Fig. 5.24), are presented in Figure 5.26. Integrated areas of the peaks were considered alternatively to the absolute peak intensity to take spectral broadening into consideration, as shown in Figure 5.27. In both cases the results show similar trends. For all samples, at low power the emission from excitons (red points) is almost entirely responsible for the measured photoluminescence. With increasing power, the intensity of the PL contribution from radiative recombination of electrons and holes progressively increases (blue points). This is due to the higher rate of

radiative recombination generated by the higher free carrier concentration, as well as the free carriers acting to screen the Coulomb attraction that binds excitons together and thus facilitates their breakup, reducing the excitonic PL contribution.

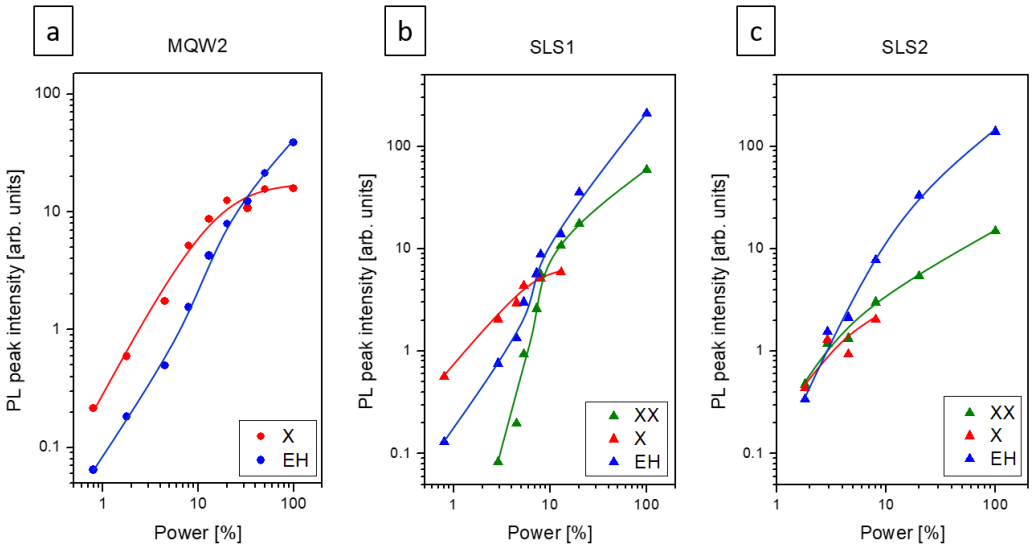

Figure 5.26 – Photoluminescence peaks (intensities) of the low energy biexciton (green points) and exciton (red points) and the high energy electron – hole plasma (blue points) emissions, deconvoluted from the power dependent 4 K PL spectra of MQW2 (a) and SLS1 & SLS2 (b & c) samples. The x-axis is plotted as a power fraction where 100% represents laser power of 20 mW (2.5 W / cm^2 at the sample surface). The overlaid lines act as a guide to the eye to show the trends of the peaks.

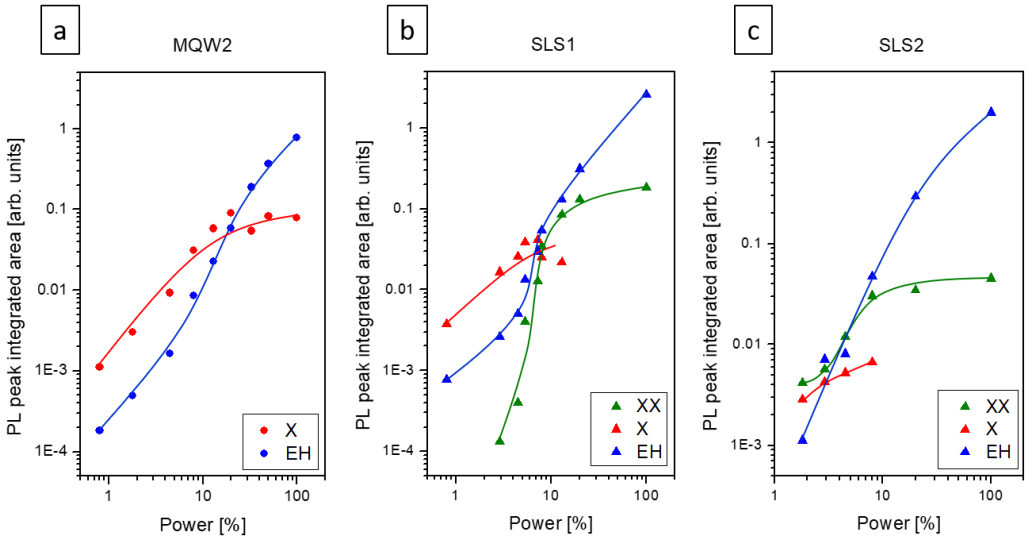

Figure 5.27 – Photoluminescence peaks (integrated areas) of the low energy biexciton (green points), exciton (red points), and high energy electron – hole plasma (blue points) emissions, deconvoluted from the power dependent 4 K PL spectra of MQW2 (a) and SLS1 & SLS2 (b & c) samples. The x-axis is plotted as a power fraction where 100% represents laser power of 20 mW (2.5 W / cm^2 at the sample surface). The overlaid lines act as a guide to the eye to show the trends of the peaks.

In the PL spectra of the two SLS, an additional third peak at even lower energy is identified (green points) which is attributed to biexcitons present in the structures. Strong evidence for excitons and biexcitons coexisting is provided by the different slopes for the change in intensity with power for the two emissions. Biexcitons have often been disregarded due to supposedly being less robust than excitons against screening effects by free carriers that cause their breakup [52]. However, theoretical predictions [50] and experimental evidence [52] of biexcitons in QW structures support this identification of their existence. The condition for biexciton formation is defined by Equation 2.50 which gives the critical QW separation distance calculated at 22 nm below which biexciton formation is possible. The MQW structures studied have QW separation of 40 nm, whereas the SLS structures have QW separation of 14 nm, indicating why biexcitons are identified in the PL spectra of the SLS1 and SLS2 samples but not for the MQW2 sample. Biexciton intensity is found to increase with increased excitation power, contrary to the decreasing emission from excitons. Comparison of the relative intensities of the biexciton and exciton PL is shown in Figure 5.28. At the lowest power there is near zero emission from biexcitons. As the power is increased the intensity of the biexciton emission rapidly increases, surpassing exciton emission at about 8.7 % power in SLS1 and is already dominant in SLS2 at the lowest power. At high power (above ≈ 20 %) there is negligible identified emission from the excitons. Whilst biexciton emission dominates the low energy photoluminescence, biexcitons eventually suffer from the same ionising effects by the free carriers as experienced by the excitons. With further power increase the relative intensity of the biexciton PL decreases, with this change found to coincide with the Mott transition that signifies the majority of the free carriers are undergoing

radiative recombination rather than binding together to form excitons or biexcitons, thus significantly increasing the overall PL contribution from radiative recombination of these free carriers.

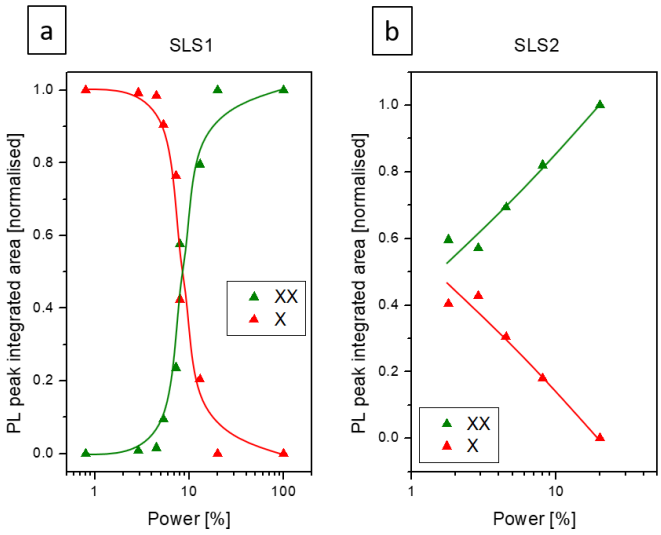

Figure 5.28 – Relative emission intensities of the low energy biexciton (green points) and higher energy exciton (red points) photoluminescence peaks deconvoluted from the power dependent 4 K PL spectra of the two SLS samples. The x-axis is plotted as a power fraction where 100% represents laser power of 20 mW (2.5 W / cm^2 at the sample surface). With increasing power, the relative intensity of the biexciton emission becomes more dominant as the source of the low energy photoluminescence.

The Mott Transition, defined as the change of the dominant PL source from exciton emission to radiative electron – hole recombination, is identified as the crossover point of the curves shown in Fig. 5.29. Our results provide evidence for a smooth rather than an abrupt transition in these structures. It is interesting to note that the transition occurs at different excitation powers in the different samples. The power at which this crossover occurs is governed by two processes:

1. The number of free carriers which undergo radiative recombination.
2. The binding energy of the excitons, which determines the free carrier concentration necessary to sufficiently screen the Coulomb attraction to break up the excitons (and reduce the photoluminescence).

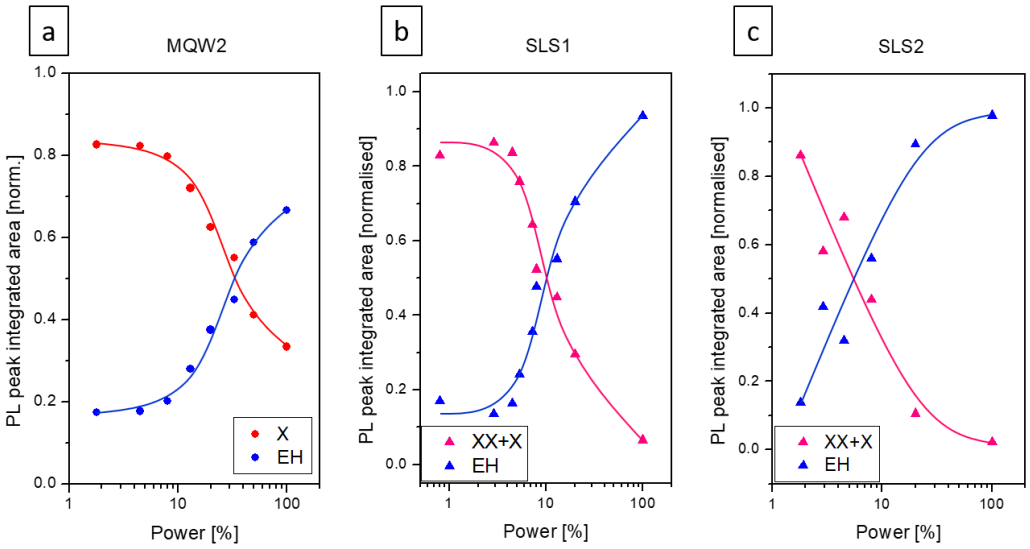

Figure 5.29 – Relative emission intensities of the low energy excitonic (excitons and biexcitons combined) photoluminescence and the higher energy photoluminescence from electron – hole recombination, deconvoluted from the power dependent 4 K PL spectra of the MQW2 (a) and the two SLS (b & c) samples. The x-axis is plotted as a power fraction where 100% represents laser power of 20 mW (2.5 W / cm^2 at the sample surface). With increasing power, the relative intensity of the PL emission from radiative recombination of free carriers becomes dominant over excitonic PL emission.

The overlap of the electron and hole wavefunctions inside the QWs dictates the rate of radiative recombination. This e – h wavefunction overlap is significantly larger in the SLS compared to the MQW. In addition, the SLS structure is 1.4 µm thick with 50 QWs whereas the MQW structure is 0.5 µm thick with 10 QWs, such that the likelihood of free carriers undergoing radiative recombination is higher in the SLS (rather than passing through and undergoing non-radiative recombination at the substrate interface, since no electron confining barriers are present). It is therefore expected that the radiative recombination of free carriers will become the dominant contributor to the photoluminescence at a lower power in the SLS samples. This is observed, with the crossover point occurring at 35 % in MQW2 and at the significantly lower powers of 10 % and 6 % in the SLS samples. Furthermore, the lower power of this crossover in SLS2 compared to SLS1 is explained by consideration of the exciton binding energy (Figure 5.31) which is noted to be lower in SLS2 than in

SLS1 meaning a lower concentration of free carriers is necessary to facilitate exciton ionisation, which takes precedence over the rate of radiative recombination of the free carriers in terms of the relative PL intensities.

The critical free carrier density η_c corresponding to the Mott transition can be estimated theoretically using Equation 2.48 with inputs of QW separation (*d*, fixed value based on the structure) and exciton energy shift (*ΔX*, determined from the experimental data). Alternatively, the carrier density corresponding to the Mott transition point was estimated using Equation 2.49 based on the 785 nm red laser used in the PL / EL setup providing a measured laser power of 2.5 mW / cm^2 at full power, with the parameters of the absorption coefficient ($\alpha = 2 \times 10^4$ cm^{-1} for InAs) and decay rate (τ = 1 ns), to give a carrier density of $n = 1.98 \times 10^{11}$ cm^{-3} at full laser power. This value is then multiplied by the laser power fraction corresponding to the crossover point as identified from Figure 5.29 to give an estimate of the free carrier density in each structure at which the Mott transition occurs. These experimental and theoretical values along with other results are summarised in Table 5.5. Both methods present the same trend for the SLS, matching the other parameters to indicate that the lower exciton binding energy in SLS2 compared to SLS1 means the Mott transition occurs at a lower excitation power, corresponding to a lower free carrier density in the structure, due to the lower exciton concentration and thus a lower exciton contribution to the measured photoluminescence of the structures.

For MQW2 the significantly lower theoretical Mott density can be explained by its derivation based on the shift in the energy of the exciton emission which is found to

be very small compared to that exhibited by the SLS. Also, it is noted by Kirsanske [38] that this simple model underestimates the Mott density. The significantly larger value of the experimental Mott density for MQW2 compared to the SLS is the result of the significantly higher power necessary to provide enough free carriers to raise the radiative recombination rate, directly related to the significantly lower e – h wavefunction overlap in the MQW structure.

Further to obtaining the relative intensities of the PL from biexcitons / excitons and from electron – hole radiative recombination, the change in energy of the PL peaks with power variation is studied. These results are shown in Figure 5.30.

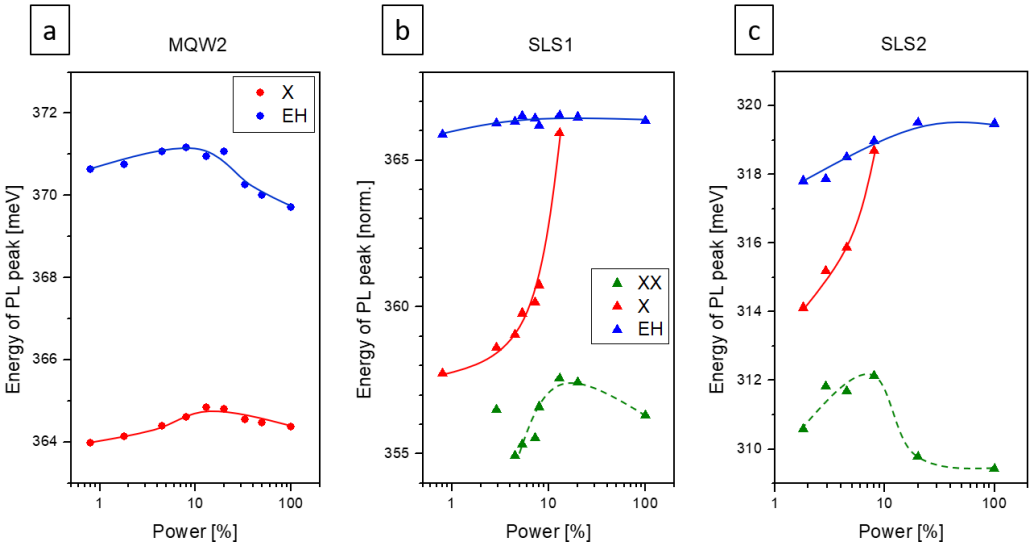

Figure 5.30 – Energies of the PL peaks deconvoluted from the 4 K PL spectra of the MQW and SLS samples. Green points: biexciton PL peak; red points: exciton PL peak; blue points: e – hh_1 PL peak.

In all three samples, the e – hh_1 peak remains almost constant in energy over the power range within a variation of about 1 – 2 meV. The exciton PL peak is found to undergo an increase in energy as power increases, by only about 1 meV in MQW2 but by several meV in SLS1 and SLS2. This is explained by an increasing concentration of excitons which leads to exciton – exciton repulsion that raises the energy at which

new excitons form [136]. The exciton binding energy is defined as the energetic difference between the $e_1 - hh_1$ and exciton peaks and gives an indication of the ability of the excitons to be perturbed by the free carriers. Thus, the reduction in the energetic separation between the exciton and $e - hh_1$ PL peaks leads to the trend of reducing exciton binding energy with increased power (Figure 5.31). This reduction of exciton binding energy is in good agreement with theoretical and experimental literature for coupled QW which show a reduction of several meV in the binding energy as excitation power is increased [38, 40].

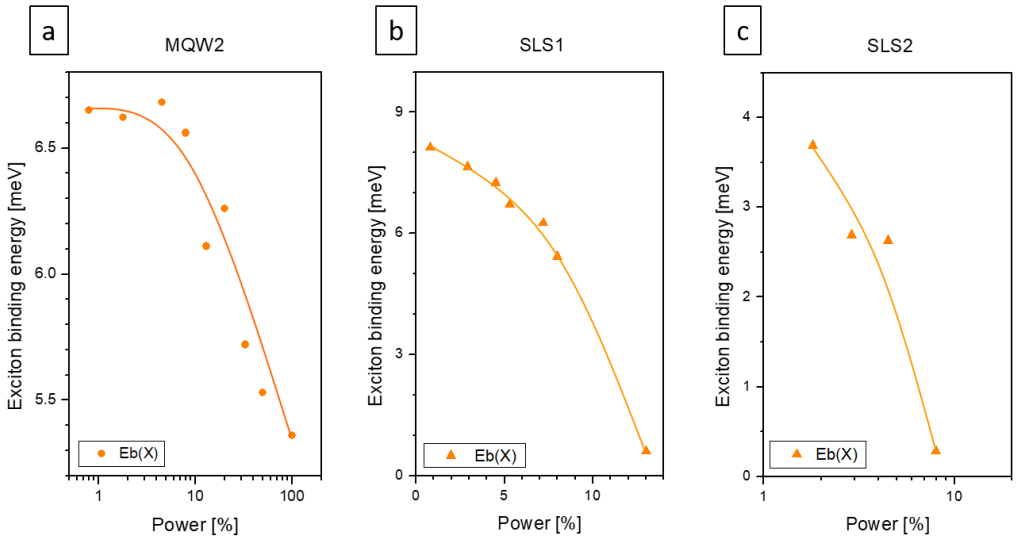

Figure 5.31 – Dependence of excitation power on the exciton binding energy in MQW2 (a) and SLS1 & SLS2 (b & c) samples, showing decrease with increasing power due to screening by the e-h plasma.

Sample	Sb of QW [%]	e-h wave – function overlap [%]	Laser power fraction at n_c [%]	Exciton peak shift ΔE_x [meV]	Exciton binding energy at n_c [meV]	Theoretical Mott density n_c [cm^{-2}]	Experimental Mott density n_c [cm^{-3}]
MQW2	4.3	4.9	0.35	1.39	5.8	2.31×10^{12}	6.93×10^{10}
SLS1	3.8	22.8	0.10	7.52	3.5	2.23×10^{13}	1.98×10^{10}
SLS2	6.2	15.6	0.06	3.41	1.1	1.01×10^{13}	1.19×10^{10}

Table 5.5 – A summary of the results from the power dependence of the 4 K PL spectra of the samples, stating the power fraction and corresponding excitation power at which the Mott transition occurs, as well as the theoretical and experimentally derives values for Mott density.

5.3.2 Excitons in temperature varied PL with low excitation power

In principle, excitation intensity and temperature should both contribute independently to the PL emission from excitons in the QWs. In the samples a gradual ionization of the low – energy excitonic PL peak with increasing temperature is observed under fixed low exciton power, as shown in Figure 5.32.

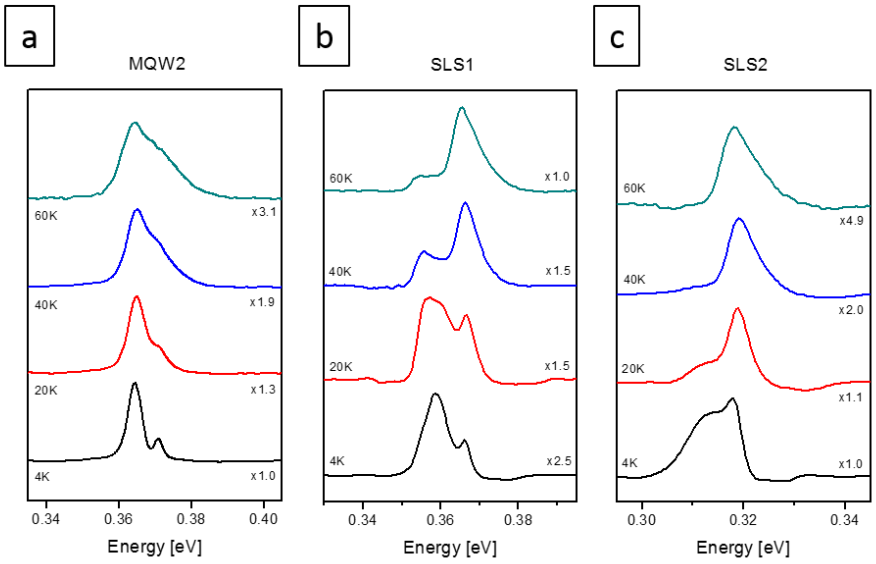

Figure 5.32 – The temperature dependence of the PL emission from each of the samples measured using constant low excitation conditions (4.5 % power for MQW2, 2.9 % power for SLS1 & SLS2).

The intensities of the exciton, biexciton and e – hh_1 PL peaks obtained from deconvolution of the PL spectra (Fig. 5.32) are shown in Figure 5.33 normalised to the overall emission intensity of each spectrum. With increasing temperature, the intensity of the exciton peak decreases and the intensity of the e – h recombination peak increases. This is caused by the rising temperature increasing the thermal energy of the free carriers which facilitates the breakup of the excitons [21]. Significant emission from biexcitons is identified in the SLS spectra, as biexcitons are more resistant to breakup than the excitons. This is observed as an increase relative to exciton emission (Figure 5.34) however at higher temperatures the sufficiently

higher energy of the free carriers means the biexcitons are also ionised. From the experimental results the Mott transition is determined to occur at temperatures of approximately 17 K in MQW2, at 33 K in SLS1 and 12 K in SLS2.

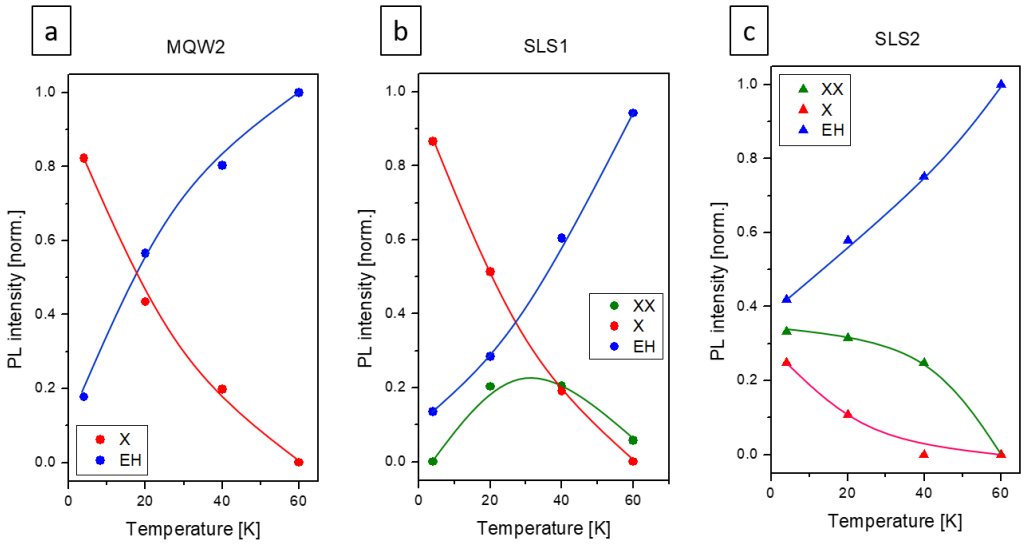

Figure 5.33 – A comparison of the relative intensities of the peaks identified in the 4 – 60 K PL spectra under constant low excitation intensity (4.5 % power for MQW, 2.9 % power for SLS). With increasing temperature, the intensity of the exciton emission is found to decrease whereas the radiative recombination of free carriers (electron – hole plasma) increases, as well as weak emission from biexcitons being identified in the SLS spectra. The temperature varied results at fixed low power show similar behaviour to that of power variation at 4 K.

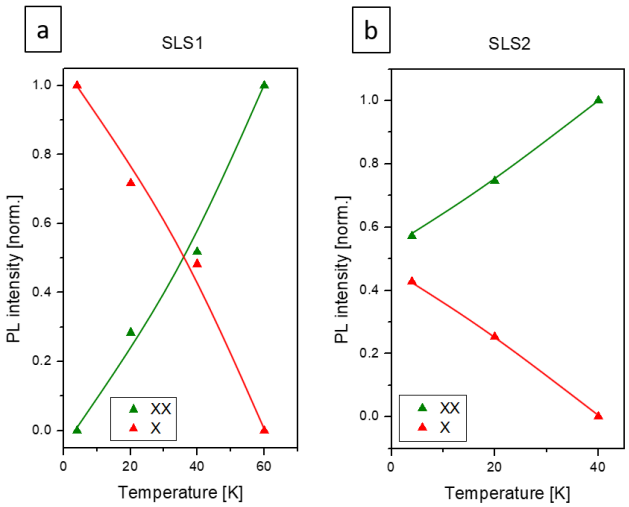

Figure 5.34 – Relative emission intensities of the low energy biexciton (green points) and exciton (red points) photoluminescence peaks deconvoluted from the temperature dependent low power PL spectra of the SLS samples. The x-axis is plotted as a power fraction where 100% represents laser power of 20 mW (2.5 W / cm^2 at the sample surface). With increasing power, the relative intensity of the biexciton emission becomes more dominant as the source of the low energy photoluminescence.

The change in energy of the PL peaks with increased temperature is shown in Figure 5.35. In the MQW sample the e – h peak trends to decrease in energy, consistent with band gap narrowing with temperature [19]. This peak in the SLS samples exhibits a slight increase of energy, a blueshift in the emission wavelength characteristic of type II structures [7], before trending downwards in energy with further increase of temperature. The energy of the exciton peak in the MQW sample is found to not change significantly in energy over the temperature range. The exciton and biexciton PL peaks of the two SLS samples both undergo significant increases in energy over the temperature range, moving towards the e – h peak.

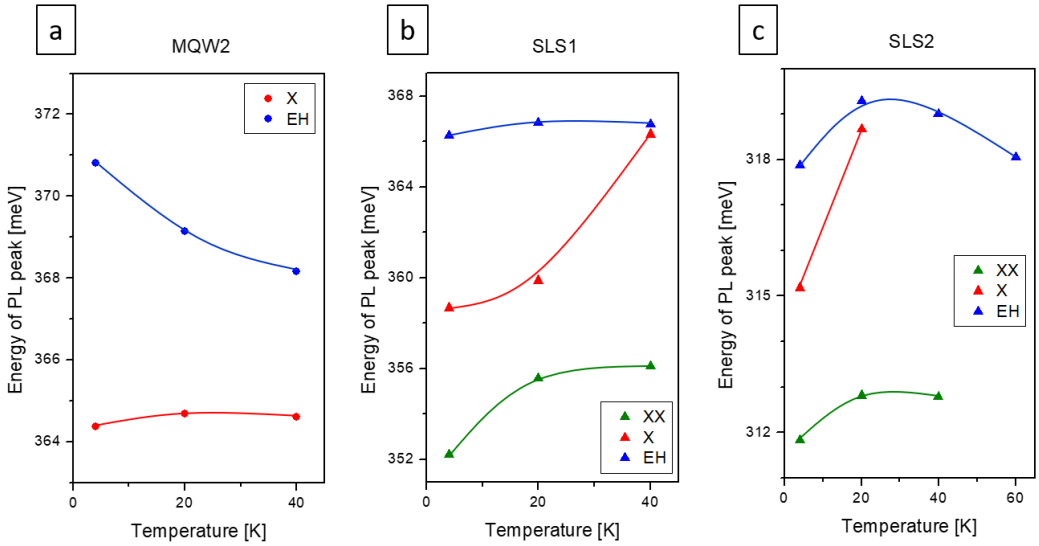

Figure 5.35 – Energy change of the PL peaks with temperature for (a) MQW2, (b) SLS1 and (c) SLS2.

Exciton binding energy (Figure 5.36) decreases for all samples with the increase of temperature, due to the increased thermal energy of the free carriers aiding the ionisation of the excitons.

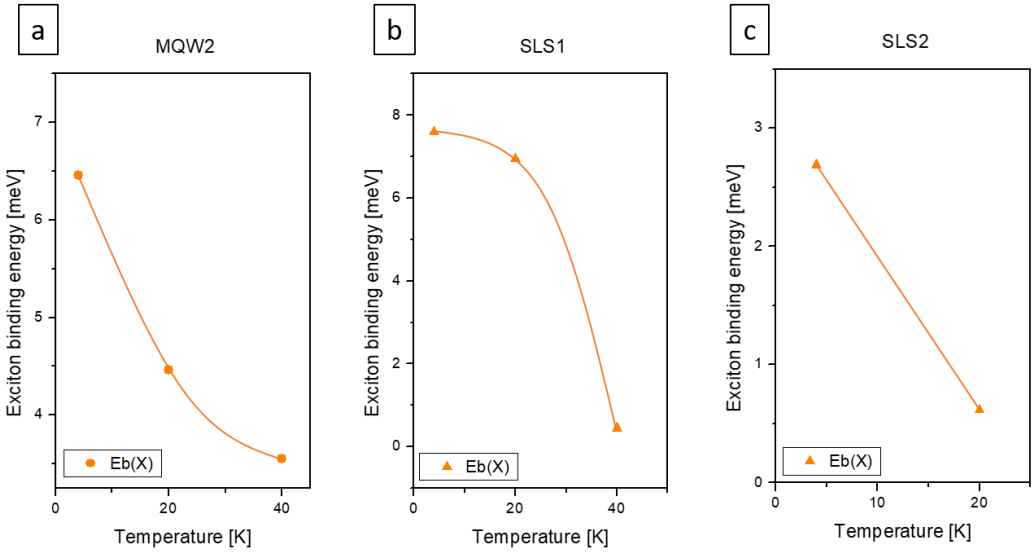

Figure 5.36 – Exciton binding energy decrease with temperature rise for the MQW and SLS samples.

A summary of the results for the Mott transition temperature and related exciton binding energy for the MQW and SLS samples is provided in Table 5.6. The results show the same trends as for the study of the power varied 4 K photoluminescence of these samples, indicating that both excitation power and temperature affect the characteristics of the excitons in these structures.

Sample	Mott Transition temperature [K]	Exciton binding energy at MT [meV]
MQW2	17	4.8
SLS1	33	2.7
SLS2	12	1.6

Table 5.6 – Mott transition temperature and corresponding exciton binding energy in the structures.

Chapter 6

Summary & conclusions

A series of InAs/InAsSb strained – layer superlattices (SLS) with low antimony content (Sb = 3.8 – 13.5 %) were grown by MBE on InAs substrates and characterised using X – ray diffraction (XRD) and transmission electron microscopy (TEM) imaging. Two InAs/InAsSb multiple quantum well (MQW) samples of similar antimony content to the SLS (Sb = 3.7, 4.3 %) were also characterised by XRD and acted as a comparison to the SLS samples. The 4K photoluminescence (PL) spectra of these samples exhibit the expected peak shift to longer wavelength and a reduction in intensity as the Sb content in the QWs is increased. Over the 4 – 300 K temperature range the SLS samples exhibit superior temperature quenching behaviour of the PL compared with the MQW samples, making them more attractive for use in the active region of emitters LEDs designed to operate at room temperature. Meanwhile, band structure simulations highlight the effects of changing the superlattice, specifically the antimony content and the layer thicknesses, to tailor the overlap of the electron and hole wavefunctions and maximise the radiative recombination rate.

Analysis of the temperature dependence of the PL emission spectra enabled the extraction of energies for thermal carrier escape from the QWs and for the primary non – radiative Auger process, which was determined to be CHCC in the SLS structures and CHSH in the MQW structures. In the SLS structures the theoretical activation energy for the CHCC process exhibits a downward trend with increasing

antimony content due to the reducing band gap moving the conduction and valence bands energetically closer. The experimental activation energies replicate this trend.

The MQW samples exhibit a changeover in the dominant radiative recombination above ≈ 100 K associated with the thermal escape of holes from the QWs and the subsequent electron – hole recombination occurring directly in the InAs layers. This behaviour was not observed in the SLS, due to the increased electron – hole wavefunction overlap and a larger Coulomb attraction which keeps the holes strongly confined in the QWs. Therefore, the SLS design is considered superior to the MQW for the active region in room temperature MIR LEDs.

Following the study of these samples, two p – n^0 – n diode samples were grown containing the corresponding superlattices in the active region and fabricated into LEDs. Mid – infrared electroluminescence was obtained from both these samples over the temperature range 7 – 300 K and both LEDs exhibit emission coincident with the main CO_2 absorption band near 4.2 µm at room temperature.

Temperature quenching was observed in both PL and EL spectra, in both cases being more significant in the structures with higher antimony content in the QWs, which is attributed to the reduced electron – hole wavefunction overlap meaning a higher concentration of free carriers which then recombine non – radiatively by Auger processes. Simulation results indicate the broad emission spectra at room temperature involve e – h recombination from additional confined hole states. These prototype LEDs produced output powers of 8 µW and 3 µW at 100 mA injection

current at room temperature with IQE of ≈ 2 % and ≈ 1 % respectively. The EL and PL spectra exhibit a redshift in wavelength and spectral broadening, as well as significant quenching with increasing temperature.

In addition to the development of mid – infrared LEDs, indirect excitons and biexcitons have been observed in the mid – infrared photoluminescence from type II InAs/InAsSb multiple quantum well (MQW) and superlattice (SLS) structures at 4 K under varied excitation power (0.2 – 20mW) and at up to 60 K under low excitation power (≤ 0.9 mW). The Mott transition at which the dominant photoluminescence process changes from exciton emission to radiative recombination of free carriers was identified in all the samples, with the results showing compelling evidence for a gradual Mott transition which is dependent on the QW structure, excitation power and temperature. Considering the 4 K photoluminescence spectra, the Mott transition was found to occur at significantly lower excitation power in the SLS samples compared to the MQW sample. This is attributed partly to the higher electron – hole wavefunction overlap resulting in a higher rate of free carrier radiative recombination and thus a lower required concentration of free carriers for this process to become the dominant contributor to the photoluminescence. In addition, the exciton binding energy is found to be higher in the MQW structure enabling the excitons to resist ionisation up to a higher free carrier density. The higher crossover in the MQW sample could also be attributed to a higher rate of non – radiative free carrier recombination as the result of being a thinner structure with fewer QWs. For the SLS samples a lower power to facilitate the Mott transition occurs in the structure of higher antimony content, in which the excitons have a

lower binding energy, indicating that the crossover is more affected by ionisation of excitons (and a reduction of their PL) rather that the rate of free carrier radiative recombination. The corresponding Mott density at the Mott transition point is calculated from theory and experimentally derived to be on the order of 10^{10} cm^{-3} in good agreement with experimental findings. The temperature dependent (4 – 60 K) photoluminescence spectra under fixed low excitation power ($P \leq 0.9$ mW) reveal exciton, biexciton and e – hh_1 peaks that behave similarly to the trends identified in the 4 K PL spectra. The excitons (in MQW and SLS) and biexcitons (in SLS only) are found to exist in the structures up to ≈ 40 K before ionisation by the free carriers with increased thermal energy. These results show that the Mott transition is affected by the structure, excitation power and temperature.

Suggested Further Work

Since strained layer superlattices offer additional freedom in design it is of interest to further develop LED structures based on our findings for mid-infrared applications. There are several approaches that have been identified that could improve device performance. Firstly, reducing the thickness of the layers would increase the overlap of the electron and hole probability wavefunctions, which is directly related to increasing the rate of radiative free carrier recombination. However, to achieve the same emission wavelength the active region would have to be made thicker to compensate which whilst providing additional QWs for electron – hole recombination may result in a higher level of strain present in the structure that degrades the structural quality. Further to this, the thinner layers will adjust the electron and hole energies such that the band gap is increased, shortening the

emission wavelength, which can only be rectified by increasing the Sb content of the QWs which itself acts to increase the strain. Secondly, the inclusion of an electron blocking barrier either side of the active region would confine the electrons and reduce non – radiative recombination at the interface with the substrate or the surface, which should lead to a higher proportion of the free carriers recombining radiatively. Thirdly, improved growth techniques could reduce the presence of defects in the structures that may result in non – radiative SRH recombination or unintended radiative recombination processes at energies different to the target. Fourthly, improving the fabrication techniques could improve efficiency by reducing issues such as current crowding and the top contact limiting light emission.

Further reconciliation between the simulations and experimental results would provide greater support for investigating the numerous characteristics of these structures and to guide future developments. A noted suggestion is to model structures with a non – square profile for the layers and compositions which would more accurately replicate the imperfections identified in the real structures.

With regards to the independent study of excitons and biexcitons existing in the InAs/InAsSb structures, additional measurements over a wider power range would strengthen the results and give an improved comparison between the MQW and the SLS. A clearer picture of the temperature dependence would emerge from additional temperature data. Time – resolved measurements and with the samples studied under applied electromagnetic fields, techniques employed in work reported by others, would be beneficial to understand better excitons in these type II structures.

Appendix A

EPILIST1 EDITOR -- QMK 642 ON N-INAS <EpiStep List + Full Data>

File View EpiList Edit Add Integrity Window Settings Z-LogOut

Setp	Excess As(V)	T_S 500.00°C +15.0rpm (In:0.8074(1),790); As(V):0.67898(1),+250; (Sb(V):0.0001(1),+0Iz)...>>...		undoped	t=At Run Time
Power	Excess As(V)	T_S 500.00°C +15.0rpm ...>>... (InT890(1),890)		undoped	t=At Run Time
3		EPILIST START...			
4	Matrix InAs(V)	T_S 500.00°C +15.0rpm In:0.8074(1),790; As(V):0.67898(1),+250; (Sb(V)); (InT)	T=0.40370µm	undoped	t=0:30:00.0
5	Excess As(V)	T_S 500.00°C +15.0rpm (In); As(V):0.67898(1),+250; (Sb(V)); (InT)		undoped	t=0:03:00.0
6S1	Start of 50 period Repeat Sequence...				
7S1	Matrix InAs(V)	T_S 500.00°C +15.0rpm In:0.8074(1),790; As(V):0.67898(1),+250; (Sb(V):0.00056(1),+44.9Iz); (InT)	T=0.00969µm	undoped	t=0:00:43.2
8S1	Excess As(V)	T_S 500.00°C +15.0rpm (In); As(V):0.01051(1),+135; (Sb(V)); (InT)		undoped	t=0:00:10.0
9S1	Excess $As(V)_{94.94}Sb(V)_{5.06}$	T_S 500.00°C +15.0rpm (In); As(V):0.01051(1),+135; Sb(V):0.00056(1),+44.9Iz; (InT)		undoped	t=0:00:03.0
10S1	Matrix $InAs(V)_{94.94}Sb(V)_{5.06}$	T_S 500.00°C +15.0rpm In:0.8074(1),790; As(V):0.01051(1),+135; Sb(V):0.00056(1),+44.9Iz; (InT)	T=0.00969µm	undoped	t=0:00:43.2
11S1	Excess $As(V)_{94.94}Sb(V)_{5.06}$	T_S 500.00°C +15.0rpm (In); As(V):0.01051(1),+135; Sb(V):0.00056(1),+44.9Iz; (InT)		undoped	t=0:00:03.0
12S1	Excess As(V)	T_S 500.00°C +15.0rpm (In); As(V):0.67898(1),+250; (Sb(V):0.0001(1),+0Iz); (InT)		undoped	t=0:00:10.0
13S1	...End of Repeat Sequence				
14	Excess As(V)	T_S 500.00°C +15.0rpm (In); As(V):0.01732(1),+150; (Sb(V)); (InT)		undoped	t=0:03:00.0
15	Matrix InAs(V)	T_S 500.00°C +15.0rpm In:0.8074(1),790; As(V):0.67898(1),+250; (Sb(V)); (InT)	T=0.04037µm	undoped	t=0:03:00.0
16	Excess As(V)	T_S 350.00°C +15.0rpm (In); As(V):0.00341(1),+100; (Sb(V)); (InT)		undoped	t=0:03:00.0
17	Growth Interrupt	T_S 350.00°C Rot Off (In); (As(V):0.0001(1),+0Iz); (Sb(V)); (InT)		undoped	t=0:00:10.0
18	Growth Interrupt	T_S 350.00°C Rot Off (In:0.00282(1),450.05Iz); (As(V)); (Sb(V)); (InT595(1),595)		undoped	t=0:30:00.0
19		...EPILIST END			
End	Growth Interrupt	T_S 350.00°C Rot Off (at end) SUB:Op; (In); (As(V)); (Sb(V)); (InT:Op)		undoped	(t=0:00:10.0)

Comms OK | P-LoopErrors | Sensor Fail | !!ALARM!! | - - - | EpiCAD

Figure A.1 – MBE recipe for growth of InAs/InAsSb SLS samples.

Appendix B

nextnanomat - C:\Users\James\Desktop\sim InAs InAsSb MQW.in

File Edit Run View Tools Help

Input | Template | Run | Output

```
##
## Simulation of InAs InAsSb SLS structure
##
## ------------------------------------------------------------------------

$QW_WID = 14                        # width of QW (units:nm)
$QW_SEP = 14                        # separation of QW (units:nm)
$PER_WID = $QW_WID + $QW_SEP        # width of 1 period (layer 1 + layer 2)
$NUM_LAY = 20                       # number of layers
$SUP_WID = $PER_WID * $NUM_LAY      # total width of active region
$SBX = 0.043   # Sb of InAsSb layers
$xalloy = 1-$SBX                    # material is InAs(x)Sb(1-x)
                                    # if SBX = 0.10 then XALLOY = 1 - 0.10 = 0.90 so QW is Sb = 10%

$GRID = 0.01                        # grid resolution

## ------------------------------------------------------------------------

global{
   simulate1D{}
   crystal_zb{
      x_hkl = [1, 0, 0]
      y_hkl = [0, 1, 0]
      }
   substrate{
      name = "InAs"                 # set material of substrate
      }
   temperature = 4               # set temperature
      }<>

database{
   ternary_zb{
   name = "InAs(x)Sb(1-x)"

  conduction_bands{
      Gamma{bandgap = 0.60}   # set CB bowing value
      }
   valence_bands{
      bandoffset = -0.90      # set VB bowing value
     delta_SO = 0             # set delta_SO bowing value
     }
   }

   binary_zb{
  name = "InSb"
  valence_bands{
    bandoffset = 1.84
      }
   }
   }<>

grid{
   xgrid{
      line{ pos = 0 spacing = $GRID }
      line{ pos = $SUP_WID spacing = $GRID }
   }
   periodic{x=yes}
   }<>

## ------------------------------------------------------------------------

structure{
   output_region_index{ boxes = no }
   output_material_index{ boxes = no }
   output_alloy_composition{ boxes = yes }

   region{
      everywhere{ # default region
      }
      contact { name = dummy }

      binary{
      name = "InAs"
      }
   }

   region{                          # parameters of first layer
      repeat_x{
         shift          = $PER_WID
         num            = $NUM_LAY
         }
      line{
         x = [0, $QW_SEP]
         }
      binary{
       name = "InAs"
         }
   }

   region{                          # parameters of second layer
      repeat_x{
         shift          = $PER_WID
         num            = $NUM_LAY
         }
      line{
         x = [$QW_SEP, $PER_WID]
         }
      ternary_constant{
        name = "InAs(x)Sb(1-x)"
        alloy_x=$xalloy
        }
   }
}<>
```

```
impurities{
}<>

contacts{
   fermi{ name = "dummy" bias = 0}
}

classical{
   Gamma{}
   HH{}
   LH{}
   SO{}
   output_bandedges{ averaged = no }
}<>

poisson{
}<>

currents{
}<>


## ------------------------------------------------------------------------

quantum{

region{
   name  =  "quantum_region"
    x  =  [$QW_SEP / 2, 1*$PER_WID + $QW_SEP / 2]

output_wavefunctions{
   max_num = 10
   amplitudes = yes
   probabilities = yes
      }

Gamma{
   num_ev   =  100
   accuracy =  1e-7
   iterations =  1000 }

HH{
   num_ev   =  100
   accuracy =  1e-7
   iterations =  1000 }

LH{
   num_ev   =  100
   accuracy =  1e-7
   iterations =  1000 }

SO{
   num_ev   =  100
   accuracy =  1e-7
   iterations =  1000 }
}
}<>

strain{
   pseudomorphic_strain{}

}<>

## ------------------------------------------------------------------------

run{
   solve_quantum{}
   solve_strain{}                  # solve with strain
   }<>

## ------------------------------------------------------------------------
## END CODE
## ------------------------------------------------------------------------
```

Figure A.2 – Nextnano software code to simulate InAs/InAsSb structure.

References:

[1] L. Meriggi, “Antimonide-based mid-infrared light-emitting diodes for low-power optical gas sensors,” University of Glasgow, 2015.

[2] H. Hardaway, J. Heber, P. Moeck, M. J. Pullin, T. Stradling, P. Tang and C. C. Phillips, “Optical studies of InAs/In(As,Sb) single quantum well (SQW) and strained-layer superlattice (SLS) LEDs for the mid-infrared (MIR) region,” *SPIE Proceedings - Light emitting diodes: research, manufacturing and applications III,* vol. 3621, 1999.

[3] M. J. Pullin, H. R. Hardaway, J. D. Heber, C. C. Phillips, W. T. Yuen and R. A. Stradling, “Room-temperature InAsSb strained-layer superlattice light-emitting diodes at 4.2um with AlSb barriers for improved carrier confinement,” *Applied Physics Letters,* vol. 74, no. 16, 1999.

[4] J. W. Matthews and A. E. Blakeslee, “Defects in epitaxial multilayers. I. misfit dislocations,” *Journal of Crystal Growth,* vol. 27, no. 118, 1974.

[5] D. A. Bui and P. C. Hauser, “Analytical devices based on light-emitting diodes - a review of the state-of-the-art,” *Analytica Chimica Acta,* vol. 853, pp. 46-58, 2015.

[6] M. Kohring, S. Bottger, U. Willer and W. Schade, “LED absorption QEPAS sensor for biogas plants,” *Sensors,* vol. 15, no. 5, pp. 12092-12102, 2015.

[7] P. J. Carrington, Q. Zhuang, M. Yin and A. Krier, “Temperature dependence of mid-infrared electroluminescence in type II InAsSb/InAs multi-quantum well light-emitting diodes,” *Semiconductor Science and Technology,* vol. 24, 2009.

[8] S. R. Tsai and M. R. Hamblin, “Biological effects and medical applications of infrared radiation,” *Journal of Photochemistry & Photobiology, B: Biology,* vol. 170, pp. 197-207, 2017.

[9] L. Fleming, D. Gibson, S. G. Song, C. Li and S. Reid, “Reducing N20 induced cross-talk in a NDIR CO2 gas sensor for breath analysis using multilayer thin film optical interference coatings,” *Surface & Coatings Technology,* vol. 336, pp. 9-16, 2018.

[10] D. Jung, S. Bank, M. L. Lee and D. Wasserman, “Next-generation mid-infrared sources,” *Journal of Optics,* vol. 19, no. 12, 2017.

[11] D. T. Norton, J. T. Olesberg, R. T. McGee, N. A. Waite, J. Dickason, K. W. Goossen, J. Lawler, G. Sullivan, A. Ikhlassi, F. Kaimilev, E. J. Koerperick, L. M. Murray, J. P. Prineas and T. F. Boggess, “512 x 512 individually addressable MWIR LED arrays based on type-II InAs/GaSb superlattices,” *IEEE Journal Quantum Electronics,* vol. 49, no. 9, 2013.

[12] M. S. Villar, “Mid-infrared absorption spectrometer for multi-species detection using LEDs for space applications: Development and flight testing,” University of Central Florida, 2015.

[13] D. Smith, A. Vass and P. Bramley, “Comparison of IR LED gas sensors with thermal source products,” *IEE Proc. Optoelectronics,* vol. 144, 1997.

[14] A. Krier, H. H. Gao, V. V. Sherstnev and Y. Yakovlev, “High power 4.6um light emitting diodes for CO detection,” *Journal of Physics D: Applied Physics,* vol. 32, pp. 3117-3121, 1999.

[15] “Atmospheric greenhouse gas concentrations,” European Environment Agency, 31 01 2018. [Online]. Available: https://www.eea.europa.eu/data-and-maps/indicators/atmospheric-greenhouse-gas-concentrations-10/assessment. [Accessed 07 09 2018].

[16] D. Gibson and C. MacGregor, “A novel solid state non-dispersive infrared CO2 gas sensor compatible with wireless and portable deployment,” *Sensors,* vol. 13, pp. 7079-7103, 2013.

[17] S. D. Smith, J. G. Crowder and H. R. Hardaway, “Recent developments in the applications of mid-infrared lasers, LEDs and other solid state sources to gas detection,” in *Conference on Novel In-Plane Semiconductor Lasers*, San Jose, CA, USA, 2002.

[18] A. Krier, Mid-infrared Semiconductor Optoelectronics, Springer, 2007.

[19] Y. P. Varshni, “Temperature dependence of the energy gap in semiconductors,” *Physica Utrecht,* vol. 34, 1967.

[20] P. T. Webster, N. A. Riordan, S. Liu, E. H. Steenbergen, R. A. Synowicki, Y. H. Zhang and S. R. Johnson, “Measurement of InAsSb bandgap energy and InAs/InAsSb band edge positions using spectroscopic ellipsometry and photoluminescence spectroscopy,” *Journal of Applied Physics,* vol. 118, no. 24, 2015.

[21] E. F. Schubert, Light-emitting diodes, Cambridge University Press, 2018.

[22] C. W. Passchier and A. J. Rudolph, Microtectonics, Springer, 2005.

[23] F. C. Frank and J. H. van der Merwe, “One-dimensional dislocations. II. misfitting monolayers and oriented overgrowth,” *Proceedings of the Royal Society A,* vol. 198, no. 1053, 1949.

[24] R. People and J. C. Bean, “Calculation of critical layer thickness versus lattice mismatch for GexSi1-x/Si strained-layer heterostructures,” *Applied Physics Letters,* vol. 47, no. 3, 1985.

[25] E. P. O'Reilly, “Valence band engineering in strained-layer structures,” *Semiconductor Science and Technology ,* vol. 4, no. 121, 1989.

[26] M. P. C. M. Krijn, “Heterojunction band offsets and effective masses in III-V quarternary alloys,” *Semiconductor Science and Technology,* vol. 6, 1991.

[27] S. Jain, M. Willander and R. van Overstraeten, Compound semiconductors: Vol. 7 - strained layers and devices, Springer US, 2000.

[28] S. H. Huang, G. Balakrishnan, A. Khoshakhlagh, A. Jallipalli, L. R. Dawson and D. L. Huffaker, “Strain relied by periodic misfit arrays for low defect density GaSb on GaAs,” *Applied Physics Letters,* vol. 88, 2006.

[29] A. Jallipalli, G. Balakrishnan, S. H. Huang, T. J. Rotter, K. Nunna, B. L. Liang, L. R. Dawson and D. L. Huffaker, “Structural analysis of highly relaxed GaSb grown on GaAs substrates with periodic interfacial array of 90 degree misfit dislocations,” *Nanoscale Research Letters,* vol. 4, no. 12, pp. 1458-1462, 2009.

[30] J. P. Hayton, “Development of mid-infrared light emitting diodes to replace incandescent airfield lighting (PhD thesis),” Lancaster University, 2016.

[31] M. Fox, Optical properties of solids, New York: Oxford University Press, 2001.

[32] J. Singh and R. T. Williams, Exciton and photonic processes in materials, Springer, 2014.

[33] P. J. Carrington, “Quantum nanostructures grown by molecular beam epitaxy for mid-infrared applications (PhD thesis),” Lancaster University, 2009.

[34] E. Selcuk, “Guided and deterministic self organization of quantum dots,” Eindhoven University of Technology, 2009.

[35] J. R. Lindle, J. R. Meyer, C. A. Hoffman, F. J. Bartoli, G. W. Turner and H. K. Choi, “Auger lifetime in InAs, InAsSb, and InAsSb-InAlAsSb quantum wells,” *Applied Physics Letters,* vol. 67, no. 21, 1995.

[36] R. I. Taylor, “Auger recombination in low-dimensional semiconductor structures (Phd Thesis),” Durham University, 1987.

[37] H. K. Choi, Long-wavelength infrared semiconductor lasers, John Wiley & Sons, 2004.

[38] G. Kirsanske, P. Tighineanu, R. S. Deveau, J. Miguel-Sanchez, P. Lodahl and S. Stobbe,

"Observation of the exciton Mott transition in the photoluminescence of coupled quantum wells," *Physical Review B,* vol. 94, no. 15, p. 155438, 2016.

[39] M. Stern, V. Garminder, V. Umansky and I. Bar-Joseph, "Mott transition of excitons in coupled quantum wells," *Physical Review Letters,* vol. 100, no. 25, 2008.

[40] S. Ben-Tabou de-Leon and B. Laikhtman, "Mott transition, biexciton crossover, and spin ordering in the exciton gas in quantum wells," *Physcal Review B,* vol. 67, no. 23, 2003.

[41] B. Deveaud, L. Kappei, J. Berney, F. Morier-Genoud, M. T. Portella-Oberli, J. Szczytko and C. Piermarocchi, "Excitonic effects in the luminescence of quantum wells," *Chemical Physics,* vol. 318, 2005.

[42] T. M. Rice, "The electron-hole liquid in semiconductors: theoretical aspects," *Solid State Physics,* vol. 32, pp. 1-86, 1978.

[43] N. F. Mott, "The basis of the electron theory of metals, with special reference to the transition metals," *Proceedings of the Physical Society,* vol. 62, no. 7, pp. 416-422, 1949.

[44] A. Amo, M. D. Martin, L. Vina, A. I. Toropov and K. S. Zhuravlev, "Photoluminescence dynamics in GaAs along an optically induced Mott transition," *Journal of Applied Physics,* vol. 101, no. 8, 2007.

[45] V. V. Nikolaev and M. E. Portnoi, "Theory of the excitonic Mott transition in quasi-two-dimensional systems," *Superlattices and Microstructures,* vol. 43, no. 5, pp. 460-464, 2008.

[46] S. W. Koch, W. Hoyer, M. Kira and V. S. Filinov, "Exciton ionization in semiconductors," *Physica Status Solidi B,* vol. 238, no. 3, pp. 404-410, 2003.

[47] L. Kappei, J. Szczytko, F. Morier-Genoud and B. Deveaud, "Direct observation of the Mott transition in an optically excited semiconductor quantum well," *Physical Review Letters,* vol. 94, no. 14, 2005.

[48] Y. E. Lozovik and O. K. Berman, "Phase transitions in a system of two coupled quantum wells," *JETP Letters,* vol. 64, no. 8, pp. 573-579, 1996.

[49] G. Manzke, D. Semkat and H. Stolz, "Mott transition of excitons in GaAs-GaAlAs quantum wells," *New Journal of Physics,* vol. 14, 2012.

[50] C. Schindler and R. Zimmerman, "Analysis of the exciton-exciton interaction in semiconductor quantum wells," *Physical Review B,* vol. 78, no. 4, 2008.

[51] D. A. B. Miller, Optical physics of quantum wells, 1996.

[52] M. Shahmohammadi, G. Jacopin, G. Rossbach, J. Levrat, E. Feltin, J. F. Carlin, J. D. Ganiere, R. Butte, N. Grandjean and B. Deveaud, "Biexcitonic molecules survive excitons at the Mott transition," *Nature Communications,* vol. 5, 2014.

[53] A. Krier, "Mid-infrared electroluminescence in LEDs based on InAs and related alloys," in *Mid-infrared semiconductor optoelectronics*, Springer, 2005.

[54] E. Dupont, J. P. McCaffrey, H. C. Liu, M. Buchanan, R. Q. Yang, C. H. Lin, D. Zhang and S. S. Pei, "Demonstration of cascade process in InAs/GaInSb/AlSb mid-infrared light emitting devices," *Applied Physics Letters,* vol. 72, no. 12, 1998.

[55] S. H. Wei and A. Zunger, "InAsSb/InAs: A type-I or a type-II band alignment," *Physical Review B,* vol. 52, no. 16, pp. 12039-12044, 1995.

[56] G. S. Lee, Y. Lo, Y. F. Lin, S. M. Bedair and W. D. Laidig, "Growth of InAs_1-xSb_x (0<x<1) and InSb-InAsSb superlattices by molecular beam epitaxy," *Applied Physics Letters,* vol. 47, pp. 1219-1221, 1985.

[57] L. R. Dawson, "Summary abstract: Molecular beam epitaxial growth of InAsSb alloys and superlattices," *J. Vac. Sci. Tech. B,* vol. 4, no. 2, 1986.

[58] M. Y. Yen, R. Peopie, K. W. Wecht and A. Y. Cho, “Long wavelength photoluminescence of InAs1-xSbx (0<x<1) grown by molecular beam epitaxy on (100) InAs,” *Applied Physics Letters,* vol. 52, 1988.

[59] J. C. Woolley and J. Warner, “Optical energy-gap variation in InAs-InSb alloys,” *Canadian Journal of Physics,* vol. 42, 1964.

[60] I. T. Ferguson, A. G. Norman and B. A. Joyce, “Molecular beam epitaxial growth of InAsSb strained layer superlattices. Can nature do it better?,” *Applied Physics Letters,* vol. 59, no. 25, 1991.

[61] M. Kesaria, M. de la Mare and A. Krier, “Room temperature mid-infrared InAsSbN multi-quantum well photodiodes grown by MBE,” *Journal of Physics D: Applied Physis,* vol. 49, 2016.

[62] M. de la Mare, P. J. Carrington, R. Wheatley, Q. Zhuang, R. Beanland, A. M. Sanchez and A. Krier, “Photoluminescence of InAs_0.926Sb_0.063N_0.011/InAs multi-quantum wells in the mid-infrared spectral range,” *Journal of Physics D: Applied Physics,* vol. 43, no. 34, 2010.

[63] P. T. Webster, A. J. Shalinder, S. T. Schaefer and S. R. Johnson, “Bandgap and composition of bulk InAsSbBi grown by molecular beam epitaxy,” *Applied Physics Letters,* vol. 111, no. 8, 2017.

[64] A. J. Shalindar, P. T. Webster, S. T. Schaefer and S. R. Johnson, “InAsBi Materials,” in *Molecular Beam Epitaxy: Research to Mass Production*, Elsevier, 2018, pp. 181-196.

[65] J. I. Chyi, S. Kalem, N. S. Kumar, C. W. Litton and H. Morkoc, “Growth of InSb and InAs_1-xSb_x on GaAs by molecular beam epitaxy,” *Applied Physics Letters,* vol. 53, no. 12, 1988.

[66] G. C. Osbourn, “InAsSb strained-layer superlattices for long wavelength detector applications,” *Journal of Vacuum Science & Technology B,* vol. 2, no. 2, 1984.

[67] S. R. Kurtz, G. C. Osbourn, R. M. Biefeld and S. R. Lee, “Photoluminescence and the band structure of InAsSb strained-layer superlattices,” *Applied Physics Letters,* vol. 53, pp. 216-218, 1988.

[68] M. Y. Yen, R. People and K. W. Wecht, “Long wavelength (3-5 and 8-12 um) photoluminescence of InAs_1-xSb_x grown on (100) GaAs by molecular-beam epitaxy,” *Journal Applied Physics,* vol. 64, no. 2, 1988.

[69] H. Q. Wen and E. Bellotti, “Optical absorption and intrinsic recombination in relaxed and strained InAs1-xSbx alloys for mid-wavelength infrared application,” *Applied Physics Letters,* vol. 107, no. 22, 2015.

[70] S. R. Kurtz, R. M. Biefeld and A. J. Howard, “Magneto-optical determination of light-heavy hole splittings in As-rich InAsSb alloys and superlattices,” *Applied Physics Letters,* vol. 67, no. 22, 1995.

[71] C. M. Ciesla, B. N. Murdin, C. R. Pidgeon, R. A. Stradling, C. C. Phillips, M. Livingstone, I. Galbraith, D. A. Jaroszynski, C. J. G. M. Langerak, P. J. P. Tang and M. J. Pullin, “Suppression of auger recombination in arsenic-rich InAs_1-xSb_x strained layer superlattices,” *Journal of Applied Physics,* vol. 80, no. 5, pp. 2994-2997, 1996.

[72] E. H. Steenbergen, K. Nunna, L. Ouyang, B. Ullrich, D. L. Huffaker, D. J. Smith and Y. H. Zhang, “Strain-balanced InAs/InAs_1-xSb_x type-II superlattices grown by molecular beam epitaxy on GaSb substrates,” *Journal Vacuum Science & Technology B,* vol. 30, no. 2, 2012.

[73] I. Melngailis and R. H. Rediker, *Journal Applied Physics,* vol. 37, p. 899, 1966.

[74] A. N. Baranov, A. N. Imenkov, O. P. Kapranchik, V. V. Negreskul, A. G. Chernyavskii, V. V. Sherstnev and Y. P. Yakovlev, “Long-wavelength light-emitting diodes based on

InAs1-x-1-ySbxPy/InAs heterostructures with a wide-gap window," *Pis'ma Zh. Tekh. Fiz.,* vol. 16, pp. 42-47, 1990.

[75] W. Dobbelaere, J. De Broek, C. Bruynseraede, R. Mertens and G. Borghs, "InAsSb light emitting diodes and their applications to infra-red gas sensors," *Electronics Letters,* vol. 29, no. 10, 1993.

[76] B. A. Matveev, G. A. Gavrilov, V. V. Evstropov, N. V. Zotova, S. A. Karandashov, G. Y. Sotnikova, N. M. Stus', G. N. Talalakin and J. Malinen, "Mid-infrared (3-5um) LEDs as sources for gas and liquid sensors," *Sensors and Actuators,* vol. 39, no. 1, pp. 339-343, 1997.

[77] B. Matveev, M. Aidaraliev, G. Gavrilov, N. Zotova, S. Karandashov, G. Sotnikova, N. Stus', G. Talalakin, N. Il'inskaya and S. Aleksandrov, "Room temperature InAs photodiode - InGaAs LED pairs for methane detection in the mid-IR," *Sensors and Actuators,* vol. 51, pp. 233-237, 1998.

[78] S. McCabe and B. D. MacCraith, "Novel midinfrared LED as a source for optical-fiber gas-sensing," *Electronics Letters,* vol. 29, no. 19, pp. 1719-1721, 1993.

[79] Y. Mao and A. Krier, "InAsSb p-n junction light emitting diodes grown by liquid phase epitaxy," *Journal of Physics and Chemistry of Solids,* vol. 56, no. 5, pp. 759-766, 1995.

[80] Y. Mao and A. Krier, "Efficient 4.2um light emitting diodes for detecting CO2 at room temperature," *Electronics Letters,* vol. 32, no. 5, 1996.

[81] Y. Mao and A. Krier, "Uncooled 4.2um light emitting diodes based on InAs_0.91Sb_0.09/GaSb grown by LPE," *Optical Materials,* vol. 6, no. 1, pp. 55-61, 1996.

[82] M. K. Haigh, G. R. Nash, S. J. Smith, L. Buckle, M. T. Emeny and T. Ashley, "Mid-infrared Al_xIn_1-xSb light-emitting diodes," *Applied Physics Letters,* vol. 90, 2007.

[83] G. Cao, Nanostructures and nanomaterials: synthesis, properties and applications, Imperial College Press, 2004.

[84] Y. Aytac, B. V. Olson, J. K. Kim, E. A. Shaner, S. D. Hawkins, J. F. Klem, M. E. Flatte and T. F. Boggess, "Effects of layer thickness and alloy composition on carrier lifetimes in mid-wave infrared InAs/InAsSb superlattices," *Applied Physics Letters,* vol. 105, no. 2, 2014.

[85] Y. Aytac, B. V. Olson, J. K. Kim, E. A. Shaner, S. D. Hawkins, J. F. Klem, J. Olesberg, M. E. Flatte and T. F. Boggess, "Bandgap and temperature dependence of Auger recombination in InAs/InAsSb type-II superlattices," *Journal of Applied Physics,* vol. 119, no. 21, 2016.

[86] C. C. Phillips, "In(As, Sb) superlattice-based emitters for mid-IR wavelengths," *IEE Proceedings - Optoelectronics,* vol. 144, no. 5, pp. 262-265, 1997.

[87] P. J. P. Tang, H. Hardaway, J. Heber, C. C. Phillips, M. J. Pullin, R. A. Stradling, W. T. Yuen and L. Hart, "Efficient 300 K light-emitting diodes at lambda ~ 5 and ~ 8 um from InAs/In(As1-xSbx) single quantum wells," *Applied Physics Letters,* vol. 72, no. 26, pp. 3473-3475, 1998.

[88] A. Krier and M. Fisher, "Comparison of light emission from room temperature light emitting diodes with InAs active regions grown by LPE," *IEE Proceedings - Optoelectronics,* vol. 144, no. 5, pp. 287-294, 1997.

[89] B. Matveev, N. Zotova, S. Karandashov, M. Remennyi, N. Il'inskaya, N. Stus', V. Shustov, G. Talalakin and J. Malinen, "InAsSbP/InAs LEDs for the 3.3-5.5um spectral range," *IEE Proceedings - Optoelectronics,* vol. 145, no. 5, pp. 254-256, 1998.

[90] E. A. Grebenshchikova, N. V. Zotova, S. S. Kizhaev, S. S. Molchanov and Y. P. Yakovlev, "InAs/InAsSbP light-emitting structures grown by gas-phase epitaxy," *Technical Physics,* vol. 46, no. 9, pp. 1125-1127, 2001.

[91] A. Krier and V. V. Sherstnev, “LEDs for formaldehyde detection at 3.6 mu m,” *Journal of Applied Physics D - Applied Physics,* vol. 34, no. 3, pp. 428-432, 2001.

[92] N. V. Zotova, S. S. Kizhaev, S. S. Molchanov, T. B. Popova and Y. P. Yakovlev, “Long-wavelength light-emitting diodes based on InAsSb/InAs heterostructures grown by vapor-phase epitaxy,” *Semiconductors,* vol. 34, no. 12, pp. 1402-1405, 2000.

[93] A. S. Golovin, A. P. Astakhova, S. S. Kizhaev, N. D. Il'inskaya, O. Y. Serebrennikova and Y. P. Yakovlev, “LEDs based on InAs/InAsSb heterojunctions for CO2 spectroscopy,” *Technical Physics Letters,* vol. 36, no. 1, pp. 47-49, 2010.

[94] S. S. Kizhayev, N. V. Zotova, S. S. Molchanov and Y. P. Yakovlev, “High-power mid-infrared light emitting diodes grown by MOVPE,” *IEE Proceedings - Optoelectronics,* vol. 149, no. 1, pp. 36-39, 2002.

[95] H. H. Gao, A. Krier, V. Sherstnev and Y. Yakovlev, “InAsSb/InAsSbP light emitting diodes for the detection of CO and CO2 at room temperature,” *Journal of Physics D - Applied Physics,* vol. 32, no. 15, pp. 1768-1772, 1999.

[96] A. A. Popov, M. V. Stepanov, V. V. Sherstnev and Y. P. Yakovlev, “InAsSb light-emitting diodes for the detection of CO_2 (lambda = 4.3um),” *Technical Physics Letters,* vol. 24, no. 8, 1998.

[97] X. Y. Gong, H. Kan, T. Makino, T. Lida, K. Watanabe, Y. Z. Gao, M. Aoyama, N. L. Rowell and T. Yamaguchi, “Room-temperature mid-infrared light-emitting diodes from liquid-phase epitaxial InAs/InAs_0.89Sb_0.11/InAs_0.80P_0.12Sb_0.08 heterostructures,” *Japanese Journal of Applied Physics,* vol. 39, no. 1, p. 9A, 2000.

[98] V. V. Sherstnev, A. M. Monahov, A. Krier and G. Hill, “Superluminescence in InAsSb circular-ring-mode light-emitting diodes for CO gas detection,” *Applied Physics Letters,* vol. 77, no. 24, pp. 3908-3910, 2000.

[99] A. Krier, M. Stone, Q. D. Zhuang, P. W. Liu, G. Tsai and H. H. Lin, “Mid-infrared electroluminescence at room temperature from InAsSb multi-quantum-well light-emitting diodes,” *Applied Physics Letters,* vol. 89, no. 9, 2006.

[100] B. Grietens, S. Nemeth, C. Van Hoof, P. Van Daele and G. Borghs, “Growth and characterisation of mid-IR InAs0.9Sb0.1/InAs strained multiple quantum well light emitting diodes grown on InAs substrates,” *IEE Proceedings - Optoelectronics,* vol. 144, no. 5, pp. 295-298, 1997.

[101] G. R. Nash, M. K. Haigh, H. R. Hardaway, L. Buckle, A. D. Andreev, N. T. Gordon, S. J. Smith, M. T. Emeny and T. Ashley, “InSb/AlInSb quantum-well light-emitting diodes,” *Applied Physics Letters,* vol. 88, 2006.

[102] B. I. Mirza, G. R. Nash, S. J. Smith, M. K. Haigh, L. Buckle, M. T. Emeny and T. Ashley, “InSb/Al_xIn_1-xSb quantum-well light-emitting diodes with high internal quantum efficiencies,” *Applied Physics Letters,* vol. 89, 2006.

[103] G. G. Zegrya and A. D. Andreev, “Mechanism of suppression of Auger recombination processes in type-II heterostructures,” *Applied Physics Letters,* vol. 67, no. 18, pp. 2681-2683, 1995.

[104] A. Slonopas and D. Tomkinson, “Study of the natural auger suppression mechanism in heterostructures through heteroboundary engineering,” *The Journal of Physical Chemistry,* vol. 121, pp. 7745-7750, 2017.

[105] P. J. P. Tang, M. J. Pullin, S. J. Chung, C. C. Phillips, R. A. Stradling, A. G. Norman, Y. B. Li and L. Hart, “4-11 um infrared-emission and 300 K light-emitting-diodes from arsenic-rich InAs1-xSbx strained-layer superlattices,” *Semiconductor Science and Technology,* vol. 10, no. 8, pp. 1177-1180, 1995.

[106] R. J. Ricker, S. Provence, L. M. Murray, D. T. Norton, J. T. Olesberg, J. P. Prineas and T. F.

Boggess, “512x512 array of dual-color InAs/GaSb superlattice light-emitting diodes,” San Francisco, CA, 2017.

[107] R. J. Ricker, A. Hudson, S. Provence, D. T. Norton, J. T. Olesberg, L. M. Murray, J. P. Prineas and T. F. Boggess, “Dual-color InAs/GaSb cascaded superlattice light-emitting diodes,” *IEEE Journal of Quantum Electronics,* vol. 51, no. 12, 2015.

[108] E. J. Koerperick, D. T. Norton, J. T. Olesberg, B. V. Olson, J. P. Prineas and T. F. Boggess, “Cascaded superlattice InAs/GaSb light-emitting diodes for operation in the long-wave infrared,” *IEEE Journal of Quantum Electronics,* vol. 47, no. 1, pp. 50-54, 2011.

[109] O. O. Cellek, H. Li, X. M. Shen, Z. Lin, E. H. Steenbergen and et. al., “InAs/InAsSb type-II superlattice: A promising material for mid-wavelength and long-wavelength infrared applications,” in *SPIE Infraed Technology and Applications XXXVIII*, 2012.

[110] M. Pullin, X. B. Li, J. Heber, D. Gevaux and C. C. Phillips, “Improved efficiency positive and negative luminescent light emitting devices for mid-infrared gas sensing applications,” in *4th Conference on Light-Emitting Diodes (LEDs)*, San Jose, CA, 2000.

[111] J. D. Heber, D. Gevaux, X. Li and C. C. Phillips, “Room temperature InAs/InAs1-xSbx single quantum well light emitting diodes with barriers for improved carrier confinement,” *IEE Proceedings - Optoelectronics,* vol. 147, no. 6, pp. 407-411, 2000.

[112] N. C. Das, K. Olver, F. Towner, G. Simonis and H. Shen, “Infrared (3.8um) interband cascade light-emitting diode array with record high efficiency,” *Applied Physics Letters,* vol. 87, no. 4, p. 041105, 2005.

[113] E. J. Koerperick, J. T. Olesberg, J. L. Hicks, J. P. Prineas and T. F. Boggess, “Active region cascading for inproved performance in InAs-GaSb superlattice LEDs,” *IEEE Journal Quantum Electronics,* vol. 44, no. 11, pp. 1242-1247, 2008.

[114] D. Zhang, E. Dupont, R. Q. Yang, H. C. Liu, C. H. Lin, M. Buchanan and S. S. Pei, “Long-wavelength infrared (10-15um) electroluminescence from Sb-based interband cascade devices,” *Optics Express,* vol. 1, no. 4, pp. 97-101, 1997.

[115] J. Abell, C. S. Kim, W. W. Bewley, C. D. Merritt, C. L. Canedy, I. Vurgaftman, J. R. Meyer and M. Kim, “Mid-infrared interband cascade light emitting devices with milliwatt output powers at room temperature,” *Applied Physics Letters,* vol. 104, no. 26, 2014.

[116] C. S. Kim, W. W. Bewley, C. D. Merritt, C. L. Canedy, M. V. Warren, I. Vurgaftman, J. R. Meyer and M. Kim, “Improved mid-infrared interband cascade light-emitting devices,” *Optical Engineering,* vol. 57, no. 1, 2018.

[117] T. J. Phillips, “High performance thermal imaging technology,” *III-Vs Review,* vol. 15, no. 7, pp. 32-34, 2002.

[118] D. R. Gibson and C. MacGregor, “Self powered non-dispersive infra-red CO2 gas sensor,” *Journal of Physics,* vol. 307, no. 1, 2011.

[119] H. R. Hardaway, T. Ashley, L. Buckle, M. T. Emeny, G. Masterton and G. Pryce, “Optimizing indium aluminum antimonide LEDs and photodiodes for gas sensing applications,” *SPIE Proceedings: Infrared Detector Materials and Devices,* vol. 5564, 2004.

[120] H. Fujita, K. Ueno, O. Morohara, E. Camargo, H. Geka, Y. Shibata and K. Naohiro, “AlInSb mid-infrared LEDs of high luminous efficiency for gas sensors,” *Physica Status Solidi A,* vol. 215, no. 8, 2018.

[121] G. A. Ejzak, J. Dickason, J. A. Marks, K. Nabha, R. T. McGee, N. A. Waite, J. T. Benedict, M. A. Hernandez, S. R. Provence, D. T. Norton, J. P. Prineas, K. W. Goossen, F. E. Kiamilev and T. F. Boggess, “512 x 512, 100 hZ mid-wave infrared LED microdisplay system,” *Journal of Display Technology,* vol. 12, no. 10, pp. 1139-1144, 2016.

[122] B. A. Matveev, M. Aydaraliev, N. V. Zotova, S. A. Karandashov, N. D. Il'inskaya, M. A.

Remennyi, N. M. Stus' and G. N. Talalakin, “Flip-chip bonded InAsSbP and InGaAs LEDs and detectors for the 3um spectra region,” *IEE Proceedings Optoelectronics,* vol. 150, no. 4, pp. 356-359, 2003.

[123] R. Stanley, “Plasmonics in the mid-IR,” *Nature Photonics,* vol. 6, pp. 409-411, 2012.

[124] T. W. Ebbesen, H. J. Lezec, H. F. Ghaemi, T. Thio and P. A. Wolff, “Extraordinary optical transmission through sub-wavelength hole arrays,” *Nature,* vol. 391, 1998.

[125] A. I. Zhmakin, “Enhancement of light extraction from light emitting diodes,” *Physics Reports,* vol. 498, no. 4, pp. 189-241, 2011.

[126] K. Okamoto, I. Niki, A. Shvartser, Y. Narukawa, T. Mukai and A. Scherer, “Surface-plasmon-enhanced light emitters based on InGaN quantum wells,” *Naturae Materials,* vol. 3, pp. 601-605, 2004.

[127] W. L. Barnes, “Light-emitting devices: turning the tables on surface plasmons,” *Nature Materials,* vol. 3, pp. 588-589, 2004.

[128] M. Li, H. Zhen, Y. Jing, H. Wang and N. Li, “Efficiency enhancement of infrared light emitting diodes by combination of photonic crystals and surface plasmons,” *Opt Quant Electron,* 2016.

[129] S. Birner, T. Zibold, T. Andlauer, T. Kubis, M. Sabathil, A. Trellakis and P. Vogl, “Nextnano: general purpose 3D simulations,” *IEEE Transactions on Electron Devices,* vol. 54, no. 9, 2007.

[130] I. Vurgaftman, J. R. Meyer and L. R. Ram-Mohan, “band parameters for III-V compound semiconductors and their alloys,” *Journal of Applied Physics,* vol. 89, 2001.

[131] D. Lackner, InAsSb/InAs strain balanced superlattices for photodetector applications, Simon Fraser University (thesis), 2009.

[132] K. Muraki, S. Fukatsu and Y. Shiraki, “Surface segregation of In atoms during molecular beam epitaxy and its influence on the energy levels in InGaAs/GaAs quantum wells,” *Applied Physics Letters,* vol. 61, no. 5, 1992.

[133] P. W. Liu, G. Tsai and H. H. Lin, “Photoluminescence and bowing parameters of InAsSb/InAs multiple quantum wells grown by molecular beam epitaxy,” *Appl. Phys. Lett.,* vol. 89, 2006.

[134] S. A. Cripps, T. J. Hosea and A. Krier, “Midinfrared photoreflectance study of InAs-rich InAsSb and GaInAsPSb indicating negligible bowing for the spin orbit splitting energy,” *Appl. Phys. Lett.,* vol. 90, 2007.

[135] S. P. Svensson, W. L. Sarney and D. Donetsky, “Materials design parameters for infrared device applications based on III-V semiconductors,” *Appl. Optics,* vol. 56, 2017.

[136] E. J. Sie, “Coherent light-matter interactions in monolayer transition-metal dichalcogenides,” PhD Thesis, Massachusetts Institute of Technology, 2017.

[137] J. A. Keen, D. Lane, M. Kesaria, A. R. J. Marshall and A. Krier, “InAs/InAsSb type-II strained-layer superlattices for mid-infrared LEDs,” *Journal of Physics D: Applied Physics,* vol. 51, no. 7, p. 075103, 2018.

[138] J. A. Keen, E. Repiso, Q. Lu, M. Kesaria, A. R. J. Marshall and A. Krier, “Electroluminescence and photoluminescence of type-II InAs/InAsSb strained-layer superlattices in the mid-infrared,” *Infrared Physics & Technology,* vol. 93, pp. 375-380, 2018.

[139] P. J. Carrington, V. A. Solov'ev, Q. Zhuang, A. Krier and S. V. Ivanov, “Room temperature midinfrared electroluminescence from InSb/InAs quantum dot light emitting diodes,” *Applied Physics Letters,* vol. 93, no. 9, 2008.